โปรโตคอลที่เหมาะสมในการตรวจ MRCP ด้วยเครื่อง MRI 0.4 เทสลา (ชนิดอุโมงค์เปิด) และเปรียบเทียบคุณภาพของภาพกับ MRI 3.0 เทสลา

นายกฤษฎางค์ ทะเสนฮด

วิทยานิพนธ์นี้เป็นส่วนหนึ่งของการศึกษาตามหลักสูตร

ปริญญาวิทยาศาสตรมหาบัณฑิต สาขาวิชาฉายาเวชศาสตร์

ภาควิชารังสีวิทยา คณะแพทยศาสตร์

จุฬาลงกรณ์มหาวิทยาลัย

ปีการศึกษา 2553

OPTIMIZATION PROTOCOLS OF MRCP IMAGING FOR MRI 0.4 TESLA (OPEN) AND COMPARISON IMAGE QUALITY WITH MRI 3.0 TESLA

Mr.Krisadang Thasenhod

A Thesis Submitted in Partial Fulfillment of the Requirements

for the Degree of Master of Science Program in Medical Imaging

Department of Radiology Faculty of Medicine

Chulalongkorn University

Academic Year 2010

Thesis Title	OPTIMIZATION PROTOCOLS OF MRCP IMAGING FOR MRI 0.4 TESLA (OPEN) AND COMPARISON IMAGE QUALITY WITH MRI 3.0 TESLA
By	Mr. Krisadang Thasenhod
Field of study	Medical Imaging
Thesis Advisor	Associate Professor Anchali Krisanachinda, Ph.D.
Thesis Co-Advisor	Associate Professor Sukalaya Lerdlum, M.D.

Accepted by the Faculty of Medicine, Chulalongkorn University in Partial Fulfillment of the requirements for the Master's Degree

.....Dean of the Faculty of Medicine

(Professor Adisorn Patradul, M.D.)

THESIS COMMITTEE

.....Chairman

(Associate Professor Somjai Wangsuphachart, M.D.)

.....Thesis Advisor

(Associate Professor Anchali Krisanachinda, Ph.D.)

.....Thesis Co-Advisor

(Associate Professor Sukalaya Lerdlum, M.D.)

.....External Examiner

(Professor Franco Milano)

กฤษฎางค์ ทะเสนฮด : โปรโตคอลที่เหมาะสมในการตรวจเอ็มอาร์ซีพี ด้วยเครื่องเอ็มอาร์ไอ 0.4 เทสลา (ชนิดอุโมงค์เปิด) และเปรียบเทียบคุณภาพของภาพกับเครื่องเอ็มอาร์ไอ 3.0 เทสลา (OPTIMIZATION PROTOCOLS OF MRCP IMAGING FOR MRI 0.4 TESLA (OPEN) AND COMPARISON IMAGE QUALITY WITH MRI 3.0 TESLA) อ.ที่ปรึกษาวิทยานิพนธ์หลัก: รศ.ดร. อัญชลี กฤษณจินดา, อ.ที่ปรึกษาวิทยานิพนธ์ร่วม: รศ.พญ. สุกัลยา เลิศล้ำ : 87 หน้า.

ในปัจจุบันความเข้มของสนามแม่เหล็กสูงๆเป็นที่นิยมเพิ่มขึ้น ความเข้มของสนามแม่เหล็กเป็นปัจจัยสำคัญในการแสดงคุณภาพของภาพ การแสดงรายละเอียดของภาพ อัตราส่วนของสัญญาณภาพต่อสัญญาณรบกวน อัตราส่วนของความคมชัดบนภาพต่อสัญญาณรบกวน และประสิทธิภาพในการลดสัญญาณรบกวน การเลือกใช้เครื่องตรวจด้วยสนามแม่หล็กนั้นมีปัจจัยหลายอย่างที่นำมาพิจารณาเช่นราคา ชนิดของแม่เหล็ก ค่าใช้จ่ายในการบำรุงรักษา ความหลากหลายของการตรวจ รวมถึงความเหมาะสมในการตรวจกับผู้ป่วย ด้วยเหตุที่สนามแม่เหล็กที่มีความเข้มสูงนั้นมีราคาแพง ค่าใช้จ่ายในการบำรุงรักษาสูง ดังนั้นสนามแม่เหล็กชนิดอุโมงค์เปิดที่ความเข้มของสนามแม่เหล็กไม่สูง จึงเป็นเครื่องมือที่ถูกนำมาพิจารณา ด้วยเหตุผลหลักคือมีราคาไม่แพง ค่าใช้จ่ายในการบำรุงรักษาต่ำ รวมถึงการรองรับผู้ป่วยที่กลัวการเข้าไปนอนในอุโมงค์แม่เหล็กแคบๆ ดังนั้นการศึกษานี้จึงมีวัตถุประสงค์เพื่อหาปัจจัยที่เหมาะสมในการแสดงภาพของระบบท่อทางเดินน้ำดี ที่สร้างโดยเครื่องตรวจด้วยสนามแม่เหล็กความเข้ม 0.4 เทสลาชนิดอุโมงค์เปิด แล้วนำมาเปรียบเทียบกับภาพที่ตรวจด้วยเครื่องตรวจด้วยสนามแม่เหล็กความเข้ม 3.0 เทสลา

*ท่อพลาสติก*ขนาดเส้นผ่าศูนย์กลาง 2 มม. ถูกนำมาสแกนเพื่อศึกษาระยะที่สั้นที่สุดที่เครื่องมือสามารถแสดงรายละเอียด (เอฟดับเบิ้ลยูเอชเอ็ม) ของภาพที่ได้จากการปรับเปลี่ยนปัจจัยที่มีผลต่อภาพ ที่ภาพ 2 มิติ พบว่าที่ความหนาของสไลด์ 20 และ 30 มม. อาฌาบริเวณขนาด 280 มม. จำนวนการเข้ารหัสเฟส 288 และ 320 ให้รายละเอียดของภาพดีที่สุดสามารถแยกรายละเอียดขนาดเล็กๆได้ ในขณะที่ภาพ 3 มิติ ความหนาสไลด์ที่ 2 และ 3 มม. อาฌาบริเวณขนาด 300 มม. จำนวนการเข้ารหัสเฟส 288 ให้รายละเอียดของภาพดีที่สุดเช่นกัน

กระบอกฉีดยาขนาดเส้นผ่าศูนย์กลาง 10 มม. ถูกนำมาสแกนเพื่อหาอัตราส่วนของสัญญาณที่ได้ ต่อสัญญาณรบกวน (เอสเอ็นอาร์) อัตราส่วนของความคมชัดบนภาพ ต่อสัญญาณรบกวนในภาพ (ซีเอ็นอาร์) และสัญญาณรบกวนก็ถูกนำมาประเมินเช่นกัน ที่ภาพ 2 มิติ พบว่าที่ความหนาของสไลด์ 50 มม. อาฌาบริเวณขนาด 320 มม. จำนวนการเข้ารหัสเฟส 288 ทีอาร์ 6,000 มิลลิวินาที จำนวนสัญญาณเฉลี่ย 4ให้ค่าเอสเอ็น อาร์และซี เอ็น อาร์ สูงที่สุดโดยค่าสัญญาณรบกวนต่ำที่สุด ที่ภาพ 3 มิติความหนาสไลด์ 5 มม. ที่ อาฌาบริเวณขนาด 320 มม. จำนวนการเข้ารหัสเฟส 288 ทีอาร์ 6,000 มิลลิวินาที จำนวนสัญญาณเฉลี่ย 5 ให้ค่าของ เอสเอ็นอาร์ และซีเอ็นอาร์สูงที่สุด และให้ค่าสัญญาณรบกวนต่ำ

การประเมินคุณภาพของการให้สัญญาณเชิงปริมาณและเชิงคุณภาพทั้งในหุ่นจำลองและอาสาสมัครนั้น จะทำการประเมินจากการตรวจหุ่นจำลองและอาสาสมัครจำนวนสิบราย ที่มีร่างกายปรกติ แข็งแรงสมบูรณ์ดี ประกอบด้วยหญิงสองราย และชายแปดราย อายุเฉลี่ย 34.7 ปี ต่ำสุด 25 ปี และสูงสุด 57 ปี สำหรับการประเมินข้อมูลเชิงปริมาณ ทำการวัดรายละเอียดและความเข้มของสัญญาณ (เอฟดับเบิ้ลยูเอชเอ็ม เอสเอ็นอาร์ และ ซีเอ็นอาร์) ส่วนข้อมูลเชิงคุณภาพประเมินโดยรังสีแพทย์หนึ่งท่านที่มีประสบการณ์ในการอ่านภาพจากการตรวจด้วยเครื่องตรวจสนามแม่เหล็กมากกว่าสิบปี จะทำการประเมินจากความสามารถในการแสดงท่อทางเดินน้ำดีหลักๆเจ็ดท่อโดยการให้คะแนนทั้งหมดสองครั้ง นำคะแนนทั้งสองครั้งมาประเมินหาค่าความเชื่อมั่นจากค่าสัมประสิทธิ์สหสัมพันธ์ภายในกลุ่มของสองเครื่องมือ ซึ่งผลที่ได้เชิงปริมาณพบว่าหุ่นจำลองและภาพของระบบท่อทางเดินน้ำดี 2 มิติและ 3 มิติมีคุณภาพของภาพที่แตกต่างกันของเครื่องตรวจด้วยสนามแม่เหล็ก ความเข้ม 0.4 เทสลากับ 3.0 เทสลาอย่างมีนัยยะสำคัญทางสถิติ ค่า p-value น้อยกว่า 0.05 ขณะที่ผลเชิงคุณภาพของภาพโดยรวมที่ภาพ 2 มิติ รังสีแพทย์ประเมินว่ามีความแตกต่างกันในการให้ผลความแตกต่างของการแสดงท่อทางเดินน้ำดี ระหว่างสองเครื่องมือ ค่า p-value น้อยกว่า 0.05 แต่ภาพ 3 มิตินั้นไม่มีความแตกต่างกัน ค่า p-value มากกว่า 0.05 ผลค่าสัมประสิทธิ์สหสัมพันธ์ภายในกลุ่มให้ค่าต่ำสุดที่ 0.61 ที่ภาพ 2 มิติ ของเครื่อง 0.4 เทสลา และค่าสูงสุดที่ 1.00 ที่ภาพ 3 มิติ ของเครื่อง 3.0 เทสลา สรุปจากการศึกษาพบว่า ภาพการตรวจระบบท่อทางเดินน้ำดีจากเครื่องตรวจสนามแม่เหล็กชนิดอุโมงค์เปิด 0.4 เทสลา ด้วยโปรโตคอลที่เหมาะสมโดยรวมนั้น ยังคงให้ความเชื่อมั่นคุณภาพของภาพได้เฉพาะที่ภาพ 3 มิติเท่านั้น

ภาควิชา .....รังสีวิทยา..... ลายมือชื่อนิสิต.....

สาขาวิชา.....ฉายาเวชศาสตร์..... ลายมือชื่อ อ .ที่ปรึกษาวิทยานิพนธ์หลัก.....

ปีการศึกษา.....2553..... ลายมือชื่อ อ. ที่ปรึกษาวิทยานิพนธ์ร่วม.....

5274752030 : MAJOR MEDICAL IMAGING
KEYWORDS : OPEN MRI/ MRI 3.0 T/ MRCP IMAGE QUALITY/ OPTIMIZED PROTOCOL/ MRI CHARACTERISTICS

KRISADANG THASENHOD: OPTIMIZATION PROTOCOLS OF MRCP IMAGING FOR MRI 0.4 TESLA (OPEN) AND COMPARISON IMAGE QUALITY WITH MRI 3.0 TESLA. THESIS ADVISOR: ASSOC. PROF. ANCHALI KRISANACHINDA, Ph.D., THESIS CO-ADVISOR: ASSOC. PROF. SUKALAYA LERDLUM, M.D., 87 pp.

Magnetic resonance imaging (MRI) at high field strength has become more and more frequently used in recent years. The magnetic field strength is a factor affecting the image quality, spatial resolution, signal to noise ratio, contrast to noise ratio and the efficiency to reduce noise. According to the cost of system, type of magnet, cost of maintenance and several examinations, these items are considered in selecting MRI system. For these reasons, Open MRI has been appropriately selected by the hospital with limited budget in purchasing MRI system. Thus, the aim of this study is to assess the feasibility in optimization protocols of MRCP imaging acquired by MRI 0.4 Tesla (Open) and the factors affecting the image quality on MRCP at 0.4 Tesla in comparison to 3.0 Tesla.

The pancreatic duct model made of plastic tube with internal diameter of 2.0 mm was used to determine FWHM (spatial resolution) with parameters affecting the image quality. The improved spatial resolution could be obtained when the slice thickness on 2D image were set at 20 and 30 mm, 280 mm FOV and the number of phase encoding at 288. For 3D images, the best spatial resolution obtained by selecting 2 and 3 mm slice thickness, 300 mm FOV and the number of phase encoding at 288.

The syringe with internal diameter of 10 mm was used to evaluate the SNR, CNR and image noise. For 2D images, the highest SNR and CNR with the lowest noise were obtained at 50 mm slice thickness, 320 mm FOV, the number of phase encoding at 288, TR 6,000 ms, the NSA at 4. For 3D images, the highest SNR and CNR with the lowest noise were obtained at a 5 mm slice thickness, 320 mm FOV, 288 number of phase encoding and NSA at 5.

The quantitative and qualitative assessment had been performed for both phantom and ten healthy volunteers who had been invited to MRCP examination. The normal subjects were 2 female and 8 male with the age range from 25-57 years (mean 34.7 years). The quantitative assessment was assessed from spatial resolution and signal intensity (FWHM, SNR and CNR) and qualitative assessment by one radiologist with experience over ten years was performed by scoring the MRCP images of seven structures for biliary systems with 2 readings. The intra-class correlation coefficient (ICC) was assessed for consistency or reproducibility of qualitative measurements. The results of quantitative study of MRCP image in phantom and on 2D and 3D at 3.0 T showed a higher SNR and CNR ($p\text{-value}<0.05$) than 0.4 T. Overall image quality on 2D MRCP image at 3.0 T was significant improvement than 0.4 T ($p\text{-value} < 0.05$) except 3D imaging ($p\text{-value} >0.05$) showing no significantly different between 0.4 and 3.0 T. The lowest ICC (0.61) is on 2D image 0.4 T and the highest is on 3D image of 3.0 T. Therefore, the overall MRCP imaging at 0.4 T (Open) with optimal protocols could be beneficial in adding up the confidence at 3D images.

Department: .....Radiology..... Student's Signature.....

Field of Study: .....Medical Imaging... Advisor's Signature.....

Academic Year: .....2010..... Co-Advisor's Signature.....

ACKNOWLEDGEMENTS

I would like to express gratitude and deepest appreciation to Associate Professor Anchali Krisanachinda, Ph.D., Division of Nuclear Medicine, Department of Radiology, Faculty of Medicine, Chulalongkorn University, my advisor for her guidance, helpful suggestion, supervision, constructive comments and English language proof of this thesis.

I would like to extremely grateful Associate Professor Sukalaya Lerdlum, M.D. Department of Radiology, Faculty of Medicine, Chulalongkorn University, my co-advisor and staff of MRI unit for her helpful suggestion, constructive comments, devoted her time to review the clinical part and encouragement the Ratchadapiseksompotch Fund from Faculty of Medicine, Chulalongkorn University.

I would like to extremely grateful Associate Professor Sivalee Suriyapee, Chief Physicist at Division of Radiation Oncology, Department of Radiology, Faculty of Medicine, Chulalongkorn University, my teacher for her invaluable advices, constructive comments in this research.

I would like to deeply thank Associate Professor Somjai Wangsuphachart, M.D., Department of Radiology, Faculty of Medicine, Chulalongkorn University, for her helpful suggestion, constructive comments in this research.

I would like to thank Associate Professor Kiat Arjhansiri, M.D., Head of Department of Radiology, Faculty of Medicine, Chulalongkorn University, and Dr. Siripan Kalayanaruj, Department of Radiology, Rajavithi Hospital for providing the required equipment to perform this research.

I am extremely grateful to Mr. Wallop Makmool, Department of Radiology, King Chulalongkorn Memorial Hospital to his instruction of using the machine, and devoted his time to acquire volunteers in clinical part in this research.

I would like to thank Professor Franco Milano from University of Florence Italy, who is the external examiner of the thesis defense for his helpful recommendation, constructive comments and teaching of knowledge in Medical Imaging.

Finally, I am extremely grateful for all teachers, lecturers and staffs at Master of Science Program in Medical Imaging, Faculty of Medicine, Chulalongkorn University for their helps, and unlimited teaching of knowledge during the course in Medical Imaging. My grateful is forwarded to the Graduate Studies for supply the knowledge as tutor, especially, Mrs. Petcharleeya Suwanpradit for her contribution in part QC phantom , Mr. Kitiwat Khamwan for every suggestions and all MRI Technologists at King Chulalongkorn Memorial Hospital for their kind supports.

CONTENTS

LIST OF TABLES

LIST OF FIGURES

Figure **Page**

LIST OF ABBREVIATIONS

ABBREVIATION	TERMS
2D	Two dimensions
3D	Three dimensions
AAPM	American Association of Physicists in Medicine
AP	Anterior to Posterior Direction
B0	Main Magnetic field strength
Bkg	Background
CBD	Common Bile Duct
CHD	Common Hepatic Duct
CI	Confidence Interval
CNR	Contrast to Noise Ratio
CT	Computed Tomography
CyD	Cystic Duct
ERCP	Endoscopic Retrograde Cholangiopancreatography
FA	Flip Angle
FOV	Field Of View
Freq.	frequency
FRFSE	Fast Recovery Fast spin Echo
FSE	Fast Spin Echo
FWHM	Full Width at Half Maximum
G	Gauss
GB	Gall bladder
GRE	Gradient Echo
HASTE	Half-fourier Acquisition Single-shot Turbo spin Echo
HF	Head to Feet Direction
K	Kelvin
kHz	Kilohertz
LHD	Left Hepatic Duct
MIP	Maximum Intensity Projection
mm	Millimeter
MRCP	Magnetic Resonance Cholangiopancreatography
MRI	Magnetic Resonance Imaging
NEX	Number of Excitations
NIH	National Institute of Health
NSA	Number of Signals Averaged
PD	Proton Density
PaD	Pancreatic duct
Phase#	Number of phase
T	Tesla
PTC	Percutaneous Trans-hepatic Cholangiography
QC	Quality Control
RARE	Rapid Acquisition by Relaxation Enhancement

ABBREVIATION	TERMS
RF	Radiofrequency
RHD	Right hepatic duct
RL	Right- Left Direction
ROI	Region Of Interest
SD	Standard Deviation
SE	Spin Echo
SENSE	SENSitivity Encoding
SI	Signal Intensity
SNR	Signal to Noise Ratio
SSFP	Steady-State Free Precession
SSFSE	Single-Shot Fast Spin Echo
T1	T1 Weighted Image
T2	T2 Weighted Image
TE	Echo Time
TSE	Turbo Spin Echo
TR	Repetition Time

CHAPTER I

INTRODUCTION

1.1 Background and Rationale

Magnetic resonance imaging (MRI) at field strength of 3.0 Tesla has become more and more frequently use in recent years. An increasing number of 3.0 Tesla MRI system for clinical imaging replaces 1.5 Tesla and lower field strength system using in the past.

MRI has been classified by magnet field strength, but is now classified in two streams-high magnetic fields MRI and Open MRI. As MRI is excellent in tissue-contrast, its imaging objects include in addition to cerebral spine area and orthopedics area as well as circulating organs of cardiovascular system recently, thus expanding to whole body. Flow of inspection by leaving established diagnosis to MRI is becoming standard [1].

In selecting an MRI system, the cost of system, cost of maintenance and cases for examination are considered. Open MRI has shown a rapid expansion in USA since 1995 and on. The major reasons are: firstly, there are many big patients who cannot enter the tunnel type MRI, secondly, increasing number of claustrophobia patients, the need for more comfortable, less anxious for MRI examination in addition, application approach to therapy of lesions by interventional MRI including MRI guided biopsy and therapy [1]. For these reasons, Open MRI is appropriately selected in purchasing MRI system.

Magnetic resonance cholangiopancreatography (MRCP) is increasingly reliable in the evaluation of biliary pathology, pancreatic disorders and anatomical variations of the biliary tree (Figure 1.1). Its main advantage over conventional endoscopic retrograde cholangiopancreatography (ERCP) is that it is a non-invasive imaging modality [2]. Recent studies reported a high accuracy in depicting choledocholithiasis and other causes of biliary and pancreatic duct obstruction, with a good correlation with the results of ERCP and percutaneous trans-hepatic cholangiography (PTC) [5-6].

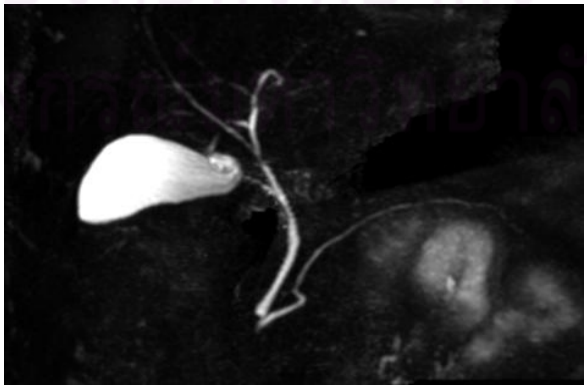

Figure 1.1 The MRCP imaging

The spatial and contrast resolutions of MRCP imaging are important for detecting small pathologies, such as small stones and mural nodules in pancreatic cystic lesions, and evaluating anatomy, such as the biliary tree in a normal liver donor population. Image quality in MRI of the abdomen has been improved by recent technical developments, such as a more powerful gradient system, receiver coils, and the use of parallel-imaging and respiratory-monitoring techniques [3]. Despite these technical improvements, however, the quality of MRCP imaging for evaluating small changes and anatomy remains limited at low field strength because of its poorer spatial resolution and signal-to-noise ratio (SNR).

MRCP image quality was compared for low and high field strengths (1.0-3.0 T) with different acquisition modalities. Both breath-hold and non-breath-hold sequences were reported in the literatures, with similar different results [2-4]. But to our knowledge, there has been no previous published in comparing MRCP between 0.4 Tesla and 3.0 Tesla.

Thus, the aim of this study is to assess the feasibility optimization MRCP imaging acquired by MRI 0.4 Tesla (Open) and to compare the obtained MRCP image acquired by the optimized protocol with the image from 3.0 Tesla.

1.2 Research Objectives

1.2.1) To determine the optimal protocols of MRCP imaging acquired by MRI 0.4 Tesla (Open) and compare image quality with MRI 3.0 Tesla.

1.2.2) To study the image quality (spatial resolution and SNR) in phantom for MRI 0.4 Tesla (Open) and 3.0 Tesla.

CHAPTER II

REVIEW OF RELATED LITERATURES

2.1 Theory

2.1.1 The introduction of MRI [7]

Magnetic resonance imaging (MRI) has been well established as both a diagnostic and research tool in many areas of medicine because of its ability to provide excellent soft-tissue delineation of different areas of interest. For example, the brain, T1- and T2-weighted MR imaging has evolved to be the standard of reference for anatomic definition. These sequences derive image contrast from the spin density in water and fat and from the MR relaxation parameters T1 and T2. Unfortunately, the water and fat spin densities yield only limited information and present difficulty in separating adipose tissue from non adipose tissue unless fat saturation is employed. These relaxation parameters can be used in a wide variety of T1- and T2-weighted sequences to optimize contrast for specific diagnostic purposes. T2 provides information about edema within the brain.

Altering the MR image contrast with an intravascular contrast agent typically reveals physiologic changes in tissue that are relevant to disease processes. For example, contrast agents, such as gadolinium, administered to the bloodstream create more contrast in highly vascular regions and are retained in regions where the permeability of the interstitial space has changed. These types of changes in vascularity or tissue permeability occur in a variety of diseased tissues, such as malignant tumors and myocardial ischemia.

MR imaging plays an increasingly important role in diagnostic imaging of different pathologic disorders, where the goal is developing radiological imaging markers for noninvasive prediction of disease and response to treatment. For example, MR imaging used in oncologic imaging consists of anatomic T1 and T2-weighted sequences, dynamic contrast material enhancement or MR spectroscopy in the brain, breast and prostate. Dynamic contrast enhancement with gadolinium yields information on the vascular status of a lesion, and MR spectroscopy probes the intracellular (e.g. choline, creatine) environment of tissue. When these sequences are combined, they can assist the physician in making the diagnosis or monitoring the treatment regimen.

One of the major advantages of the MR imaging is the ability to manipulate image contrast with a variety of selectable parameters affecting the quality of the information provided. Therefore, this study reviews the elements used to obtain MR images and the factors affected the MR image specifically, instrumentation, localization of the MR signal, gradients, k-space, and pulse sequences as well as emerging applications in high-field-strength MR imaging.

2.1.2 MR Instrumentation

MR images require a sophisticated combination of electronics, radiofrequency (RF) generators, coils, and gradients that interface with a computer for communication between different electronics. This combination of equipment allows localization, excitation, and acquisition of a specific tissue of interest and formation of

a digital image. There are two parts of equipment combined to form the MR system. The first part is the command and control center, that is, the computer, interface, and data storage. The second part is specialized equipment that generates and receives the MR signal, that is, the magnet, gradients, and RF coils (Figure 2.1).

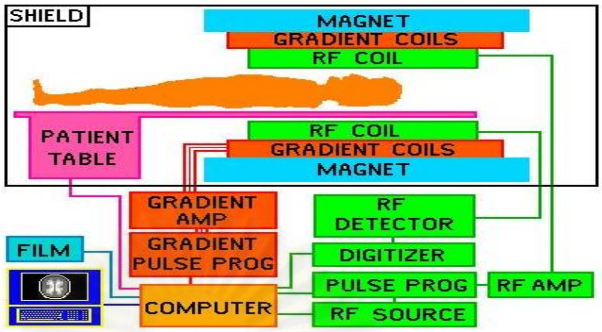

Figure 2.1 Basic components of MRI system (www.fas.org/irp/imint/docs/rst/I...26c.html).

2.1.3 Magnets

The magnet provides the "external" magnetic field in which the patient or object is placed, and its performance requirements are usually defined in terms of field strength, stability, and homogeneity. There are three types of magnets that can be used in MR imaging: permanent, resistive, and superconducting.

(a) Permanent Magnets

Permanent magnets exploit the ferromagnetic properties of the metal used (e.g. iron, nickel, or other metals). They are configured differently from superconducting magnet (Figure 2.2 (B)). Specifically, the main magnetic field (B0) of a permanent magnet is perpendicular to the object of interest (vertical magnetic field) that runs between the two magnetic poles (Figure 2.2 (A)). Early permanent magnets are very heavy of 5–100 tons. However, newer versions are lighter and are sometimes used for limited clinical applications such as open magnets (Figure 2.3). Advantages of permanent magnets are that they require no cooling or power to run and thus are lower cost than other magnets. However, they cannot be turned off in emergencies and have less field homogeneity.

(A)

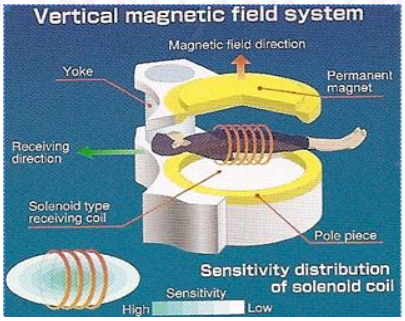

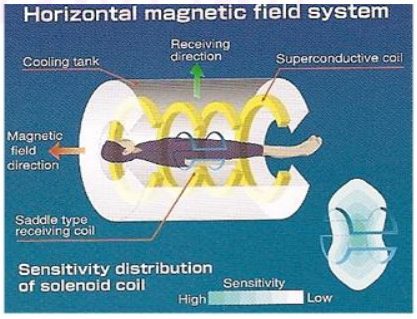

(B)

Figure 2.2 Magnetic field system of permanent (vertical magnetic field system, A), superconducting (Horizontal magnetic field system, B)

Figure 2.3 Open MRI magnet (Aperto presentation, Hitachi Company)

Open MRI system is much more patient friendly than restricted tunnels of super conducting systems, offering the possibility of MRI-guide interventional procedures, because the physician is able to access to the patient during scanning. Open MRI systems are based on either permanent or iron-cored electromagnet designs.

(B) Resistive Magnets

When an electric current flows through a wire, the magnetic field is induced around the wire, this principle is used for construction of a resistive magnet. Resistive magnets require cooling and power to operate but can be turned off and on. Their field strengths range from 0.1 T to 0.3 T with the disadvantages of poor homogeneity and high electrical costs. Also, the object of interest lies perpendicular to the B0 field, and the usual application is similar to that of permanent magnets in the "open magnet" configuration.

(C) Superconducting Magnets

Superconducting magnets are based on the principle of cooling down to 4°K for certain metal conductors so that there is little or no resistance; therefore, a high electric current can be used to generate high magnetic field strength with no major heat disposition. However, in order to achieve small electrical resistance, expensive cooling cryogens, usually liquid helium are used. Currently, most clinical systems use superconducting magnets with field strengths of 0.5–3.0 T; most field strengths on the order of 1.5–3.0 T. Research magnets (clinical or experimental) can have field strengths of 4.0–9.4 T.

2.1.4 Field Strength

The field strength of an MR system is a major determinant of the image contrast due to the energy exchange between the protons (water) and their environments. These interactions are governed by the magnetic moments of the protons, in particular the longitudinal relaxation parameter T1. The time required for complete relaxation differs for different field strengths; for example, the T1 is shorter at lower field strengths and tends to increase at higher field strengths. These changes affect both the signal and contrast-to-noise ratios of MR images. The units of field

strength of an MR system are tesla or gauss which 1 T equals to 10,000 G. The range of magnetic field strength is variable, from low (0.1– 0.5 T), medium (0.5–1.0 T), high (1.5 T) to ultrahigh (3.0 T or greater). Although there have been vast technological advances in MR imaging over the past 40 years, the principle for advancing the MR imaging technology has been based on finding ways to increase signal to noise ratio (SNR) in the MR image or spectra. The most fundamental approach to boosting SNR is to increase the field strength of the MR magnets. As a result, human MR imaging is currently performed at field strengths 4 T, 7 T, 8 T, and 9.4 T.

2.1.5 Tissue Contrast [8]

All MR images are of some degree affected by each of the parameters that determine tissue contrast such as T1, T2, proton density and the TR and TE can be adjusted to emphasize a particular type of contrast. This may be done, for example, with T1 weighting. Table 2.1 describes the parameters used to obtain images with T1, T2, and proton-density weighting. T1-weighted images best depict the anatomy, and if contrast material is used, they also may show pathologic entities; however, T2-weighted images provide the best depiction of disease, because most tissues involved in a pathologic process have a higher water content than in normal, and the fluid causes the affected areas to appear bright on T2- weighted images. Proton-density weighted MR images usually depict both the anatomy and the disease entity. Table 2.2 shows typical TR and TE values that may be used to achieve different weighting with Spin echo (SE) and Gradient echo (GRE) sequences.

Table 2.1 Effect of TR and TE on MR Image Contrast

Imaging Technique	TR	TE
T1 weighting	Short	Short
T2 weighting	Long	Long
Proton-density weighting	Long	Short

Table 2.2 Typical TR and TE Values for SE and GRE Sequences

Sequence	TR (ms)		TE (ms)	
	Short	Long	Short	Long
SE	250–700	>2000	10–25	>60
GRE	<50	>100	1–5	>10

2.1.6 Image characteristics [9]

(A) Tissue Characteristics

For the imaging process, three tissue characteristics: PD, T1, and T2 are used to show valuable information about the tissues. These characteristics become visible because each one has an effect on the level of magnetization present at the picture snapping time in each imaging cycle.

PD (Proton Density): PD has a very direct effect on tissue magnetization, the resulting RF signal and image brightness. That is because the magnetization is produced by the protons. Therefore, a tissue with a high PD can reach a high level of magnetization and produce an intense signal.

T1: When the imaging protocol is set to produce a T1-weighted image, it is the tissues with the short T1 values that produce the highest magnetization and brightness on the image.

T2: When the imaging protocol is set to produce a T2-weighted image, it is the tissues with the long T2 values that produce the highest brightness, because of the higher level of magnetization at the picture snapping time.

(B) Spatial Characteristics

Figure 2.4 illustrates the basic spatial characteristics of the MR image. MRI is basically a tomographic imaging process, although there are some procedures, such as angiography, in which a complete anatomical volume will be displayed in a single image. The protocol for the acquisition process must be set up to produce the appropriate spatial characteristics for a specific clinical procedure. This includes the number of slices, slice orientation, and the structure within each individual slice.

Slices: A typical examination consists of at least one set of contiguous slices. In most cases the entire set of slices is acquired simultaneously. However, the number of slices in a set can be limited by certain imaging factors and the amount of time allocated to the acquisition process.

The slices can be oriented in virtually any plane through the patient's body. The major restriction is that images in the different planes cannot generally be acquired simultaneously. For example, if both axial and sagittal images are required, the acquisition process must be repeated. However, there is the possibility of acquiring 3-D data from a large volume of tissue and then reconstructing slices in the different planes.

Voxels: Each slice of tissue is subdivided into rows and columns of individual volume elements, or voxels. The size of a voxel has a significant effect on image quality. It is controlled by a combination of protocol factors and should be adjusted to an optimum size for each type of clinical examination. Each voxel is an independent source of RF signals. That is why voxel size is a major consideration in each image acquisition.

Image Pixels: The image is also divided into rows and columns of picture elements, or pixels. In general, an image pixel represents a corresponding voxel of tissue within the slice. The brightness of an image pixel is determined by the intensity of the RF signal emitted by the tissue voxel.

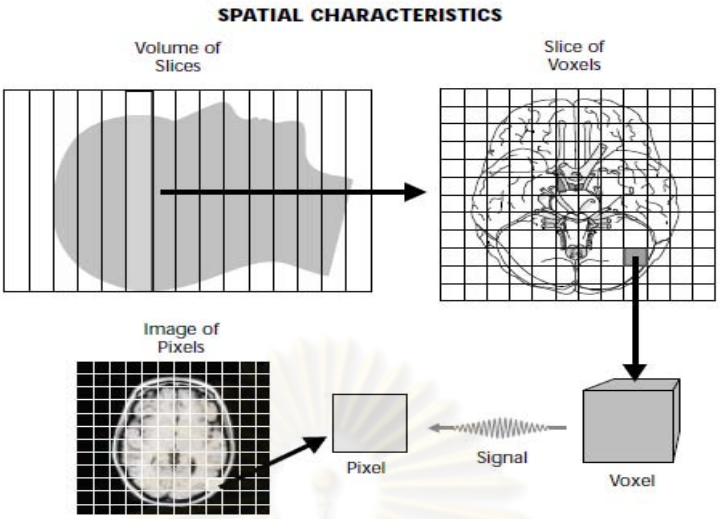

Figure 2.4 The spatial characteristics of MR images [9].

2.1.7 Image Quality Characteristics

The MRI system has tremendous been controlled over the characteristics and the quality of the images that are produced. The five basic image quality characteristics are spatial, detail, contrast sensitivity, noise and image artifact as shown in Figure 2.5. Each of these image characteristics is affected by a combination of the imaging factors that make up the acquisition protocol.

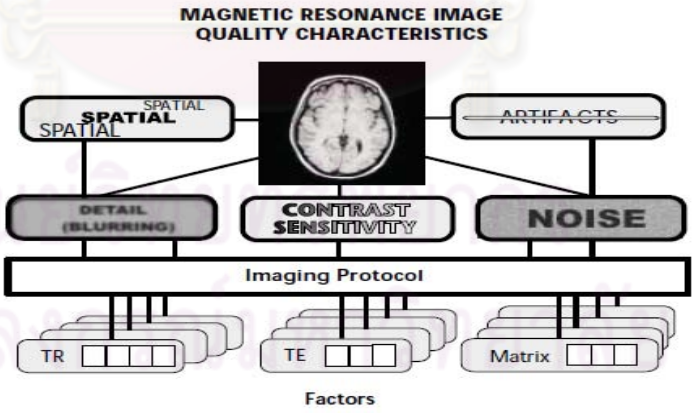

Figure 2.5 Image quality characteristics controlled by the selection of protocol parameters [9].

Not all types of clinical procedures require images with the same characteristics. Therefore, the primary objective is to use an imaging protocol in which the acquisition process is optimized for a specific clinical requirement.

Contrast Sensitivity: Contrast sensitivity is the ability of an imaging process to produce an image of objects or tissues in the body that have relatively small physical differences or inherent contrast. The contrast that is to be imaged is in the form of some specific physical characteristic. In x-ray imaging, including CT (computed tomography), difference in physical density is a principle source of contrast. One of the major advantages of MRI is a high contrast sensitivity for visualizing differences among the tissues in the body because there are several sources of contrast; that is, it has the ability to image a variety of characteristics (PD, T1, T2). Also, there is usually much greater variation among these characteristics than among the tissue density values that are the source of contrast for x-ray imaging. If a certain pathologic condition does not produce a visible change in one characteristic, there is the possibility that it will be visible by imaging some of the other characteristics.

Even though MRI has high contrast sensitivity relative to the other imaging modalities, it must be optimized for each clinical procedure. This includes the selection of the characteristics, or sources of contrast, that are to be imaged and then adjusting the protocol factors so that the sensitivity to that specific characteristic is optimized. This is illustrated in Figure 2.6.

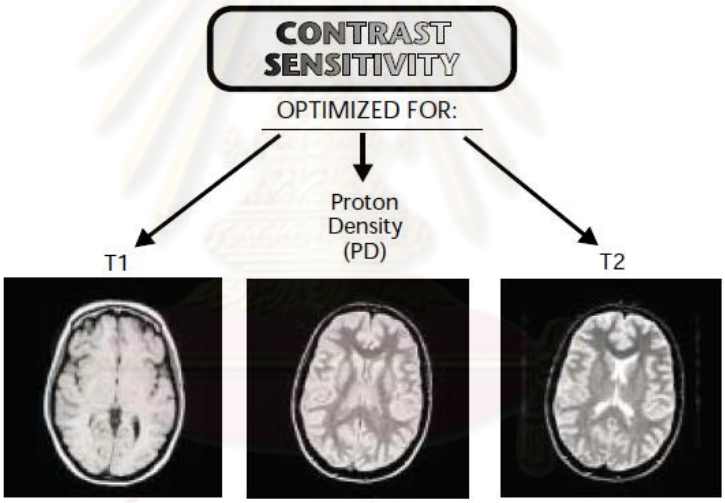

Figure 2.6 The images produced when the contrast sensitivity is optimized for each of the three specific tissue characteristics [9].

Detail: A distinguished characteristic of every imaging modality is its ability to image small objects and structures within the body. Visibility of anatomical detail (sometimes referred to as spatial resolution) is limited by the blurring that occurs during the imaging process. All medical imaging methods produce images with some blurring but not to the same extent. The blurring in MRI is greater than in radiography.

In MRI, like all modalities, the amount of blurring and the resulting visibility of detail can be adjusted during the imaging process. Figure 2.7 shows images with different levels of blurring and visibility of detail.

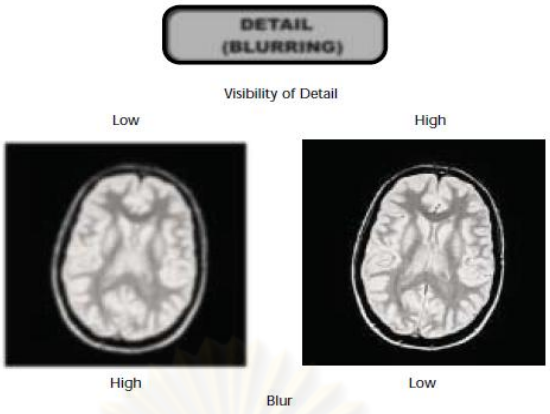

Figure 2.7 Images with different levels of blurring and visibility of anatomical detail [9].

Noise: Visual noise is a major issue in MRI. The presence of noise in an image reduces its quality, especially by limiting the visibility of low contrast objects and differences among tissues. Figure 2.8 shows the images with different levels of visual noise. Most of the noise in MR images is the result of random, unwanted RF energy picked up from the patient's body. The amount of noise can generally be controlled through a combination of factors. However, many of these factors involve compromises with other characteristics.

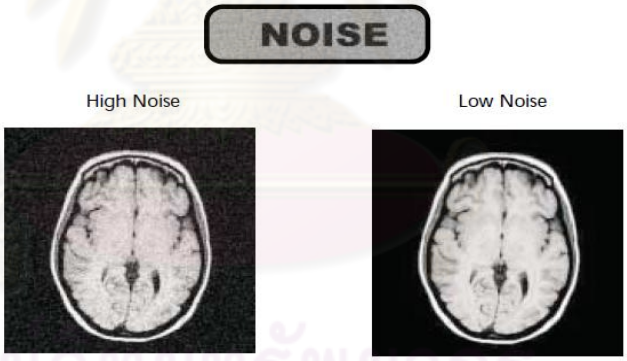

Figure 2.8 Images with different levels of visual noise [9].

Artifacts: Artifacts are undesirable objects, such as streaks and spots appear in images which do not directly represent an anatomical structure. They are usually produced by certain interactions of the patient's body or body functions (such as motion) with the imaging process. There is a selection of techniques that can be used to reduce the presence of artifacts.

Spatial: The general spatial characteristics of the MR image were described previously. However, when setting up an imaging protocol the spatial characteristics must be considered in the general context of image quality. The voxel size plays a major role in determining both image detail and image noise.

2.1.8 MRI image quality

An MR exploration is a compromise between scan time and image quality. An MR exploration protocol and its sequence parameters will be optimized in function of the organs and pathology.

The MR image quality depends on several factors:

- Spatial resolution and image contrast
- Signal to noise ratio (SNR)
- contrast to noise ratio (CNR)
- Artifacts

Spatial resolution: Spatial resolution corresponds to the size of the smallest detectable detail. The smaller the voxels are, the higher the potential spatial resolution. Voxel size is determined by slice thickness, FOV and matrix size as shown in figure 2.9.

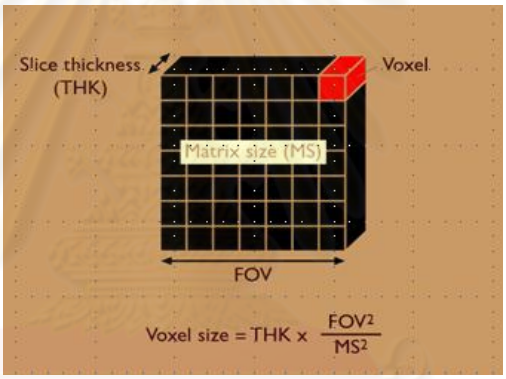

Figure 2.9 The relationship between the voxel size with matrix size and slice thickness (understanding MRI: Philips).

As the slice thickness is increased the signal intensity increases and the SNR is improved. But the impact of partial volume effect is increased also. If the slice thickness decreases the spatial resolution is improved. The voxel size can be determined by the equation:

$$\text{Voxel size} = \text{slice thickness} \times \frac{(\text{Fiew of view})^2}{(\text{Matrix size})^2} \quad (1)$$

As FOV increases the SNR is improved. The area depicted in a pixel is enlarged and the proton contained in the area increases causing the signals increase as in figure 2.10.

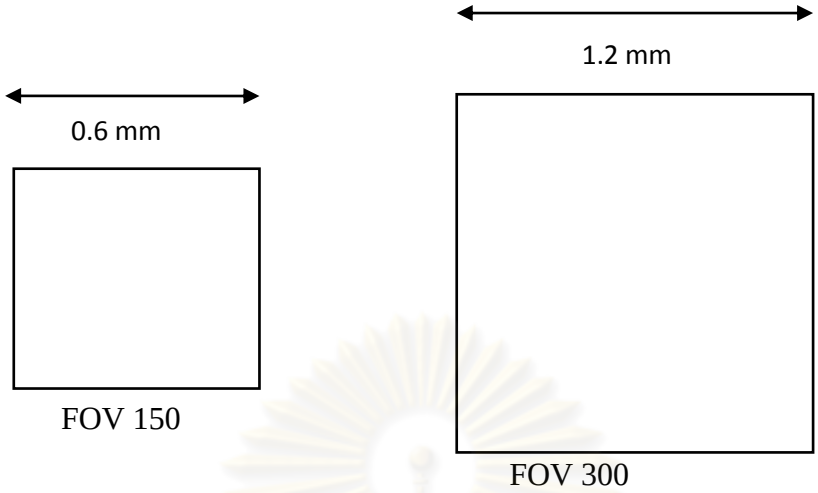

Figure 2.10 Difference of pixel size due to difference of FOV, in case of the number of frequency 256 and phase 256.

As frequency encoding or phase encoding increases the spatial resolution is improved. As frequency encoding or phase encoding decreases the SNR is improved because the pixel size becomes large and signal intensity increases, but the impact of partial volume effect increases also as in figure 2.11.

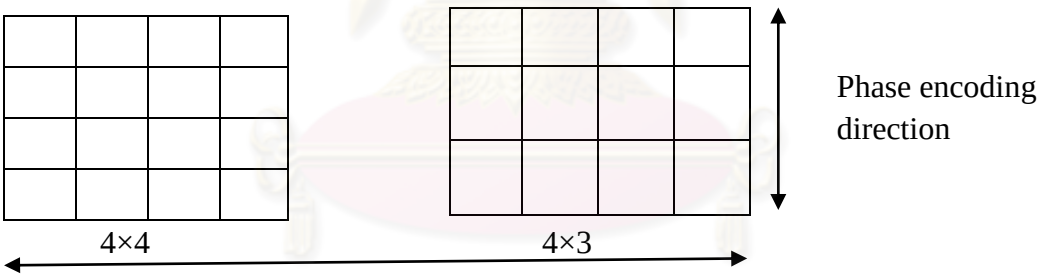

Figure 2.11 The relationship between number of matrix in the frequency and phase encoding

The spatial resolution in MRI could be measured as the full width at half maximum (FWHM). The technical term FWHM is used to describe a measurement of the width of an object in a picture, when that object does not have sharp edges. A simple box can be described just by its width and a rectangle by its width and height.

It is a simple and well-defined number which can be used to compare the quality of images obtained under different observing conditions. The FWHM gives a good condition of spatial resolution in MRI the same as the modulation transfer function (MTF) in CT [16]. The normalized FWHM is shown as in figure 2.12

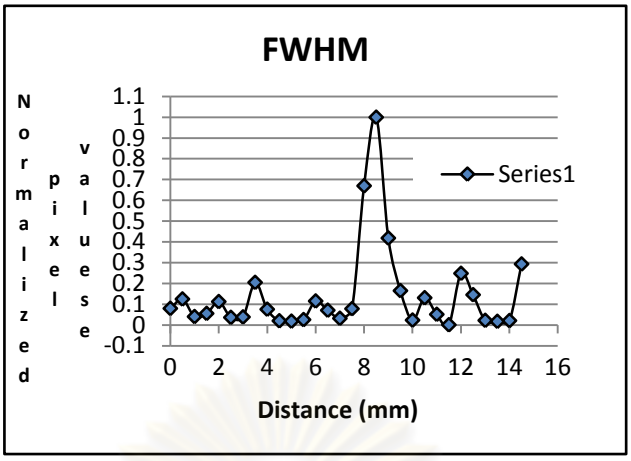

Figure 2.12 The normalized FWHM

Signal to noise ratio (SNR): The signal to noise ratio (SNR) is equal to the ratio of the average signal intensity over the standard deviation or the noise. Noise is like interferences which present as in irregular granular pattern. This random variation in signal intensity degrades image information. The main source of noise in the image is the patient's body and the MR scanner. This noise corrupts the signal coming from the transverse magnetization variations of the intentionally excited spins on the selected slice plane.

The signal to noise ratio depends not only on MR scanner specifications, and pulse sequence design but also on factors that the user can change, voxel size, the number of signal average (NSA), number of phase encoding and the receiver bandwidth which determined by the equation:

2D SNR α Sequence×$voxel_{x,y,z}$ ×$\frac{\sqrt{NSA \times Number\ \ of\ phase\ (y)}}{\sqrt{Bandwidt\ h}}$ ×coil type× magnetic field× reconstruction algorithms ; where y is phase encoding in the y direction (2)

3D SNR α Sequence×$voxel_{x,y,z}$ ×$\frac{\sqrt{NSA \times Number\ \ of\ phase\ (y,z)}}{\sqrt{Band\ widt\ h}}$ ×coil type× magnetic field× reconstruction algorithms; where y and z are phase encoding in y and z direction (3)

The fixed factors are static field intensity, pulse sequence design, tissue characteristics and the controllable factors are RF coil, sequence parameters, voxel size, number of signal average, receiver bandwidth and reconstruction algorithms.

RF coil: The smaller the sensitive volume of a coil, the lower the noise from the adjacent structures of the selected slice plane which it can detect, and the better the signal to noise ratio will be. A local coil, or better, a surface coil has a higher signal to noise ratio than a body coil.

Voxel size: The signal comes from the excited protons on the selected slice plane. The number of spins in parallel state in excess is proportional to the static magnetic field intensity. The larger the field intensity is, the higher the excess number of spins in parallel state (available to make the MR signal) will be. Thus, the signal intensity varies almost linearly with the main field intensity. Assuming a uniform

proton density, the number of excited spins is proportional to the voxel size and so is the signal intensity. The signal goes up linearly with the voxel size.

Number of signal averaging (NSA)

When the number of signal averaging for the same slice increases: The signal is identical for each measure. The noise is random and is not the same for each measure. Therefore, the signal sum goes up linearly with the number of excitations but the noise only goes up with the square root of the number of excitations. In other words, the average signal remains constant, but the average noise goes down with the square root of the number of excitations. The signal to noise ratio goes up with the square root of the number of excitations (Figure 2.13).

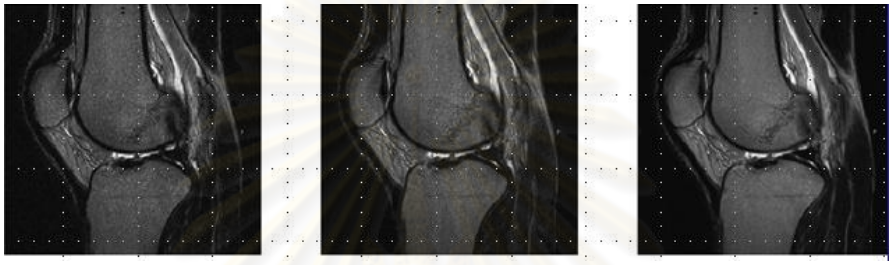

NSA=1 NSA=2 NSA=4

Figure 2.13 Increasing the NSA the SNR is improved (understanding MRI: Philips)

Receiver bandwidth: Given a voxel size and static field strength, the number of excited spins is defined and so is the amount of MR signal. The readout of the MR signal can take more or less time, depending on the receiver bandwidth. The relation between the receiver bandwidth and the strength of the readout gradient is such that:

A broad bandwidth corresponds to a fast sampling of the MR signal and a high-intensity readout gradient. A narrow bandwidth corresponds to a slow sampling of the MR signal and a low-intensity readout gradient (Figure 2.14).

Background noise has a constant intensity at all frequencies (white noise). Therefore, the larger the receiver bandwidth is, the more noise is recorded (and the higher is the readout gradient intensity and the faster the MR signal is sampled).

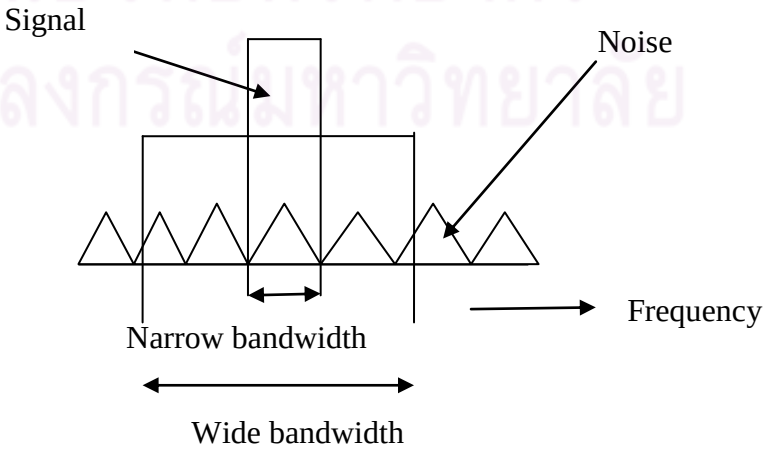

Figure 2.14 The frequency bandwidth (kHz) of receiving signals.

The SNR is inversely proportional to the square root of bandwidth. Accordingly, when bandwidth is narrow, the noise component in an image decreases to improve the SNR.

Magnetic field strength: Magnetic field strength influences the SNR of the image by a factor of $B^{1.0}$ to $B^{1.5}$. Thus, one would expect a three- to fivefold improvement in SNR with a 1.5 T magnet over a 0.5 T magnet. Although the gains in the SNR are real, other considerations mitigate the SNR improvement in the clinical environment, including longer T1 relaxation times and greater RF absorption.

Image acquisition and reconstruction algorithms: Image acquisition and reconstruction algorithms have a profound effect on SNR. The various acquisition/reconstruction methods such as point acquisition methods, line acquisition methods, two-dimensional Fourier transform acquisition methods, and three-dimensional Fourier transform volume acquisition methods are to increase SNR. In each of these techniques, the volume of tissue that is excited is the major contributing factor to improving the SNR and image quality, Reconstruction filters and image processing algorithms will also affect the SNR. High-pass filtration methods that increase edge definition will generally decrease the SNR, while low-pass filtration methods that smooth the image data will generally increase the SNR at the cost of reduced resolution.

Contrast to noise ratio (CNR): This is defined as difference in the SNR between two adjacent areas. It is controlled by same factors that affect SNR. The figure 2.15 are illustrated the simple mathematical definition of SNR and CNR.

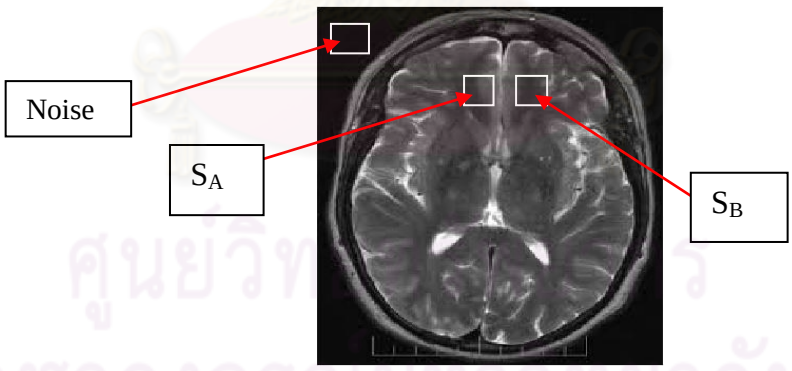

Figure 2.15 Definitions of contrast, signal to noise ratio, contrast to noise ratio (where, S is signal intensity) [16]

$$SNR_A = \frac{S_A}{Noise} \quad , CNR_{AB} = \frac{S_A - S_B}{Noise} \tag{4}$$

Artifact: Artifacts often corrupt MRI images. An image artifact is any feature which appears in an image which is not present in the original imaged object. An image artifact is sometime the result of improper operation of the imager, and other times a consequence of natural processes or properties of the human body. It is

important to be familiar with the appearance of artifacts because artifacts can obscure, and be mistaken for, pathology. Therefore, image artifacts can result in false negatives and false positives. Artifacts are typically classified as to their source, and there are dozens of image artifacts. The following table 2.3 shows type of artifact and the cause.

Table 2.3 MRI image artifacts

Artifact	**Cause**
RF Offset and Quadrature Ghost	Failure of the RF detection circuitry
RF Noise	Failure of the RF shielding
B_o Inhomogeneity	Metal object distorting the B_o field
Gradient	Failure in a magnetic field gradient
Susceptibility	Objects in the FOV with a higher or lower magnetic susceptibility
RF Inhomogeneity	Failure or normal operation of RF coil, and metal in the anatomy
Motion	Movement of the imaged object during the sequence
Flow	Movement of body fluids during the sequence
Chemical Shift	Large B_o and chemical shift difference between tissues
Partial Volume	Large voxel size
Wrap Around	Improperly chosen field of view
Gibbs Ringing	Small image matrix and sharp signal discontinuities in an image

2.1.9 Protocol Optimization

An optimum imaging protocol is designed for the balance among the image quality characteristics and acquisition time. The imaging protocol used for a specific clinical examination has a major impact on the quality of the image, the visibility of anatomical structures and pathologic conditions.

Image acquisition Time: MR image quality is affected by the time required for the acquisition process. In general, the detail and noise can be improved by using longer acquisition times. In the basic acquisition time required is TR multiplied by matrix size in phase encoding direction and number of signal average.

$$\text{Time} = \text{TR} \times \text{phase encoding} \times \text{NSA} \quad (5)$$

Matrix size: The matrix size and the FOV are the two factors that determine voxel size in the plane of image. Voxel size determines the amount of blurring and image detail. Small voxel and minimum blurring required for good detail. If the matrix size is reduced without changing the FOV, voxel size will be increased and there will be reduction in image detail.

It is only the matrix size in the phase encoded direction that has an effect on acquisition time. This matrix dimension determines the number of row of k-space that must be filled.

Reduced matrix in phase-encoded direction: One approach to optimizing an acquisition is to reduce the matrix size in phase encoded direction to a value that is less than the matrix size in the frequency encoded direction. These selectable basic matrix sizes are binary multiplies such as 128, 256, 512, and 1024. When basic matrix size is selected, it is one of these values, with 256 being the most common for most procedures. When the matrix size is reduced by some percentage in the phase encoded direction, the computer fill in the unused row of k space with zeros to make the reconstruction process work.

Rectangular field of view: Decrease matrix size without changing the FOV does produce an increased voxel size. However, if the FOV can be reduced in phase encoded direction, the voxel size will be decreased and image detail will be maintained. The use of rectangular FOV is a way of optimizing acquisition time and image detail if a rectangular FOV works for the specific anatomical region that is being image. By combining a reduced matrix size in phase encoded direction with a rectangular FOV, acquisition time can be reduced without affecting image quality. This is one step in optimizing a procedure.

Half acquisition: This method might be referred to by names such as *half scan* and *half Fourier*. When using the half acquisition method only the first half of k space is filled directly. Then, the data that was acquired during the first half is mathematically "flipped" and used to fill the second half of k space. This makes it possible to fill all of the rows of k space in approximately half of the normal acquisition time. The actual acquisition time will be slightly more than half because there must be some overlap in the data to make this process work. This is a method that can be used to reduce acquisition time. However, it results in an increase in image noise because the image is being formed with a smaller number of acquisition signals.

Signal averaging: The averaging is achieved by repeating the cycle several times for each phase-encoding step. This process does not change the number of phase-encoding step required. But it does increase the number of cycles in the acquisition. For example if the NSA protocol factor is set to 4. The cycle for each phase encoding step is repeated four times and the total acquisition time is increased by a factor of 4.

Developing an optimized protocol: An acquisition protocol can be rather complex because of the large number of factors that must be adjusted and the interaction of many of the factors with different image quality characteristics and acquisition time. One approach to develop a good protocol is to address the specific image characteristics in this order: Contrast sensitivity**,** Image detail**,** Spatial Characteristics and methods**,** Image Noise and Artifact Reduction

2.1.10 Magnetic resonance cholangiopancreatography (MRCP)

Magnetic resonance cholangiopancreatography (MRCP) is a special type of magnetic resonance imaging (MRI) that produces detailed images of the hepatobiliary and pancreatic systems, including the liver, gallbladder, bile ducts, pancreas and pancreatic duct. These may include tumors, stones, inflammation or infection. MRCP is used to evaluate patients with pancreatitis to detect the underlying cause, help

diagnose unexplained abdominal pain, and a less invasive alternative to endoscopic retrograde cholangiopancreatography (ECRP). ERCP is a diagnostic procedure that combines endoscopy, which uses an illuminated optical instrument to examine inside the body, with radiographic- fluoroscopic system. Figure 2.16 shows the images of MRCP (a) and the anatomical structure of biliary system (b).

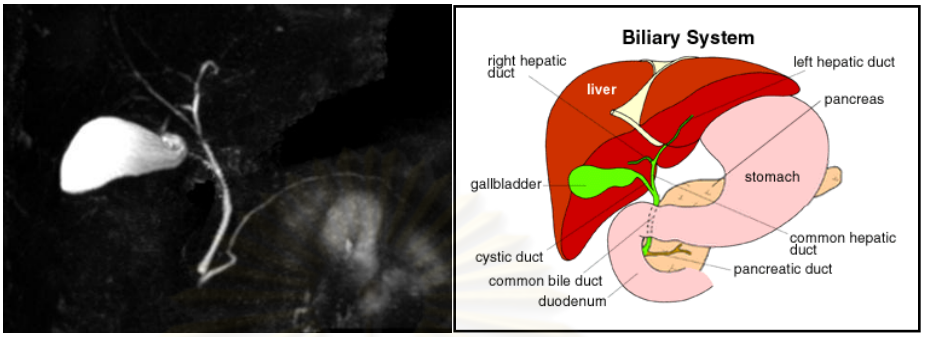

(a) (b)

Figure 2.16 The MRCP imaging (a), the anatomical structure of biliary system (b)

Advantages and Disadvantages of MRCP [15]

MRCP is non-invasive procedure provided patients with adequately screened for contraindications. In addition, MRCP does not require radiation exposure, intravenous contrast agents, or a highly skilled operator. MRCP is less expensive and can be performed on an outpatient basis with an excellent inter-observer agreement.

Major disadvantages of MRCP compared to ERCP include: lack of immediate therapeutic solution and inability to obtain tissue for diagnosis, inability to provide information about the rate of biliary drainage, a lower spatial resolution and lack of distension by contrast limits visualization of non-dilated peripheral bile ducts and assessment of stricture morphology, claustrophobia and the inability to evaluate patients with pacemakers or ferro-magnetic implants.

MRCP Technique

MRCP technique is based on heavily T2-weighted pulse sequences which results in dramatic increase in contrast between stationary fluids (bile) and background (hepatic and pancreatic parenchyma, peritoneal fat). As a result, the bile appears at very high signal intensity whereas the background at low. In addition, no signal will come from flowing blood.

FSE sequence has been demonstrated very suitable for performing heavily T2-weighted studies in the abdomen. As a result, it has become the technique of choice for MRCP studies. Compared with GRE sequence, FSE has a higher SNR and CNR; a lower sensitivity to susceptibility artifacts, very common when studying the biliary tract (i.e., surgical clips, intestinal gas); a lower sensitivity to motion artifact and blood flow. Moreover, FSE takes advantage of new techniques to improve the image quality, such as gradient moment nulling, which reduces artifacts from periodic motion, respiratory triggering, and fat-suppression technique, in order to improve the

contrast between the bile ducts and the background. Typical pulse sequences and imaging parameters for MRCP are provided in Table 2.4.

Table 2.4 Typical Imaging Parameters for various MRCP Acquisitions [15]

	Localizer	SSFSE (HASTE)	SSFSE (HASTE)	MRCP (Thick slice)	FRFSE 3D	2D FSE
plane	3 plane	Coronal	Transverse	Oblique, multiple orientations	Coronal	Transverse
Mode		2D	2D	2D	3D	2D
Pulse Seq.		SSFSE	SSFSE	SSFSE	FRFSE	FSE
No. of echoes					1	31
TE		180	180	1s	500-600	150-250
TR		3000	3000	3000	4000	4000
Optional			Resp.trig.		Resp.trig	
Flip Angle		-	-	-	-	-
Saturation					Fat	Fat
FOV	40	32-40	32-40	28-38	32-40	32-40
Slice Thickness (mm)	8	4-5	4-5	40	1.6	3
Spacing (mm)	2	0	0	-	-	0.3
Matrix	256×128	384×224	384×224	320×320	256×256	384×256
NEX	1	0.5	0.5	1	1	2

2.2 Review of Related Literature

Larkman D.J, Cokkinos D., Hajnal J.V, et al [2], studied the feasibility of performing MRCP at 3.0 Tesla, and compared the image quality and signal characteristics of a sample of patients undergoing an examination on both 1.5 and 3.0 Tesla systems. A prospective pilot study was performed in which 10 patients underwent an MRCP examination consecutively on 1.5 and 3.0 Tesla systems (both Philips Intera). HASTE sequence and a coronal thick slab 2D turbo-spin echo (TSE) sequence were compared on both systems.

The results showed a slightly higher signal intensity ratio (CBD:liver) at 3.0 Tesla compared with 1.5 Tesla (8.1±1.9 vs 5.6±0.7, p=0.002). No significant difference was found between the SI ratios of (CBD:fat) on HASTE images or (CBD:liver) on TSE images. The qualitative analysis showed superior image quality of 3.0 Tesla over 1.5 Tesla images on both HASTE (31±5 vs 25±9, p=0.032), and TSE sequences (34±7 vs 28±4, p=0.043). This pilot study showed that MRCP is feasible at 3.0 Tesla with some improvement in image quality and signal characteristics.

Hiroyoshi I., Masako k., Yoji M., et al [3], evaluated the impact of MRCP imaging at 1.5T and 3.0T on image quality. Fourteen volunteers were examined at both 1.5T and 3.0T using MRCP imaging performed with a breath-held two-dimensional (2D) HASTE thick-slab sequence, a free-breathing navigator-triggered three-dimensional (3D) TSE sequence with prospective acquisition correction, and a heavily T2W sequence with breath-held multi-slice HASTE. All images were scored for visualization of the biliary and pancreatic ducts, severity of artifacts, image noise, and overall image quality

The results showed the MRCP imaging at 3.0T yielded a significant improvement in overall image quality compared to 1.5T. They found at 3D TSE a non significant trend toward superior visualization of cystic duct, CBD and pancreatic duct at 3.0T. At sequence heavily T2W imaging with thin sections (1.4 mm) at 3.0T provided diagnostic images and better visualization of the biliary and pancreatic ducts than heavily T2W imaging with standard sections (2.8 mm) at 3.0T.

Yasui M. et al [4], compared the image quality and visualization in MRCP by using different high-field strength 1.0 vs. 1.5 Tesla MR units and assessed the effect of field strength on MRCP. Ten healthy volunteers and 37 patients suspected of having pancreatobiliary diseases were studied with HASTE and rapid acquisition by relaxation enhancement (RARE) sequences.

The results showed SNR and CNR in HASTE sequences acquired with the 1.5 Tesla (T) unit were significantly higher than those acquired by the 1.0 T unit (p=0.001). In qualitative analysis, there were no statistical significantly differences in image quality or visualization of the ducts in either HASTE or RARE sequences between 1.0 T and 1.5 T.

Pavone P., Laghi A., et al [5], evaluated the feasibility of MRCP at 0.5 T. Thirty-one patient with dilated biliary systems were examined with three dimensional MRCP studied with a 0.5 T superconducting magnet. A three-dimensional TSE sequence was acquired (TR= 5,000 ms, TE= 244 ms, echo train length = 45). A coronal image was post processing with MIP algorithm.

The results showed optimized parameters (TR= 3000 ms, TE= 700 ms, echo train length = 128) which reduced acquisition time to 3 min when comparison with ERCP the MRCP could have the same clinical value as high field strength MRCP.

Irie H., et al [10], determined appropriate acquisition parameters for MRCP with RARE sequence and the optimal MRCP technique by comparing half-Fourier RARE, steady-state free precession (SSFP) of sequences 2D FSE and 3D FSE sequences. They used half-Fourier RARE MRCP images with varying parameters and compared by using a phantom. Duct conspicuity and CNRs were compared for the four MRCP techniques in phantom and healthy volunteers.

The results at 5 mm thick section without gap was appropriated for half-Fourier RARE MRCP. Only for half- Fourier RARE MRCP could depict a 1mm duct. CNR was the highest with half- Fourier RARE, followed by 3D fast spin echo, 2D fast spin echo and SSFP sequences. ROC curve analysis revealed no inter-observer differences, and the area under the curve for detection of strictures of the main pancreatic duct was as high as 0.89

CHAPTER III

RESEARCH METHODOLOGY

3.1 Research Hypothesis

The image quality obtained from MRI 3.0 Tesla is better than MRI 0.4Tesla (Open) on both phantom and MRCP imaging.

3.2 Research Design

This study is a comparative research.

3.3 Research Design Model

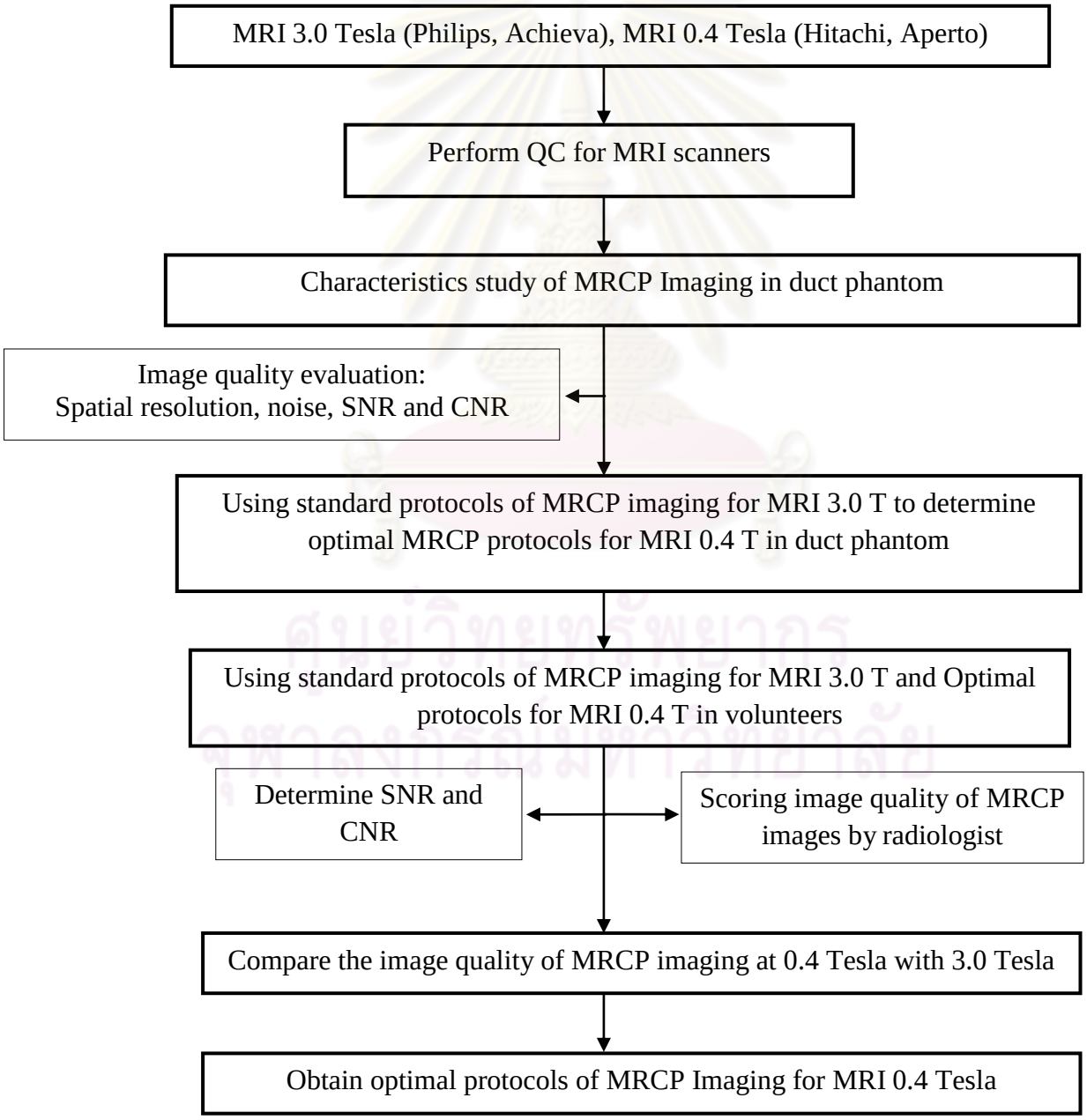

3.4 Conceptual Framework

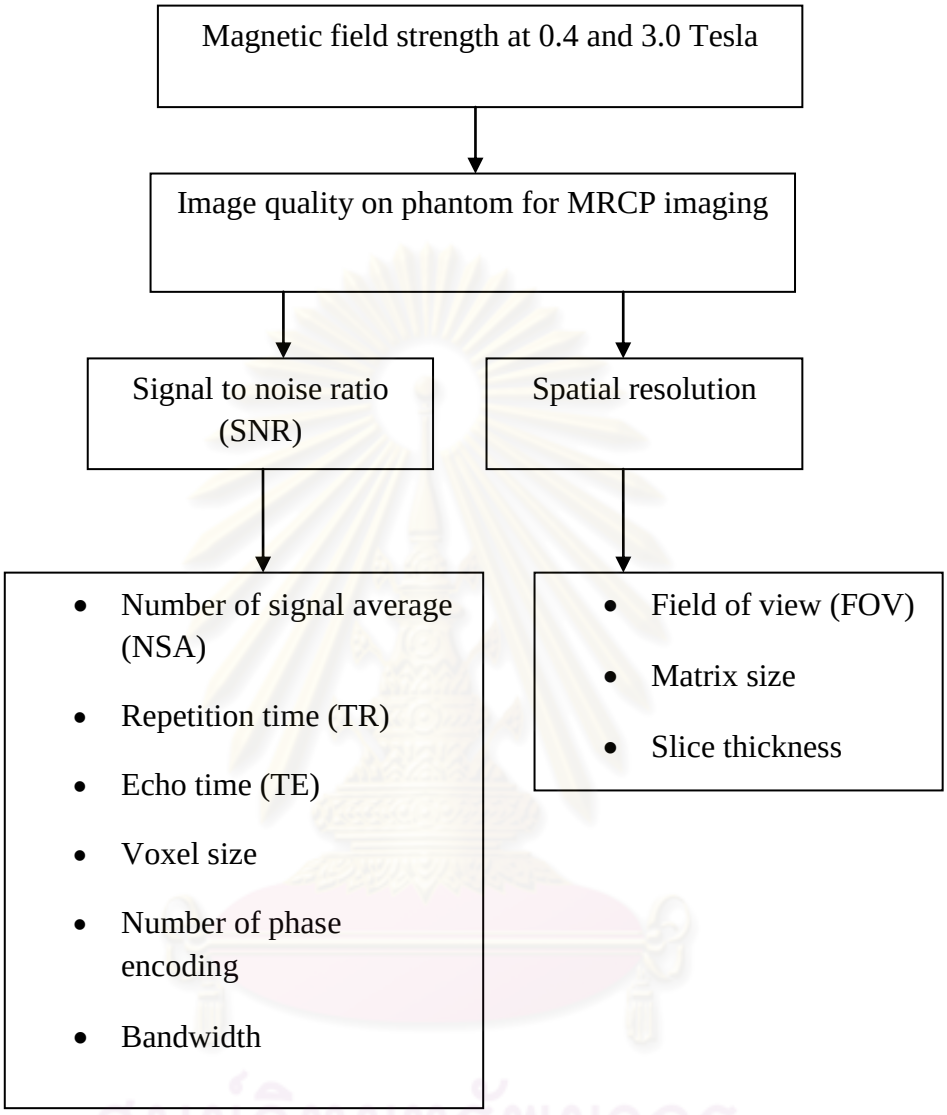

3.5 Research Questions

3.5.1 Primary Question

What are the optimal MRI protocols for MRCP imaging acquired by MRI 0.4 Tesla (Open) in comparison to MRI 3.0 Tesla?

3.5.2 Secondary Question

What are the image quality (spatial resolution and SNR) for MRI 0.4 Tesla (Open) and 3.0 Tesla in phantom study?

3.6 Materials

3.6.1 MRI equipments:

MRI 3.0 Tesla, Philips: Achieva TX

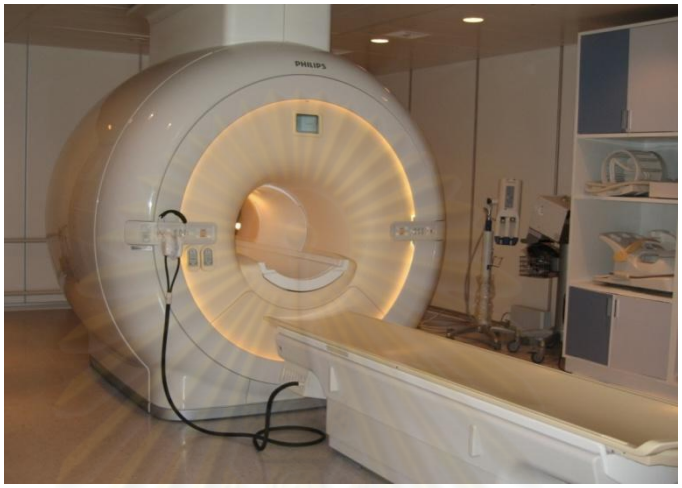

Figure 3.1 MRI 3.0 Tesla (Philips: Achieva TX, Netherland)

MRI 3.0 Tesla, manufacturer Philips model Achieva TX at Department of Radiology, King Chulalongkorn Memorial Hospital has been installed in 2010**.**

MRI 0.4 Tesla (Open), Hitachi: Aperto

Figure 3.2 MRI 0.4 Tesla (Open), (Hitachi: Aperto**,** Japan)

MRI 0.4 Tesla (Open), manufacturer Hitachi model Aperto has been installed in 2006 at Department of Radiology, Rajavithi Hospital. Type of magnet is permanent.

3.6.2 Coil Type

MRI 3.0 Tesla: 16 elements phased-array coil

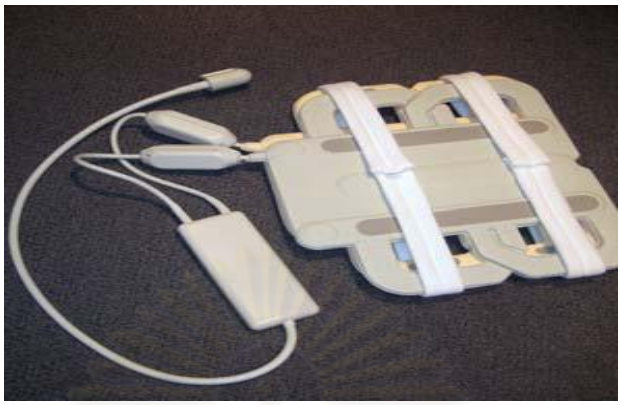

Figure 3.3 SENSE XL Torso coil

The SENSE XL Torso coil, receiver type, was designed as flexible volume coil of anterior and posterior sections. Each section consists of 16 elements: 8 upper and 8 lower elements. It can be performed in AP, RL, and HF directions, especially, mainly in AP and RL directions, generally use for the part of abdomen/pelvis, thorax/abdomen, or other two-station combinations as well as individual anatomies. The recommended field of view for single station coronal or sagittal examinations is 45 x 38 (HF) cm.

MRI 0.4 Tesla: Body phase array coil

Figure 3.4 Body phase array coil

A phase array coil, an MR receiver coil, consists of an array of individual receiver coils. A phase array yields the high signal to noise ratio seen with small surface coils while simultaneously providing a large field of view. In a phase array, adjacent coil is overlapped to eliminate mutual inductance in a measure of coupling between coils. This coupling would cause an unwanted degree of overlay required to set the mutual inductance to zero, determined by the geometry of the individual coils. Each coil in the phased array is connected to a low impedance amplifier. Use of low impedance amplifiers help reduce coupling between distant coils. The outputs of the preamplifiers in the array are sampled simultaneously and combined electronically.

A single receiver coil may consist of many individual coil “elements”. Parallel imaging techniques depend on the use of multi element array coils. Differences in spatial sensitivities of each element are exploited in paralleled imaging to deliver scan time saving.

3.6.3 Magphan phantom

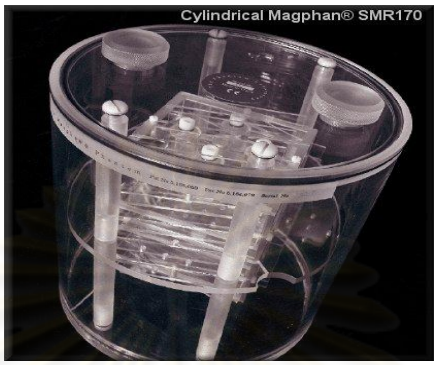

Figure 3.5 Magphan phantom

Cylindrical Magphan SMR 170 as in figure 3.5 was used to study the image quality characteristics of spatial resolution and signal to noise ratio for both MRI equipments. The phantom is filled up by copper sulfate solution at different concentration of 1 gram of copper sulfate to 1 liter of distilled water. 0.220, 0.295, 0.430 and 0.590 grams of copper sulfate per liter of distilled water were filled in four contrast containers. The procedures were conducted as in the Magphan manual and AAPM report No.28 and 34.

3.6.4 Duct phantom

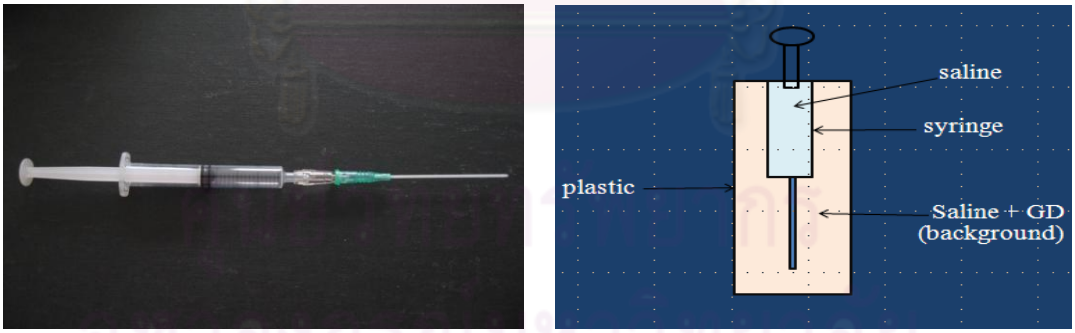

(a) (b)

Figure 3.6 (a) Syringe and plastic needle as duct phantom, (b) duct phantom placed inside plastic bottle.

There are two parts of duct phantom; the first is made of plastic needle with internal diameter of 2.0 mm (simulated as pancreatic duct). The second is 3 cc plastic syringe with diameter of 10 mm (simulated to express the signal intensity in common bile duct). Both syringe and plastic needle are placed inside a plastic bottle containing saline [10] whereas outside of a duct model was filled with saline mixed Gadolinium.

This phantom was used to determine the 0.4 T MRI optimal parameters affecting the image quality (spatial resolution, SNR and CNR) in MRCP imaging.

3.6.5 Image J program

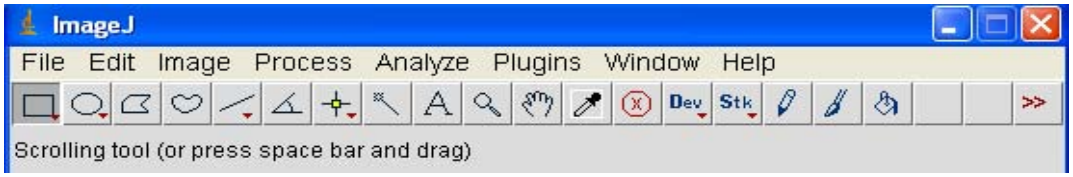

Figure 3.7 Image J program

Image J is a public domain Java image processing program inspired by National Institute of Health (NIH) Image for the Macintosh. It runs, either as an online applet or as a downloadable application, on any computer with a Java 1.4 or later virtual machine. Downloadable distributions are available for windows, Mac OS, Mac OS X and Linux. This program can display, edit, analyze, process, save and print 8-bit and 32 bit images. It can read many image formats including TIFF, GIF, JPEG, BMP, DICOM, FITS and "raw". The calculation of area and pixel value statistics of user-defined selections are available as well as measuring of distances and angles. It can create density histograms and line profile plot and also supports standard image processing functions such as contrast manipulation, sharpening, smoothing, edge detection and median filtering [10].

Image J program collaborated with the Microsoft office 2007 was used for the calculation of full width at half maximum (FWHM) and measured the signal intensity or pixel value of common bile duct and liver.

3.6.6 SPSS program

SPSS (originally, Statistical Package for the Social Sciences) is a computer program used for statistical analysis. SPSS is among the most widely used programs for statistical analysis in social science. It is used by market researchers, health researchers, survey companies, government, education researchers, marketing organizations and others. The original SPSS manual (Nie, Bent & Hull, 1970) has been described as one of "sociology's most influential books". In addition to statistical analysis, data management (case selection, file reshaping, creating derived data) and data documentation (a metadata dictionary is stored in the data file) are features of the base software. Statistics included in the base software [18]:

- Descriptive statistics: Cross tabulation, Frequencies, Descriptive, Explore, Descriptive Ratio Statistics
- Bivariate statistics: Means, t-test, ANOVA, Correlation (bivariate, partial, distances), Nonparametric tests
- Prediction for numerical outcomes: Linear regression
- Prediction for identifying groups: Factor analysis, cluster analysis (two-step, K-means, hierarchical), Discriminant

SPSS program was used to calculate the intra-class correlation coefficients (ICC) for assessment consistency with effects due to reading 7 ducts structure by radiologist.

The **intra-class correlation** [19], (ICC) is a descriptive statistic that can be used when qualitative measurements are made on units that are organized into groups. It describes how strongly units in the same group resemble each other. While it is viewed as a type of correlation, unlike most other correlation measures it operates on data structured as groups, rather than data structured as paired observations.

The intra-class correlation is commonly used to quantify the degree to which individuals with a fixed degree of relatedness (e.g. full siblings) resemble each other in terms of a qualitative trait. Another prominent application is the assessment of consistency or reproducibility of qualitative measurements made by different observers measuring the same quantity.

The ICC is constructed to be applied to exchangeable measurements that is, grouped data in which there is no meaningful way to order the measurements within a group. In assessing conformity among observers, if the same observers rate each element being studied, then systematic differences among observers are likely to exist, which conflicts with the notion of exchangeability. If the ICC is used in a situation where systematic differences exist, the result is a composite measure of intra-observer and inter-observer variability. Since the intra-class correlation coefficient gives a composite of intra-observer and inter-observer variability when used with data where the observers are not exchangeable, its results are sometimes considered difficult to interpret in that setting. Alternative measures such as Cohen's kappa statistic, the Fleiss kappa, and the concordance correlation coefficient have been proposed as more suitable measures of agreement among non-exchangeable observers.

3.7 Methods

3.7.1 MRI image quality characteristics study

The image quality characteristics of MRI 3.0 T, and MRI 0.4 T were studied following the Magphan manual (2001) [14] and AAPM report No.28 (1989) [12] and 34(1991) [13]. The specific image parameters are: sensitometry, slice thickness and slice position/separation.

3.7.2 The characteristics of MRCP imaging in duct phantom

The characteristics of MRCP imaging are spatial resolution, image noise, signal to noise ratio and contrast to noise ratio. A duct phantom with internal diameter 2.0 mm of a plastic needle and 10 mm diameter of syringe were scanned by both MRI equipments.

MRI 3.0 T techniques:

- The duct phantom was placed at the center of the 16 elements phased-array coil (Figure 3.8a).
- The coronal 2D SSh-MRCP rad TSE and 3D high resolution SENSE T2W FSE were obtained from the standard parameters as shown in Table 3.1.

Table 3.1 The standard parameters of MRCP protocols at MRI 3.0 T (standard protocol).

	TR (ms)	TE (ms)	FA	FOV (mm)	Thickness (mm)/gap	Freq.	phase	NSA	Recon matrix	time
2D	5,640	740	90	300	40/0	256	256	1	256	5 s
3D	2,340	740	90	300	2/0	255	256	1	512	3.39 min

FA: Flip angle, Freq: frequency, Recon: reconstruction, SSh: single shot, rad: radial, TSE: Turbo spin echo.

- The FWHM was measured by image J program for visualization of the duct in coronal 2D and 3D image of phantom.
- The coronal image at syringe diameter 10 mm. was evaluated to obtain the SNR and CNR by placing ROI at the center of syringe (signal) and outside syringe (noise). The signal intensity was used to calculate SNR, CNR and image noise.

MRI 0.4 T techniques:

The procedure and the analysis were performed the same as at MRI 3.0 T but the scan parameters were different.

- The duct phantom was placed at the center of the body phased-array coil (Figure 3.8b).
- The coronal 2D FSE and coronal 3D heavily T2W FSE were obtained as shown in Table 3.2.

Table 3.2 The parameters of MRCP protocols at MRI 0.4 T (original protocol).

	TR (ms)	TE (ms)	FA	FOV (mm)	Thickness (mm)/gap	Freq.	phase	NSA	Recon. matrix	time
2D	4,000	512	90	300	40/0	256	256	2	256	8 s
3D	4,000	540	90	300	2/0	256	256	4	512	5.20 min

- The FWHM was measured by image J program for visualization the duct in coronal 2D and 3D image of phantom.
- The coronal image at syringe diameter 10 mm. was evaluated to obtain the SNR and CNR by placing ROI at the center of syringe and outside syringe (noise).
- The signal intensity (SI) was used to calculate SNR, CNR and image noise (standard deviation of background surrounding syringe) of saline+ Gadolinium by equations as follow:

$$SNR = \frac{SI\ (saline\ in\ syringe)}{SD\ (saline + Gadolinium)} \quad (6)$$

$$CNR = \frac{SI\ (saline\ in\ syringe) - SI\ (saline + Gadolinium)}{SD\ (saline + Gadolinium)} \quad (7)$$

$$Noise = SD\ (saline + Gadolinium) \quad (8)$$

3.7.3 Using standard protocols of MRCP imaging for MRI 3.0 T to determine optimal MRCP protocols for MRI 0.4 T in duct phantom

The duct phantom was used to study the optimal MRI parameters for MRCP (SNR, CNR and Spatial resolution) for 0.4 T and compare with at 3.0 T for standard MRCP protocol.

Standard MRCP imaging protocols of MRI 3.0T

- The duct phantom was placed at the center of the 16 elements phased-array coil (Figure 3.8a).
- The coronal 2D SSh-MRCP rad TSE: TR= 5,640 ms, TE= 740 ms, FOV= 300 mm, thickness = 40 mm, no inter-slice gap, image matrix size was 256×256, NSA= 1 and acquisition time = 5 s and 3D high resolution SENSE T2W FSE : TR= 2,340 ms, TE= 740, FOV= 300 mm, thickness = 2.0 mm, no inter-slice gap, matrix size was 255×256, NSA= 1, and acquisition time = 3.39 min
- 3D reconstruction image by maximum intensity projection (MIP).

Optimal MRCP imaging protocol of MRI 0.4 T

- The duct phantom was placed at the center of the body phased-array coil (Figure 3.8b).

- The coronal 2D and 3D Heavy T2-weighted FSE (Fast Spin Echo) was obtained by varying the parameters affecting for image quality (SNR and Spatial resolution).

- The FWHM was measured by image J program to evaluate the spatial resolution at duct phantom diameter 2.0 mm.

- The signal intensity (SI) was used to calculate SNR, CNR and image noise (standard deviation of background surrounding syringe) of saline+ Gadolinium at syringe diameter 10 mm.
- Compare the image quality for both field strengths and obtain the optimal parameters of MRCP imaging at MRI 0.4 T.

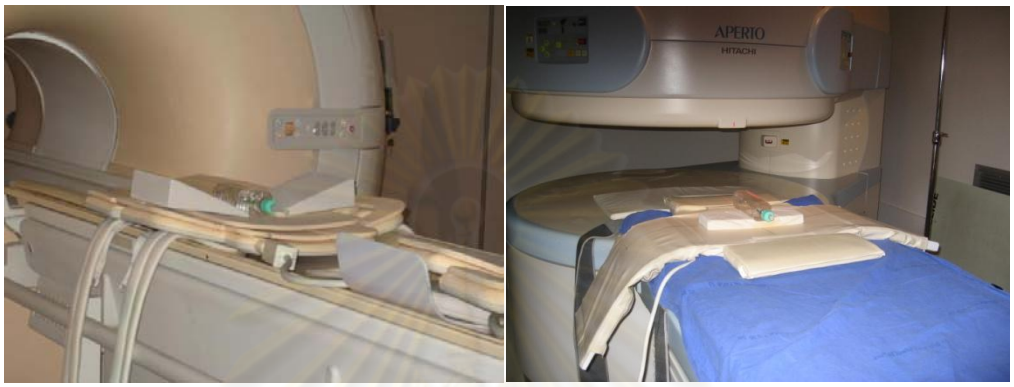

(a) (b)

Figure 3.8 The experimental set up of duct phantom for evaluation of spatial resolution, SNR and CNR at MRI 3.0 T (a) and 0.4 T (b).

3.7.4 MRCP protocols in volunteers.

The standard MRCP imaging protocols for MRI 3.0 T and the obtained optimal protocols in phantom of MRCP imaging for MRI 0.4 T were used to acquire in volunteers.

3.7.5 Quantitative assessment

Quantitative assessment was determined as the SNR and CNR by placing circular ROI on common bile duct (CBD) and liver. The standard deviation (SD) of the signal intensity at the liver is determined as the noise (SD_{noise}). The equations are:

$$SNR = \frac{SI\ (common\ bile\ duct)}{SD\ (Liver)} \quad (9)$$

$$CNR = \frac{SI\ (common\ bile\ duct) - SI\ (Liver)}{SD\ (Liver)} \quad (10)$$

$$Noise = SD\ (Liver) \quad (11)$$

The mean and standard deviation of pixel value were used to evaluate the quantitative assessment for both field strengths.

3.7.6 Qualitative assessment

One radiologist with over 10 year experience evaluated these images for qualitative appearance. Seven structures were analyzed: gall bladder, left hepatic duct, right hepatic duct, cystic duct, common hepatic duct, common bile duct and pancreatic duct. Five-point scales were scored to assess the image quality.

3.7.7 Comparison of the SNR and CNR and the scoring of image quality for both field strengths.

The purpose of this study is to determine and optimize the MRCP protocol of MRI 0.4 T. However, the diagnostic requirement for MRCP imaging is not only high spatial resolution but also the contrast resolution and the appropriate acquisition time. Therefore, the protocols setting for MRCP imaging can be obtained by comparing the results of characteristic of spatial resolution, SNR and CNR including the total examination time.

3.8 Data analysis

3.8.1 Image Evaluation

This research is a prospective study which healthy volunteers were invited to the MRCP examination at 3.0 T and 0.4 T.

3.8.2 Image quality scores (Qualitative image analysis)

A reader with over 10 years of MRI experience performed a blinded qualitative analysis of randomized images review on a View Forum workstation. Each pair of MR sequences were evaluated together for the quality of visualization of individual structures of the pancreatobiliary system according to predefined criteria. Seven structures were: the gall bladder, left hepatic duct, right hepatic duct, common hepatic duct, common bile duct, cystic duct and pancreatic duct. There are five-point scales scored by radiologist:

4= very good (diagnostic image quality, visualize structures with homogeneous of ducts)
3= good (still diagnostic, visualize structures with inhomogeneous of ducts)
2= moderate (partly diagnostic)
1= poor (barely diagnostic)
0= non diagnostic (lacking enhancement of the ducts)

The consistency of image quality is obtained by score with two readings. The measurement was assessed by calculating intra-class correlation coefficients (ICC) for 7 structures of ducts.

3.8.3 Signal and Contrast to noise ratio (Quantitative image analysis).

The quantitative image quality is analyzed by create a 28.8 mm^2 circular region of interest at the center of the common bile duct and liver parenchyma. The mean pixel values in these regions of interest were used to calculate the signal intensity. The standard deviation (SD) of the liver represented as the noise (SD noise). A single ROI was located in a homogenous portion of the liver and set in an area to avoid vessels and prominent artifacts. To minimize coil in-homogeneity errors, a

small ROI for signal measurement of the common bile duct was set at center of the common bile duct. The equation (9), (10) and (11) were used to calculate SNR and CNR respectively.

3.9 Sample size determination

The sample size between two related groups was calculated as the difference of the image quality from both field strength MRI scanners as following:

Two related groups so, n pair $\frac{(Z\alpha+Z\beta)^2\sigma^2}{d^2}$ where $\sigma^2 = \sigma^2_1+\sigma^2_2 - 2\gamma\sigma_1\sigma_2$

$\alpha = 0.05$, $\beta = 0.10$, $Z_\alpha = Z0.05 = 1.645$ (one tail) ,$Z_\beta = Z0.10 = 1.28$

σ^2 = Variance of difference = 2.77, d = Difference = 2.50 ,$\gamma = 0.5$,$\sigma_1 = 1.9$,$\sigma_2 = 0.7$

Therefore, n pair = $\frac{(1.645+1.28)^2(2.77)}{(2.5)^2}$ = 3.81, 10 cases will be collected.

From the literature review [1] the signal intensity ratio (CBD: liver) at 3.0 Tesla and 1.5 Tesla were (8.1±1.9 vs 5.6±0.7). To obtain the maximum sample size the correlation coefficient, γ is defined as 0.5.

3.10 Statistical analysis

SNR and CNR were calculated by equation (9) and (10). The Image J program was used to measure the signal intensity and the image quality score were expressed as mean and the standard deviation. Statistical comparisons of mean values were performed with the t-test for paired samples. The qualitative image analysis was compared using the t-test for paired samples. Statistical significance is assumed at p=0.05 and use 95% confidence interval (CI) in all cases. Microsoft excels and SPSS program were used to calculate all data value.

3.11 Outcome measurement

Variables

Phantom study

Independent variables: Slice thickness, NSA, FOV, Matrix size, TR, TE, Flip angle, bandwidth and number of phase encoding.

Dependent variables: Spatial resolution, Signal to noise ratio, contrast to noise ratio

Patient study

Independent variables: signal intensity in biliary system and MIP on MRCP imaging

Dependent variables: Preference score, Signal to noise ratio and contrast to noise ratio

3.12 Expected benefits

The MRI parameters for better image quality at both field strengths and optimized protocol of MRCP imaging at MRI 0.4 Tesla (Open) are expected. The improvement in image quality of MRCP imaging could increase the diagnostic confidence level for radiologist in diagnosis of MRCP examination especially for MRI 0.4 Tesla. In addition, the quality control of MRI systems would improve the spatial resolution and SNR for both field strengths using phantom study.

3.13 Ethical consideration

Most parts were performed in phantom to investigate the physical characteristics of spatial resolution and SNR. The clinical image quality was performed in healthy volunteers in order to achieve the optimized protocols. The ethical had been approved by the Ethics Committee, Faculty of Medicine, Chulalongkorn University and Rajavithi hospital.

CHAPTER IV

RESULTS

4.1 The performance test of MRI scanners

The performance test of MRI 3.0 T and MRI 0.4 T were image uniformity, sensitometry, high contrast resolution, low contrast sensitivity, slice geometry, geometric distortion and slice separation. The result of quality control of MRI scanners is shown in Appendix B. The report of both field strengths MRI systems is shown in Table 4.1 and 4.2.

Table 4.1 REPORT OF MRI SYSTEM 0.4 T PERFORMANCE TEST

LOCATION	Sirinthorn Building, Floor 1 Rajavithi Hospital
DATE	July 28, 2010
MANUFACTURER	HITACHI
MODEL	APERTO
Image Uniformity	pass
Sensitometry (MRI Number)	pass
High Contrast Resolution	pass
Low Contrast Sensitivity	pass
Slice Geometry (Slice Width)	pass
Geometric Distortion	pass
Slice Position/Separation	pass

Table 4.2 REPORT OF MRI SYSTEM 3.0 T PERFORMANCE TEST

LOCATION	Apuntreepacha Building, Floor 1 King Chulalongkorn Memorial Hospital
DATE	August 7, 2010
MANUFACTURER	PHILIPS
MODEL	ACHIEVA TX
Image Uniformity	pass
Sensitometry (MRI Number)	pass
High Contrast Resolution	pass
Low Contrast Sensitivity	pass
Slice Geometry (Slice Width)	pass
Geometric Distortion	pass
Slice Position/Separation	pass

4.2 Characteristics of MRCP imaging in duct phantom

4.2.1 Evaluation of the spatial resolution by FWHM

A. Variation of slice thickness

The coronal plane of duct phantom diameter 2.0 mm for 2D images is displayed for the study of the spatial resolution affected by the slice thickness (thick-slab) of 20, 30, 40, 50 and 60 mm and 3D images at the slice thickness of 2, 3, 4 and 5 mm at MRI 0.4 T. The chart of FWHM is shown as in Figure 4.1(a) for 2D and 4.1(b) for 3D.

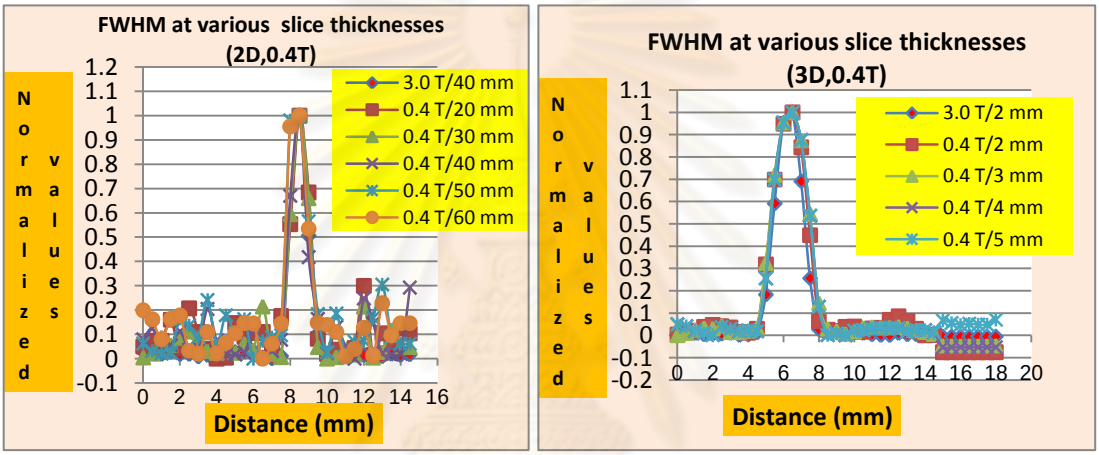

(a) **(b)**

Figure 4.1 The FWHM versus slice thickness of (a) 2D and (b) 3D images at MRI 0.4 T compared to 40 mm at 2D and 2.0 mm at 3D slice thickness of 3.0 T MRI system

Figure 4.1 shows the FWHM at a half of normalized values (0.5) of 2D and 3D images from each varying thickness at MRI 0.4 T. The FWHM at 2D images and 3D images is shown in the Table 4.3.

Table 4.3 FWHM as a factor of slice thickness of 2D and 3D images at MRI 0.4 T compared to 40 and 2 mm slice thickness of MRI 3.0 T respectively

2D / 0.4 T	**FWHM** (mm)	**3D /0.4 T**	**FWHM** (mm)
Thickness (mm)		Thickness (mm)	
20	2.6	2	2.8
30	2.6	3	2.8
40	2.8	4	2.9
50	2.9	5	2.9
60	2.9		
40 mm at MRI 3.0 T	2.1	2 mm at MRI 3.0 T	2.3

From the Table 4.3, the shortest FWHM (2.6 mm) was obtained at 20 and 30 mm thickness for 2D images and at 2 and 3 mm thickness (2.8 mm) for 3D images respectively. The thinnest slice thickness, the best spatial resolution is obtained.

B. Variation of field of view (FOV)

The coronal plane from duct phantom diameter 2.0 mm 2D and 3D images with variation of FOV at 280, 300, 320, 340 mm for MRI 0.4 T to evaluate the spatial resolution, FWHM are displayed in Figure 4.2.

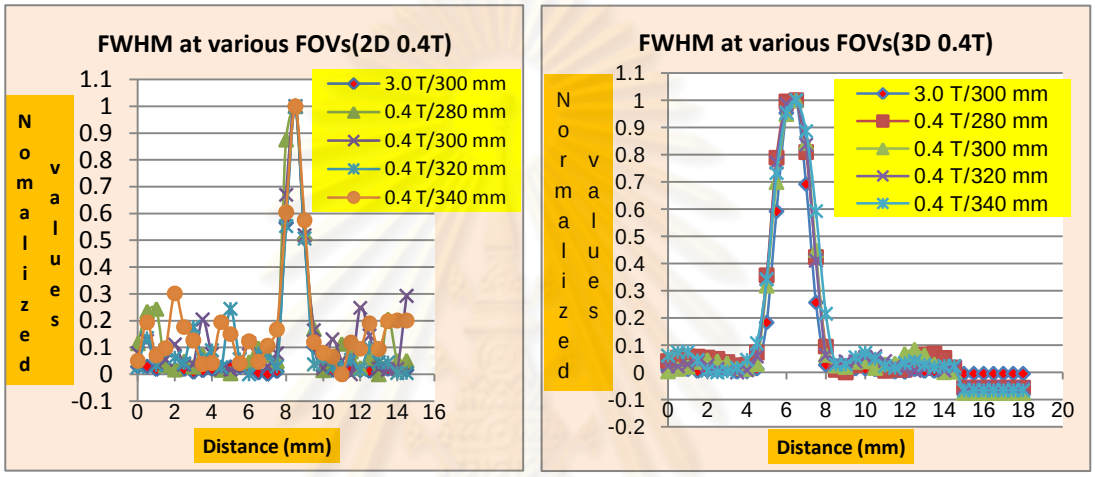

(a) **(b)**

Figure 4.2 FWHM at various FOVs of 2D (a) and 3D (b) images at MRI 0.4 T compared to FOV 300 mm at MRI 3.0 T

Figure 4.2 shows FWHM of 2D and 3D images at various FOVs at MRI 0.4 T. The FWHM values are shown in the Table 4.4.

Table 4.4 The FWHM values from variation of FOV 2D and 3D images at MRI 0.4 T compared to 300 mm FOV at MRI 3.0 T

2D / 0.4 T	**FWHM** (mm)	**3D /0.4 T**	**FWHM** (mm)
FOV(mm)		FOV(mm)	
280	2.1	280	3.0
300	2.5	300	2.9
320	3.2	320	3.0
340	3.2	340	3.1
300 mm at MRI 3.0 T	2.1	300 mm at MRI 3.0 T	2.3

From the Table 4.4, the shortest FWHM (2.1 mm) for 2D images at 0.4 T was found at 280 mm FOV and at 300 mm FOV (2.9 mm) for 3D images respectively.

C. Variation of number of phase encoding (matrix)

The coronal plane from duct phantom diameter 2.0 mm 2D and 3D images in phase direction are displayed to evaluate the spatial resolution at 192, 256 , 288, 320 at MRI 0.4 T as shown in Figure 4.3.

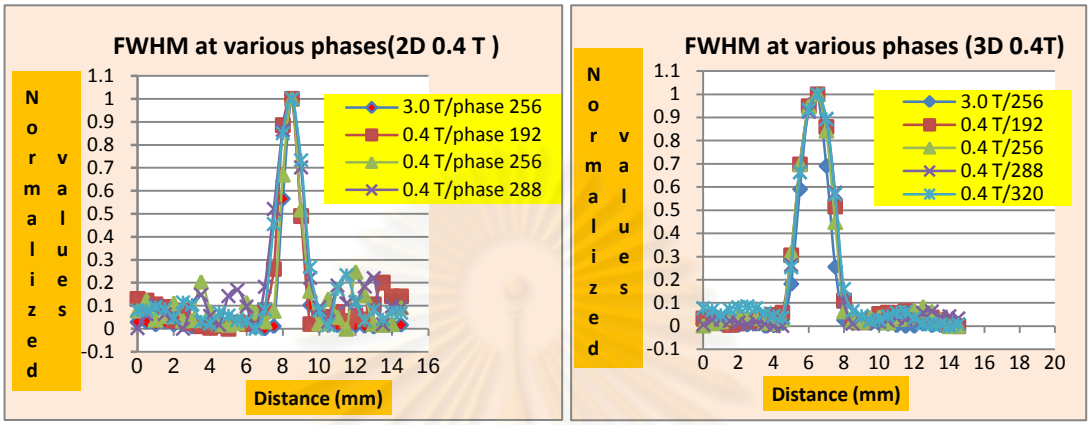

(a) **(b)**

Figure 4.3 FWHM versus phase of 2D (a) and 3D (b) images at MRI 0.4 T compared to number of phase 256 at MRI 3.0 T

Figure 4.3 shows the FWHM of 2D and 3D images from various number of phases at MRI 0.4 T with MRI 3.0 T. The FWHM values from various numbers of phases are shown in the Table 4.5.

Table 4.5 The FWHM from variation number of phase 2D and 3D images at MRI 0.4 T compared to number of phase 256 at MRI 3.0 T

2D / 0.4 T Number of phase	**FWHM** (mm)	**3D /0.4 T** Number of phase	**FWHM** (mm)
192	3.2	192	3.1
256	2.5	256	3.0
288	2.4	288	2.9
320	2.4	320	3.0
256 at MRI 3.0 T	2.1	255 at MRI 3.0 T	2.3

From the Table 4.5, the shortest FWHM (2.4 mm) of phase for 2D images at 0.4 T is at number 288 and 320 and 3D images (2.9 mm) at number 288

4.2.2 Evaluation of the signal to noise ratio (SNR), contrast to noise ratio (CNR) and image noise for MRCP imaging using syringe.

The image noise, SNR and CNR for MRCP imaging are evaluated with the variation of scanning parameters, the method for estimating the value of coronal MRCP images are obtained by using the part of syringe diameter 10 mm for duct phantom. The coronal 2D and 3D images were reconstructed.

B. Variation of slice thickness

The 2D coronal plane images in part of syringe from duct phantom diameter 10 mm are obtained from the variation of slice thickness at 20, 30, 40, 50 and 60 mm. and 3D image at 2 , 3, 4 and 5 mm for MRI 0.4 T to evaluate the SNR, CNR and noise. The signal intensity values by drawing ROI were measured, the SNR, CNR and image noise were compared to MRI 3.0 T as in the Table 4.6 and 4.7 respectively.

Table 4.6 The image noise, SNR and CNR at various slice thickness for 2D images at 0.4 T compared to MRI 3.0 T

Thickness (mm)	**syringe**		**Bkg**		**SNR**	**CNR**
	mean	**SD**	**mean**	**SD** (Noise)	**SI** (syr) / **SD** (bkg)	**SI** (syr)-**SI** (bkg) / **SD** (bkg)
20	**15976.8**	**1218.1**	**411**	**175.2**	**91.18**	**88.84**
30	**15700.4**	**1196.3**	**333.3**	**156.7**	**100.14**	**98.02**
40	**15824**	**1158.5**	**310**	**108.4**	**146.03**	**143.17**
50	**14823.7**	**1077.2**	**287.8**	**90.7**	**163.45**	**160.28**
60	**15839.1**	**1115.1**	**347.3**	**101.7**	**155.74**	**152.32**
3.0 T (40 mm)	**483.42**	**52.49**	**6.30**	**2.85**	**169.62**	**167.41**

*****syr (syringe)

Table 4.7 The image noise, SNR and CNR at various thicknesses of 3D images at 0.4 T compared to MRI 3.0 T

Thickness (mm.)	**syringe**		**Bkg**		**SNR**	**CNR**
	mean	**SD**	**mean**	**SD** (Noise)	**SI** (syr) / **SD** (bkg)	**SI** (syr)-**SI** (bkg) / **SD** (bkg)
2	**15379.9**	**744.9**	**449.1**	**59.6**	**258.05**	**250.51**
3	**14439.5**	**1887.5**	**349.8**	**55.26**	**261.30**	**254.97**
4	**16707.6**	**563.6**	**380.1**	**47.37**	**352.70**	**344.68**
5	**16627.3**	**451.5**	**309.1**	**45.22**	**367.69**	**360.86**
3.0 T (2 mm)	**1187.91**	**119.39**	**4.13**	**2.19**	**542.42**	**540.53**

The minimum thickness was 2 mm at MRI 0.4 T

Table 4.6 shows the SNR and CNR for 2D MRCP imaging. SNR and CNR are highest (163.45, 160.28) at the largest thickness 50 mm. For 3D images in table 4.7 the slice thickness at 5 mm showed a highest SNR and CNR (367.69 and 360.86). The

lowest noise is at slice thickness 50 mm (90.7) for 2D images and 5 mm (45.22) for 3D images.

B. Variation of field of view (FOV)

The 2D and 3D coronal plane images in the part of syringe from duct phantom diameter 10 mm are obtained from variation of FOV at 260, 280, 300, 320 and 340 mm at MRI 0.4 T. The signal intensity value by drawing ROI to measure image noise, SNR and CNR are compared to MRI 3.0 T as in the Table 4.8 and 4.9 respectively

Table 4.8 The image noise, SNR and CNR at various FOV for 2D images at 0.4 T compared to MRI 3.0 T

FOV (mm)	**syringe**		**Bkg**		**SNR**	**CNR**
	mean	**SD**	**mean**	**SD** (Noise)	**SI** (syr) / **SD** (bkg)	**SI** (syr)-**SI** (bkg) / **SD** (bkg)
280	**24746.7**	**1698.5**	**772**	**215.9**	**96.37**	**93.28**
300	**15404.9**	**1091.3**	**312.2**	**150.2**	**102.53**	**100.48**
320	**15947.5**	**1237.9**	**333.3**	**140.6**	**113.42**	**111.05**
340	**18128.3**	**1825.3**	**410.2**	**172.3**	**105.2**	**102.83**
3.0 T (300)	**483.42**	**52.49**	**6.30**	**2.85**	**169.62**	**167.41**

Table 4.9 The image noise, SNR and CNR with various FOV for 3D images at 0.4 T

FOV (mm.)	**syringe**		**Bkg**		**SNR**	**CNR**
	mean	**SD**	**mean**	**SD** (Noise)	**SI** (syr) / **SD** (bkg)	**SI** (syr)-**SI** (bkg) / **SD** (bkg)
280	**10089.8**	**164.9**	**337.8**	**67.1**	**150.37**	**145.33**
300	**17419.43**	**374.6**	**401.5**	**85.2**	**204.47**	**199.76**
320	**13522.1**	**328.4**	**344.8**	**56.6**	**239.08**	**232.97**
340	**14941.4**	**236.7**	**346.9**	**91.6**	**163.17**	**159.38**
3.0 T (300)	**1187.91**	**119.39**	**4.13**	**2.19**	**542.42**	**540.53**

Table 4.8 shows the SNR and CNR for 2D MRCP imaging. SNR and CNR are highest (113.42, 111.05) at FOV 320 mm. For 3D images in table 4.9 the FOV at 320 mm showed a highest value for both SNR and CNR (239.08 and 232.83). The lowest noise showed at FOV 320 mm (140.6) for 2D images and 320 mm also (56.6) for 3D images.

C. Variation of number of phase encoding (matrix)

The 2D and 3D coronal plane images in part of syringe from duct phantom diameter 10 mm are obtained from the variation number of phase steps at 192, 256, 288 and 320 for MRI 0.4 T to evaluate the SNR, CNR and noise. The signal intensity values by drawing ROI to measure SNR, CNR and image noise are compared to MRI 3.0 T as in the Table 4.10 and 4.11 respectively.

Table 4.10 The image noise, SNR and CNR with various number of phase for 2D images at 0.4 T compared to MRI 3.0 T

Phase	syringe		Bkg		SNR	CNR
	mean	SD	mean	SD (Noise)	SI (syr) / SD (bkg)	SI (syr)-SI (bkg) / SD (bkg)
192	16023.1	1094.7	380.1	177.5	90.27	88.13
256	14539.1	1064.5	403.1	169.1	85.99	83.61
288	14719.1	440.1	298.8	137.3	107.20	105.02
320	14704.1	759.8	390.4	150.9	97.44	94.85
3.0 T (256)	483.42	52.49	6.30	2.85	169.62	167.41

Table 4.11 The image noise, SNR and CNR with various number of phase for 3D images at 0.4 T compared to MRI 3.0 T

Phase	syringe		Bkg		SNR	CNR
	mean	SD	mean	SD (Noise)	SI (syr) / SD (bkg)	SI (syr)-SI(bkg) / SD (bkg)
192	13754.8	45.3	459.3	54.8	250.90	242.53
256	17419.43	374.6	401.5	85.2	204.47	199.76
288	9025.1	824.9	326.3	27.83	324.29	312.56
320	9026.5	736.0	303.9	51.34	175.81	169.89
3.0 T (256)	1187.91	119.39	4.13	2.19	542.42	540.53

Table 4.10 shows the SNR and CNR for 2D MRCP imaging. SNR and CNR are highest (107.20, 105.02) at number of phase 288. For 3D images in table 4.11 the number of phase at 288 shows a highest SNR and CNR (324.29 and 312.56). The lowest noise is at number of phase 288 (137.3) for 2D images and 288 also (27.83) for 3D images.

D. Variation of repetition time (TR)

The 2D and 3D coronal image plane in part of syringe from duct phantom diameter 10 mm are obtained from various TR at 2000, 3000 , 4000, 5,000 and 6000 ms for MRI 0.4 T to evaluate the SNR, CNR and image noise. The signal intensity values by drawing ROI to measure SNR, CNR and image noise are compared to MRI 3.0 T as in the Table 4.12 and 4.13 respectively.

Table 4.12 The image noise, SNR and CNR with various TR for 2D images at 0.4 T compared to MRI 3.0 T

TR (ms)	**syringe**		**Bkg**		**SNR**	**CNR**
	mean	**SD**	**mean**	**SD** (Noise)	**SI** (syr) / **SD** (bkg)	**SI** (syr)-**SI** (bkg) / **SD** (bkg)
2,000	**20650.2**	**1429.1**	**804**	**376.3**	**54.87**	**52.74**
3,000	**20107.2**	**1951.7**	**750.1**	**269.9**	**74.49**	**71.72**
4,000	**14233.1**	**1090**	**399.7**	**183.5**	**77.56**	**75.83**
5,000	**15047.1**	**1202.4**	**348.9**	**143.1**	**105.15**	**102.7**
6,000	**17118.2**	**1235.9**	**381.5**	**135.4**	**126.42**	**123.61**
3.0 T (5,640)	**483.42**	**52.49**	**6.30**	**2.85**	**169.62**	**167.41**

*****Scan time (s), TR 2,000 (4), 3,000 (6), 4,000 (8), 5,000 (10), 6,000(12)

Table 4.12 shows the SNR and CNR for 2D MRCP imaging. SNR and CNR are highest (126.42, 123.61) at TR 6,000 ms, For 3D images in table 4.13 the TR at 6,000 ms shows a highest value for both SNR and CNR (372.9 and 365.19). The lowest noise shows at TR 6,000 ms (135.4) for 2D images and 6,000 ms also (38.5) for 3D images.

Table 4.13 The image noise, SNR and CNR with various TR for 3D images at 0.4 T compared to MRI 3.0 T

TR (ms)	syringe		Bkg		SNR	CNR
	mean	SD	mean	SD (Noise)	SI (syringe) / SD (bkg)	SI (syr)-SI (bkg) / SD (bkg)
2,000	10392.6	301.6	668.9	133.9	77.63	72.64
3,000	19308.6	442.6	700.5	116.1	166.24	160.20
4,000	17230.3	319.87	562.95	64.44	267.38	258.64
5,000	13788.6	196.2	317	49.3	279.46	273.03
6,000	14349.2	277.9	296.8	38.5	372.9	365.19
3.0 T (2,340)	1187.91	119.39	4.13	2.19	542.42	540.53

*****Scan time (min), TR 2,000 (2.4), 3,000 (4), 4,000 (5.2), 5,000 (6.4), 6,000(8)

E. Variation of number of signal average (NSA)

The 2D and 3D coronal plane images in part of syringe from duct phantom diameter 10 mm are obtained from variation of NSA at 1, 2, 3 and 4 for MRI 0.4 T to evaluate the SNR, CNR and image noise. The signal intensity values by drawing ROI to measure SNR, CNR and image noise are compared to MRI 3.0 T as in Table 4.14 and 4.15 respectively.

Table 4.14 The image noise, SNR and CNR with various NSA for 2D images at 0.4 T compared to MRI 3.0 T

NSA	syringe		Bkg		SNR	CNR
	mean	SD	mean	SD (Noise)	SI (syr) / SD (bkg)	SI (syr)-SI (bkg) / SD (bkg)
1	18846.6	1558.9	988.5	452.6	41.64	39.45
2	19698.2	12483.3	370.9	363.4	54.2	53.18
3	23893.9	1728.3	598.2	382.6	62.45	60.88
4	23822.6	1904.1	538.7	310.2	76.76	75.06
3.0 T (NSA=1)	483.42	52.49	6.30	2.85	169.62	167.41

*****Scan time (s), NSA 1 (4), 2(8), 3(12), 4(16)

Table 4.15 The image noise, SNR and CNR of 3D images at 0.4 T compared to MRI 3.0 T

NSA	syringe		Bkg		SNR	CNR
	mean	SD	mean	SD (Noise)	SI (syr) / SD (bkg)	SI (syr)SI(bkg) / SD (bkg)
1	11531.6	136.3	666.2	118.7	97.12	91.51
2	11396.2	277.6	453.1	66.8	170.65	163.86
3	11008.6	284.3	355.0	48.0	229.20	221.81
4	15379.9	744.9	449.1	59.6	258.05	250.51
5	11496.2	462.9	289.5	31.2	368.70	359.42
3.0 T (NSA=1)	1187.91	119.39	4.13	2.19	542.42	540.53

*****Scan time (min), NSA 1 (1.2), 2(2.4), 3(4.0), 4(5.2), 5(6.4)

Table 4.14 shows the SNR and CNR for 2D MRCP imaging. SNR and CNR are highest (76.76 and 75.06) at NSA 4. For 3D images in table 4.15 the NSA at 5 shows a highest value for both SNR and CNR (368.7 and 359.42). The lowest noise is at NSA 4 (310.2) for 2D images and NSA 5 (31.2) for 3D images.

4.3 Determination of optimal parameters for MRCP imaging protocols in phantom at MRI 0.4 T

The optimal parameters for MRCP imaging protocols at MRI 0.4 T are determined by using the results of characteristics of MRCP imaging in duct phantom including evaluation of the spatial resolution, image noise, signal to noise ratio and contrast to noise ratio**.** The obtained optimal parameters are:

A. Slice thickness

As comparing side by side between the FWHM (Table 4.3) and the obtained signal intensity values, the image noise, SNR and CNR from various slice thickness are shown in Table 4.6 and 4.7.

2D image The thick-slab 40 mm was selected at the FWHM of 2.8 while in 3.0 T was 2.1. The SNR and CNR were accepted (40 mm was 146.03 and 143.17). Although, the obtained SNR was not a highest but the spatial resolution was still considered. The image noise decreased when the slice thickness increased (40 mm, 108.4 and 50mm, 90.7). In addition, the area coverage was considered at a larger part examination.

3D image The slice thickness at 2 mm is selected, although the values of SNR and CNR are lower than thicker slice thickness (SNR, 258.05 and CNR, 250.51). At 3D image, thin slices are selected to reconstruct MIP images, especially at pancreatic duct which is small size in diameter, the thin slices shows better resolution.

B. Field of view (FOV)

Similar to the slice thickness, the comparing side by side between the FWHM in Table 4.4 and the noise, SNR and CNR from various FOV are shown in Table 4.8 and 4.9.

2D image The FOV at 300 mm is selected as FWHM is 2.5 mm at 0.4Twhile at 3.0 T FWHM was 2.1 mm. The SNR and CNR show appropriate values at300 mm FOV of 102.53 and 100.48.

The noise is slightly decreased with increasing FOV. Although large FOV brought to increasing of SNR and CNR but the spatial resolution is poorer.

3D image The FOV at 300 mm is selected, although the SNR and CNR were lower than bigger size of FOV (SNR was 204.47 and CNR was 199.76). In this part, SNR and CNR decreased when FOV increased to 340 mm (SNR was163.7 and CNR was 159.38).

C. Number of phase encoding (matrix)

The FOV is kept constant while number of phase encoding is increased. As a results pixel size is smaller and SNR decreases, the spatial resolution was improved. The FWHM, (Table 4.5) SNR, CNR and noise are displayed at various number of phase encoding (Table 4.10 and 4.11):

2D image, the number of phase encoding 288 is selected because FWHM is not different at 2.4 mm while in 3.0 T FWHM is 2.1 mm. The SNR and CNR show the highest values (288 number of phase was 107.20 and 105.02). The noise is decreased when the number of phase increased.

3D images, the number of phase at 288 for 0.4 T, the FWHM was 2.9 mm while 3.0 T was 2.3 mm. The SNR and CNR were highest (SNR was 324.29 and CNR was 312.56) and the noise was lowest of 27.83.

D. Repetition time (TR)

When the TR increased the SNR increased according to the T1 recovery curve. Unfortunately, the increasing of scan time was followed. From Table 4.12 and 4.13 the optimal TR values were selected.

2D image, the TR at 5000 ms was selected because of the SNR and CNR showed the optimal values corresponding to the scan time (TR 5000 ms, SNR was 105.15, CNR was 102.27 and scan time for breath- hold was 10 s). The noise decreased when TR increased (TR 5000 ms noise 143.1, TR 6000 ms noise 135.4).

3D image, the TR at 6000 ms was selected, because the SNR and CNR were higher than the lower TR values (SNR was 372.9 and CNR was 365.19). In this part increasing of TR values results in decreasing noise. In addition, 3D MRCP in

volunteers, the respiratory triggering was used. The constant TR value depends on an appropriate pulse.

E. Number of signal average (NSA)

The NSA was similar to TR. The NSA is the number of times scan repeated that cause of smoothing and improvement in the image quality. Table 4.14 and 4.15 the optimal NSA corresponding scan time was selected.

2D image, the NSA value at 2 was selected because of the SNR and CNR showed the optimal values corresponding the scan time (SNR was 54.2, CNR was 53.18 and scan time for breath- hold 8 s). The noise decreased when NSA increased (NSA 2, which noise 363.4).

3D image, the NSA 4 was selected, because the SNR and CNR were higher than the lower NSA values (SNR was 258.05 and CNR was250.51). The noise decreased when NSA increased.

The optimal parameters for MRI 0.4 T is shown in Table 4.16 and 4.17 to achieve the good image quality of MRCP imaging, the acquisition parameters will be improved for healthy volunteers.

Table 4.16 The acquisition parameters of 2D MRCP imaging for MRI 0.4 T (Open)

Parameters	*Setting value*
Slice thickness	40 mm (Thick slab)
FOV	300 mm
Phase	288
TR	5000 ms
NSA	2
Scan time	10 s

*TE, Flip Angle and bandwidth cannot be changed.

Table 4.17 The acquisition parameters of 3D MRCP imaging for MRI 0.4 T (Open)

Parameters	*Setting value*
Slice thickness	2 mm
FOV	300 mm
Phase	288
TR	6000 ms
NSA	4
Scan time	8.00 min

*TE, Flip Angle and bandwidth cannot be changed.

4.4 Using MRCP protocols in volunteers.

From November to December 2010, ten adult healthy volunteers participated in the study. After the ethical had been approved by both the Ethics Committee, Faculty of Medicine, Chulalongkorn University and Rajavithi hospital, all volunteers gave their written informed consent for the study protocol. The group consisted of 8 men and 2 women with an age range of 25-57 years (mean age 34.7 years). The standard MRCP imaging protocols were determined for MRI 3.0 Tesla and the protocol with the optimal image quality in phantom of MRCP imaging for MRI 0.4 Tesla were performed in ten healthy volunteers. Figures 4.4- 4.13 for ten volunteers were shown (a and b were 2D and 3D images at 0.4 T and c and d at 3.0 T respectively).

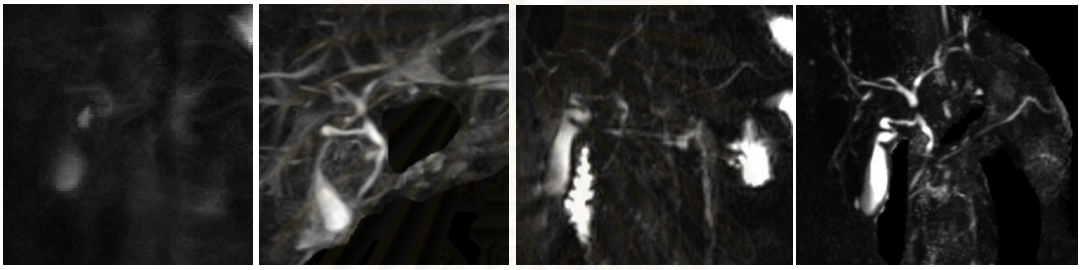

(a) (b) (c) (d)

Figure 4.4 Case No. 1 The MRCP imaging 2D, 3D at MRI 0.4 T (a),(b) and 2D, 3D at 3.0 T (c),(d) respectively

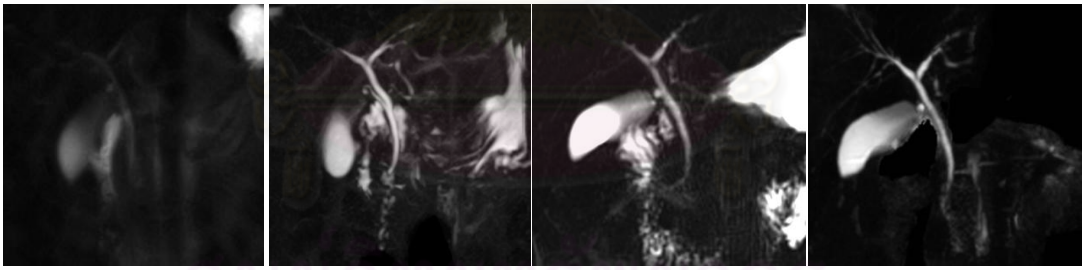

(a) (b) (c) (d)

Figure 4.5 Case No. 2 The MRCP imaging 2D,3D at MRI 0.4 T (a),(b) and 2D, 3D at 3.0 T (c),(d) respectively

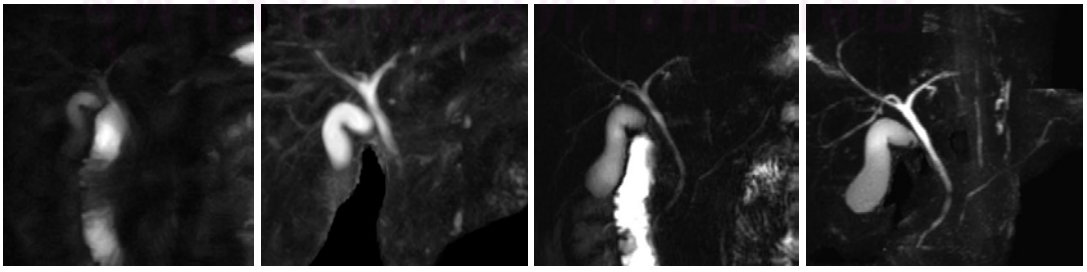

(a) (b) (c) (d)

Figure 4.6 Case No. 3 The MRCP imaging 2D, 3D at MRI 0.4 T (a),(b) and 2D, 3D at 3.0 T (c),(d) respectively

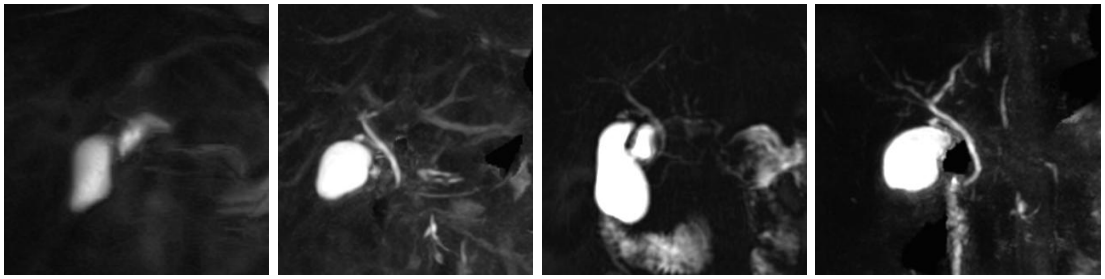

(a) (b) (c) (d)

Figure 4.7 Case No. 4 The MRCP imaging 2D, 3D at MRI 0.4 T (a),(b) and 2D, 3D at 3.0 T (c),(d) respectively

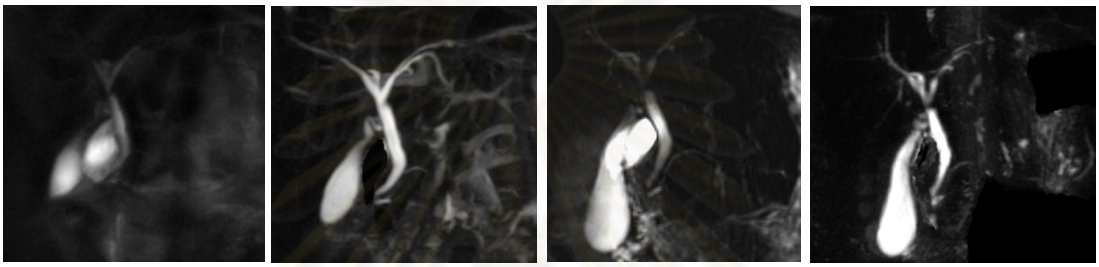

(a) (b) (c) (d)

Figure 4.8 Case No. 5 The MRCP imaging 2D, 3D at MRI 0.4 T (a),(b) and 2D, 3D at 3.0 T (c),(d) respectively

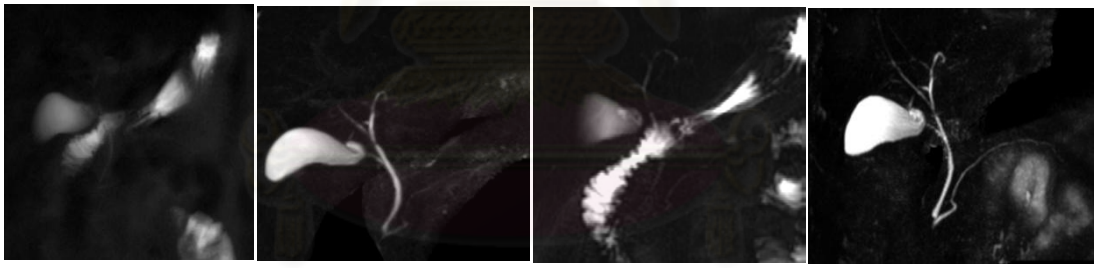

(a) (b) (c) (d)

Figure 4.9 Case No. 6 The MRCP imaging 2D, 3D at MRI 0.4 T (a),(b) and 2D, 3D at 3.0 T (c),(d) respectively

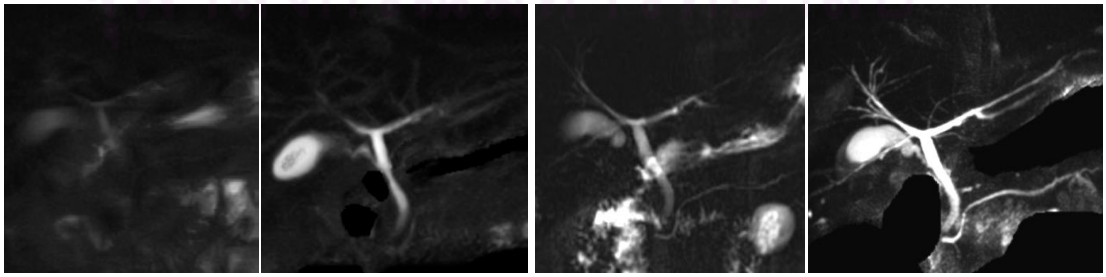

(a) (b) (c) (d)

Figure 4.10 Case No. 7 The MRCP imaging 2D, 3D at MRI 0.4 T (a),(b) and 2D, 3D at 3.0 T (c),(d) respectively

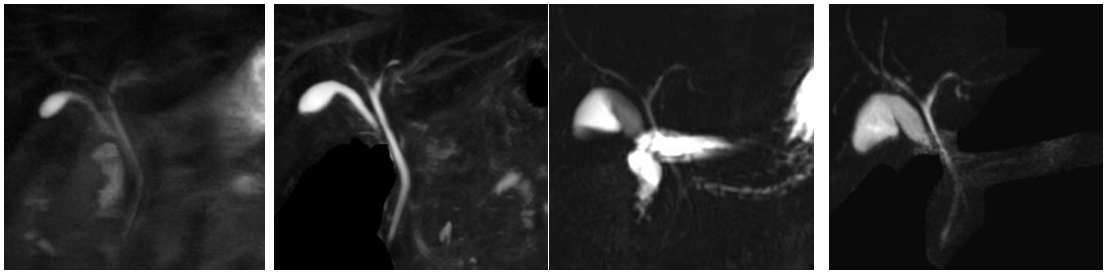

(a) (b) (c) (d)

Figure 4.11 Case No. 8 The MRCP imaging 2D, 3D at MRI 0.4 T (a),(b) and 2D, 3D at 3.0 T (c),(d) respectively

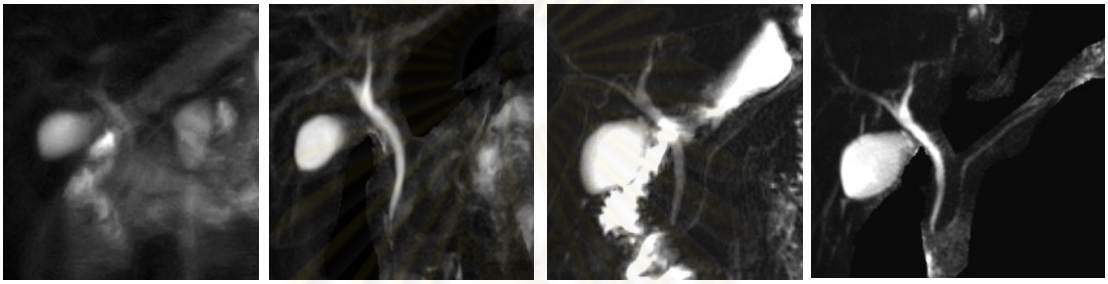

(a) (b) (c) (d)

Figure 4.12 Case No. 9 The MRCP imaging 2D, 3D at MRI 0.4 T (a),(b) and 2D, 3D at 3.0 T (c),(d) respectively

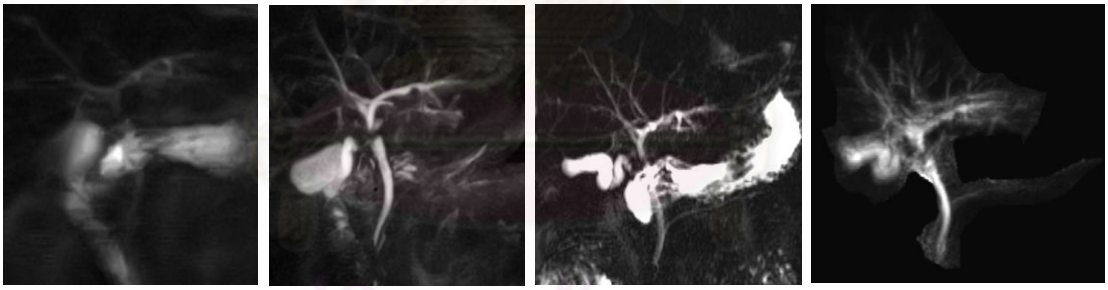

(a) (b) (c) (d)

Figure 4.13 Case No. 10 The MRCP imaging 2D, 3D at MRI 0.4 T (a),(b) and 2D, 3D at 3.0 T (c),(d) respectively

A. Quantitative assessment

The signal intensity at the common bile duct which passes through the head of pancreas and standard deviation (SD) of liver as the noise was assessed for the quantitative analysis of MRCP imaging. The mean signal and SD were calculated in terms of SNR, CNR as shown in Table 4.18 for 2D and Table 4.19 for 3D images at MRI 0.4 T and Table 4.20 and 4.21 for 2D and 3D images at MRI 3.0 T.

Table 4.18 The data for quantitative assessment of 2D MRCP imaging in 10 healthy volunteers at MRI 0.4 T

Case No.	0.4 Tesla					
	Pixel value (ROI)				SNR	CNR
	SI (CBD)		SI (Liver)		SI (CBD) / SD(Liver)	SI (CBD)-SI (Liver) / SD (Liver)
	Mean	SD	Mean	SD		
1	**3990.7**	**464.7**	**996.1**	**188.1**	**21.21**	**15.92**
2	**6641.6**	**1246**	**1514.8**	**245.3**	**27.08**	**20.90**
3	**4857.8**	**1088.2**	**828.2**	**144.6**	**33.59**	**27.87**
4	**8466.8**	**1328.3**	**800.9**	**153.9**	**54.98**	**49.87**
5	**4174.8**	**610.3**	**909**	**192.7**	**21.66**	**16.95**
6	**3079**	**424.3**	**1179.9**	**201.4**	**15.28**	**9.43**
7	**2552.9**	**236.2**	**260.7**	**100.7**	**25.35**	**22.76**
8	**5448.1**	**881.5**	**1270.3**	**413.3**	**13.18**	**10.11**
9	**4907.8**	**674.1**	**818.7**	**148.5**	**33.05**	**27.53**
10	**3465.7**	**731.8**	**867.7**	**201.8**	**17.17**	**12.87**

Table 4.19 The data for quantitative assessment of 3D MRCP imaging in 10 healthy volunteers at MRI 0.4 T

Case NO.	0.4 Tesla					
	Pixel value (ROI)				SNR	CNR
	SI (CBD)		SI (Liver)		SI (CBD) / SD(Liver)	SI (CBD)-SI (Liver) / SD (Liver)
	Mean	SD	Mean	SD		
1	**16613.9**	**1335.5**	**1052.8**	**105.7**	**157.17**	**147.21**
2	**10674.9**	**391.7**	**929.7**	**79.1**	**135.01**	**123.25**
3	**15527.1**	**1668.5**	**799.2**	**107.9**	**143.96**	**136.55**
4	**26283.9**	**973.4**	**1520.2**	**129.7**	**202.6**	**190.90**
5	**12315.8**	**1664.2**	**1325.8**	**106.2**	**115.92**	**103.45**
6	**10503.2**	**1083.3**	**732.3**	**68.3**	**153.86**	**143.13**
7	**8695.2**	**408.9**	**600.9**	**32.4**	**268.21**	**249.67**
8	**20075.4**	**1848.2**	**1172.9**	**79.8**	**251.63**	**236.93**
9	**13525.7**	**450.1**	**858.0**	**65.5**	**206.56**	**193.46**
10	**10873.7**	**205.2**	**649.1**	**84.9**	**128.11**	**120.46**

Table 4.20 The data for quantitative assessment of 2D MRCP imaging in 10 healthy volunteers at MRI 3.0 T

Case No.	3.0 Tesla					
	Pixel value (ROI)				SNR	CNR
	SI (CBD)		SI (Liver)		SI (CBD) / SD(Liver)	SI (CBD)-SI (Liver) / SD (Liver)
	Mean	SD	Mean	SD		
1	**295.3**	**29.5**	**4.5**	**2.6**	**114.45**	**112.68**
2	**314.1**	**31.1**	**5.71**	**2.9**	**105.76**	**103.84**
3	**241.1**	**79.4**	**4.6**	**1.5**	**157.10**	**154.12**
4	**339.0**	**57.4**	**4.7**	**2.5**	**136.70**	**134.73**
5	**339.4**	**13.5**	**5.8**	**2.5**	**134.16**	**131.89**
6	**458.2**	**40.7**	**10.9**	**4.54**	**100.05**	**98.54**
7	**355.5**	**59.1**	**2.2**	**1.8**	**199.71**	**198.45**
8	**139.8**	**58.2**	**5.3**	**1.9**	**74.36**	**71.53**
9	**190.5**	**31.7**	**4.6**	**2.6**	**73.26**	**71.50**
10	**246.4**	**78.4**	**2.67**	**2.80**	**86.93**	**87.06**

Table 4.21 The data for quantitative assessment of 3D MRCP imaging in 10 healthy volunteers at MRI 3.0 T

Case NO.	3.0 Tesla					
	Pixel value (ROI)				SNR	CNR
	SI (CBD)		SI (Liver)		SI (CBD) / SD(Liver)	SI (CBD)-SI (Liver) / SD (Liver)
	Mean	SD	Mean	SD		
1	**630.9**	**66.3**	**17.2**	**2.3**	**279.16**	**272.02**
2	**510.2**	**65.9**	**16.0**	**2.1**	**251.97**	**244.06**
3	**583.1**	**57.7**	**20.6**	**2.4**	**243.04**	**234.46**
4	**578.5**	**24.4**	**16.8**	**2.1**	**270.82**	**262.95**
5	**429.09**	**51.9**	**16.2**	**1.79**	**240.25**	**231.16**
6	**550.3**	**73.5**	**16.0**	**1.87**	**294.11**	**285.56**
7	**512.5**	**43.8**	**24.6**	**2.3**	**219.95**	**209.39**
8	**409.8**	**34.8**	**23**	**3.85**	**106.43**	**100.46**
9	**451.6**	**57.7**	**14.1**	**1.5**	**309.33**	**299.64**
10	**763.1**	**68.4**	**27.1**	**3.2**	**235.5**	**218.81**

From Table 4.18 – 4.21 the quantitative assessment by measurement of SNR and CNR values were illustrated the summarized values by comparison the signal intensity between performed at MRI 0.4 T and 3.0 T as shown in Table 4.22 and Figure 4.14

Table 4.22 The SNR and CNR of previous and optimal protocols of 2D and 3D MRCP imaging 0.4 T compared to 3.0 T in duct phantom study

Proto-cols	SNR			CNR		
	0.4 T	3.0 T	p-value	0.4 T	3.0 T	p-value
previous 2D	89.18± 12.5	169.62± 4.2	0.0026	87.05± 8.1	167.41± 4.1	0.0009
Optimal 2D	102.08± 5.92		0.0013	100.04± 6.71		0.0016
previous 3D	239.12± 33.9	542.42± 22.9	0.0033	232.36± 31.1	540.53± 23.1	0.0029
Optimal 3D	345.65± 34.37		0.0022	336.26± 26.70		0.0028

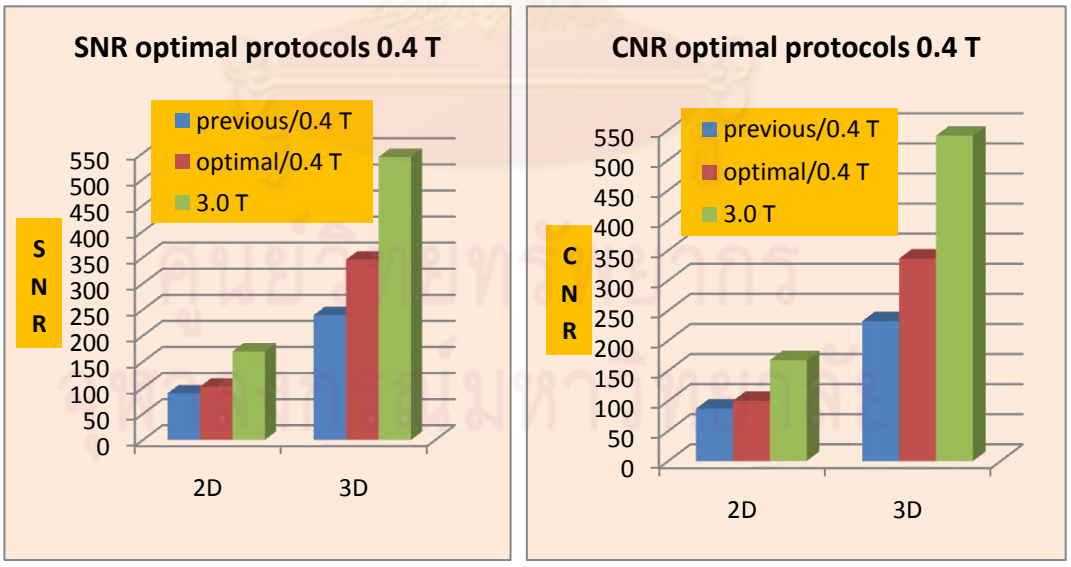

Figure 4.14 The comparison of SNR, CNR for previous and optimal protocols 0.4 T and 3.0 T of 2D and 3D MRCP imaging in phantom study

Table 4.23 The SNR and CNR of 2D and 3D MRCP imaging in 10 healthy volunteers

Protocols	SNR			CNR		
	0.4 T	3.0 T	p-value	0.4 T	3.0 T	p-value
2D	**26.25 ± 11.61**	**118.25 ± 37.65**	**0.00001**	**22.33 ± 11.93**	**116.46 ± 39.66**	**0.000009**
3D	**176.31 ± 53.04**	**245.06 ± 53.27**	**0.021**	**164.50 ± 50.78**	**235.85 ± 55.7**	**0.016**

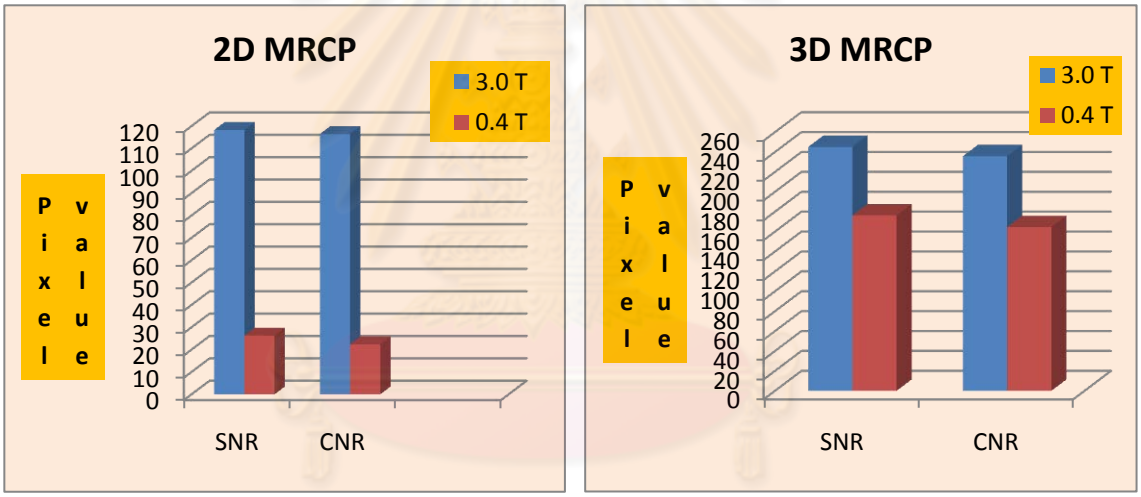

Figure 4.15 The comparison of SNR, CNR at 0.4 T and 3.0 T of 2D and 3D MRCP imaging in ten volunteers

B. Qualitative assessment

One radiologist had scored images from 0.4 T and 3.0 T. Seven structures analyzed consist of gall bladder, right hepatic duct, left hepatic duct, common hepatic duct, common bile duct, cystic duct and pancreatic duct. Five-point scale was used to assess the image appearance as shown in Table 4.24 for 2D images and Table 4.25 for 3D images respectively. The bar chart of figure 4.16 and 4.17 showed the image quality between at 0.4 T and 3.0 T of 2D and 3D MRCP imaging for visualization of each ducts.

Table 4.24 The 2D MRCP image quality scored by one radiologist with 2 readings

Structure of ducts	Scores (1)		P-value	Scores (2)		P-value
	2D 0.4 T	2D 3.0 T		2D 0.4 T	2D 3.0 T	
RHD	1±0.81	2.3±1.17	0.00087	1.4±1.07	3.2±0.78	0.00018
LHD	1.22±0.48	2.66±0.78	0.000043	1.7±0.94	3.2±0.78	0.00004
CHD	2.0±0.94	3.3±0.82	0.00009	1.9±0.99	3.4±0.84	0.00043
GB	2.7±1.15	3.7±0.94	0.00053	2.4±0.69	3.8±0.63	0.000006
CyD	0.69±0.4	1.5±1.18	0.015	0.4±0.69	1.7±1.33	0.011
CBD	1.1±0.74	2.8±1.03	0.000053	1.6±1.07	3.4±0.84	0.0025
PaD	0.55±0.70	1.9±1.19	0.0047	0.5±0.97	2.3±1.33	0.0012

RHD (Right hepatic duct), LHD (Left hepatic duct), CHD (Common hepatic duct), GB (Gall bladder), CyD (Cystic duct), CBD (Common bile duct), PaD (Pancreatic duct)

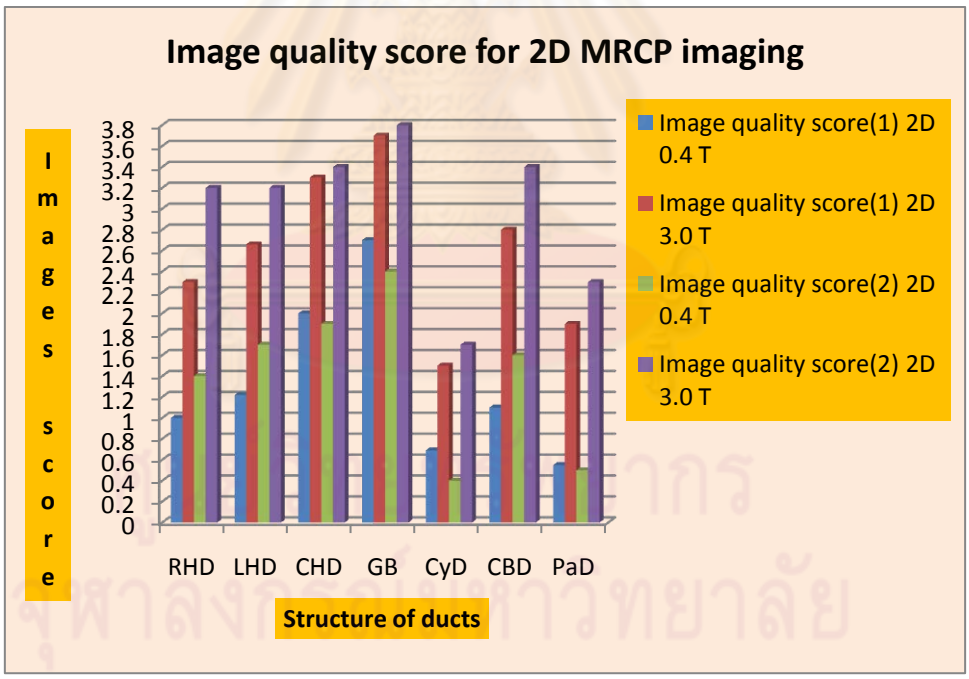

Figure 4.16 The comparison of scores on 2D MRCP imaging structure of ducts with 2 readings

The consistency image quality scored by one radiologist was assessed by calculating intra-class correlation coefficients (ICC) for the 7 ducts structure. ICCs were calculated using the image quality score of the 2 readings for one observer. The data of ICCs is shown in table 4.25 for 2D 0.4 T and 2D 3.0 T.

Table 4.25 The ICCs of image quality scored by one radiologist with 2 readings

ICCs		
Structure of ducts	**2D 0.4 T**	**2D 3.0 T**
RHD	0.61	0.77
LHD	0.61	0.78
CHD	0.71	0.76
GB	0.75	0.92
CyD	0.68	0.80
CBD	0.83	0.85
PaD	0.69	0.71

The intra-observer of image quality score showed moderate up to high agreement. ICCs for intra-observer agreement from table 4.25 were 0.61 at RHD and LHD for 2D 0.4 T and 0.92 at GB for 2D 3.0 T whereas in table 4.27 the lowest value as showed at GB for 3D 0.4 T (0.64) and the highest at GB for 3D 3.0 T also (1.0).

Table 4.26 The 3D MRCP image quality scored by one radiologist with 2 readings

Structure of ducts	**Image quality scores (1)**		**P-value**	**Image quality scores (2)**		**P-value**
	3D 0.4 T	**3D 3.0 T**		**3D 0.4 T**	**3D 3.0 T**	
RHD	**2.33±0.82**	**2.7±0.67**	**0.13**	**3.0±0.81**	**3.4±0.69**	**0.13**
LHD	**2.33±0.84**	**2.8±0.63**	**0.15**	**3.1±0.87**	**3.4±0.69**	**0.21**
CHD	**3.40±0.69**	**3.2±0.91**	**0.17**	**3.6±0.51**	**3.2±0.63**	**0.18**
GB	**3.90±0.31**	**3.80±0.63**	**0.33**	**3.7±0.48**	**3.8±0.63**	**0.36**
CyD	**2.20±1.47**	**2.6±1.17**	**0.17**	**2.2±1.54**	**2.8±1.13**	**0.08**
CBD	**3.30±0.94**	**3.3±0.67**	**0.5**	**3.6±0.96**	**3.7±0.48**	**0.39**
PaD	**1.2±0.91**	**2.1±1.19**	**0.05**	**1.0±1.05**	**2.5±1.26**	**0.01**

RHD (Right hepatic duct), LHD (Left hepatic duct), CHD (Common hepatic duct), GB (Gall bladder), CyD (Cystic duct), CBD (Common bile duct), PaD (Pancreatic duct)

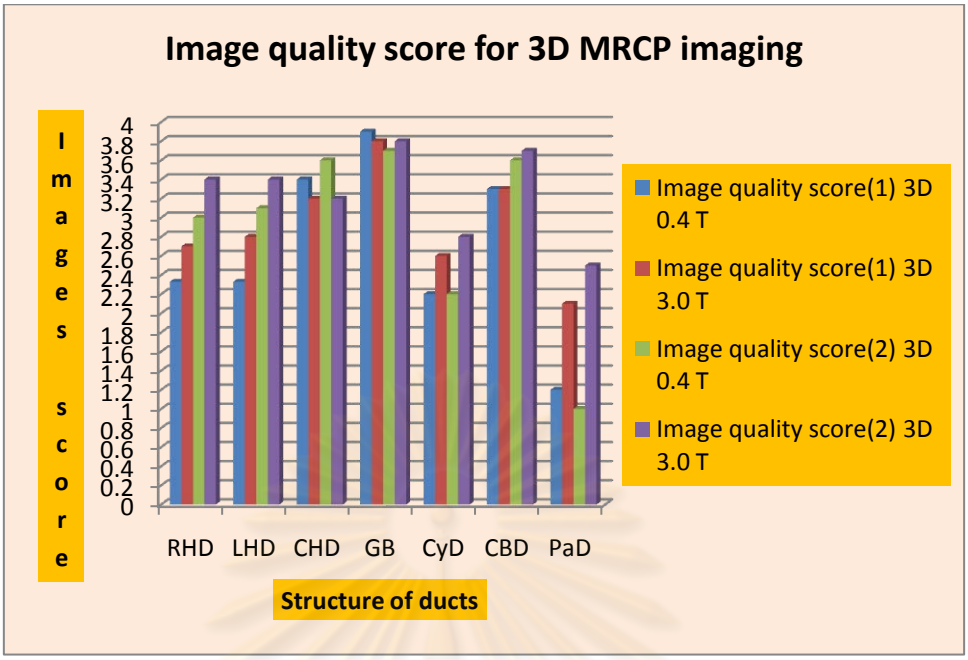

Figure 4.17 The score on image quality for 3D MRCP imaging structure of ducts of 2 readings by one radiologist

Table 4.27 The ICCs of image quality score of 2 readings by one radiologist

ICCs		
Structure of ducts	**3D 0.4 T**	**3D 3.0 T**
RHD	0.66	0.75
LHD	0.69	0.70
CHD	0.76	0.75
GB	0.64	1.00
CyD	0.75	0.68
CBD	0.87	0.68
PaD	0.79	0.78

The overall image quality was the average score of structure of ducts for each case. It was shown as in Table 4.28 and 4.29 for both 2D and 3D images. The bar chart (Figure 4.18) shows the overall image quality at both field strengths of 2D and 3D MRCP imaging.

Table 4.28 The overall image quality of MRCP imaging for 2D for both field strengths

Case No.	Overall image scores (1)		P-value	Overall image scores (2)		P-value
	2D 0.4 T	2D 3.0 T		2D 0.4 T	2D 3.0 T	
1	0.42±0.53	1.57±0.53	0.002	0.14±0.37	2.42±0.78	0.0003
2	1.71±0.95	3.0±1.15	0.0002	2.14±1.46	3.83±1.49	0.007
3	1.28±1.11	2.42±1.27	0.002	1.14±1.06	3.28±1.11	0.0009
4	1.14±1.34	2.14±1.34	0.03	1.14±0.89	2.85±1.21	0.0015
5	2.57±0.97	3.14±0.89	0.05	2.71±0.48	2.85±0.69	0.048
6	1±1	2±1	0.001	1±0.92	2.28±1.38	0.017
7	1.14±0.69	3.71±0.48	0.00007	1.42±0.97	3.85±0.37	0.00009
8	1.29±1.25	2.0±1.52	0.047	1.66±1.13	2.57±1.39	0.007
9	1±1.15	3.0±1.4	0.0018	1±0.87	3.14±1.46	0.0017
10	1.43±0.81	3.43±0.53	0.0003	2±1.15	3.42±0.78	0.001
Average	1.3±0.55	2.64±0.71	0.000047	1.43±0.72	3.04±0.52	0.00002

The different of image score between 0.4 T and 3.0 T for 2D MRCP imaging showed the p-values lesser than 0.05 in table 4.28 whereas in table 4.29 for 3D MRCP imaging showed the average overall image quality which p-values greater than 0.05 are significantly different.

Table 4.29 The overall image quality of MRCP imaging for 3D for both field strengths

Case No.	Overall image scores (1)		P-value	Overall image scores (2)		P-value
	3D 0.4 T	3D 3.0 T		3D 0.4 T	3D 3.0 T	
1	2.71±1.11	3.28±0.48	0.05	3±1.41	3.57±0.53	0.13
2	2.57±1.39	3.42±0.53	0.023	3.14±1.46	3.57±0.78	0.09
3	1.71±1.49	2.85±1.07	0.002	1.87±1.46	3.42±0.78	0.016
4	2.42±1.13	2.57±1.27	0.38	3±1	3±1.41	0.5
5	3.71±0.75	2.43±0.78	0.086	3.85±0.37	3.14±0.69	0.41
6	3.0±0.81	3.42±0.53	0.09	3.14±1.06	3.71±0.48	0.11
7	3.0±0.57	3.0±0.57	0.5	3.14±0.89	4±0	0.022
8	2.57±1.51	2.42±1.13	0.38	2.14±1.67	2.71±0.95	0.08
9	2.28±1.79	3.43±0.53	0.03	2.42±1.39	3.42±0.53	0.01
10	2.71±0.75	1.42±0.78	0.22	3.28±0.95	1.85±0.69	0.81
Average	2.67±0.52	2.93±0.64	0.15	2.89±0.58	3.39±0.61	0.12

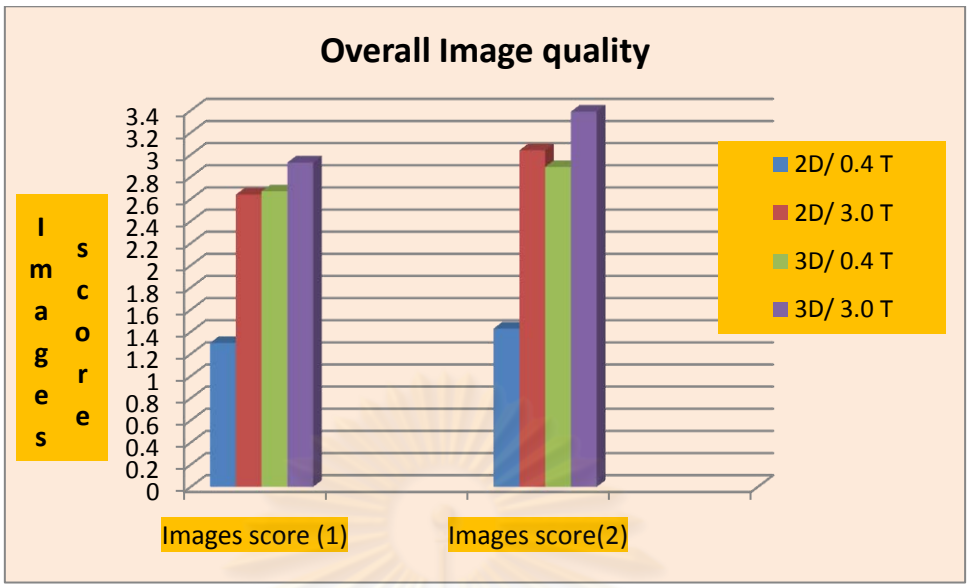

Figure 4.18 The overall image quality of 2D and 3D images at 3.0 T and 0.4 T of 2 readings by radiologist

Figure 4.18 shows the different of image score for 2D MRCP imaging between 0.4 and 3.0 T whereas for 3D MRCP imaging the image of no difference.

CHAPTER V

DISCUSSION AND CONCLUSION

5.1 Discussion

MRI is a digital, three-dimensional imaging modality of great flexibility with respect to image contrast and its spatial characteristics. However, one of the downsides of this flexibility is a greater complexity in terms of the choice of scanning parameters. In general, the scan time is not negligible and there is a certain tendency towards artifact. However, it was agreed that the fundamental limitation in MRI is the signal-to-noise ratio (SNR) which depends on the hardware, particularly the main field strength and radiofrequency (RF) coils, the relaxation properties of tissue and the choice of sequence parameters. Good image quality is dependent on selecting the proper parameters. Therefore, the aim of this study is to investigate the influence of acquisition parameters on the image quality and the practical trade-offs between SNR, CNR and spatial resolution. The characteristics of MRCP images were studied to obtain the optimal parameters with the suitable scan time.

5.1.1 Characteristics of MRCP imaging in phantom study

A. Evaluation of the spatial resolution in MRCP images using a duct phantom.

The characteristics of the MRCP images were studied by the investigation of spatial resolution, image noise, SNR and CNR. The spatial resolution is evaluated by imaging of the plastic tube duct phantom diameter 2.0 mm.

From this study the MRCP images of duct phantom from coronal 2D showed a shorter FWHM than 3D of both field strengths as in Table 5.1

Table 5.1 The FWHM of 2D and 3D MRCP imaging in duct phantom for 0.4 T

FWHM (mm)		
Field strength (T)	2D image	3D image
0.4	2.5	2.9

As the result on Table 5.1, the signal intensity on 2D image is less than on 3D image (Figure 5.1).

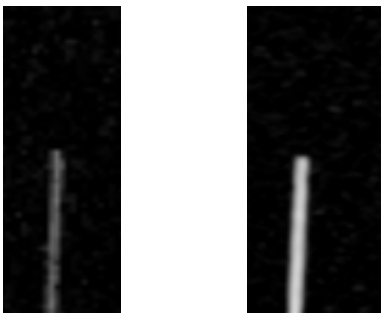

(a) (b)

Figure 5.1 The signal intensity in duct phantom 2D (a) and 3D (b) images, 0.4 T.

Figure 5.1 shows different signal intensity between 2D and 3D images. The normalized profile curves were created across the duct to measure the FWHM at point A as in figure 5.2 and Table 5.1

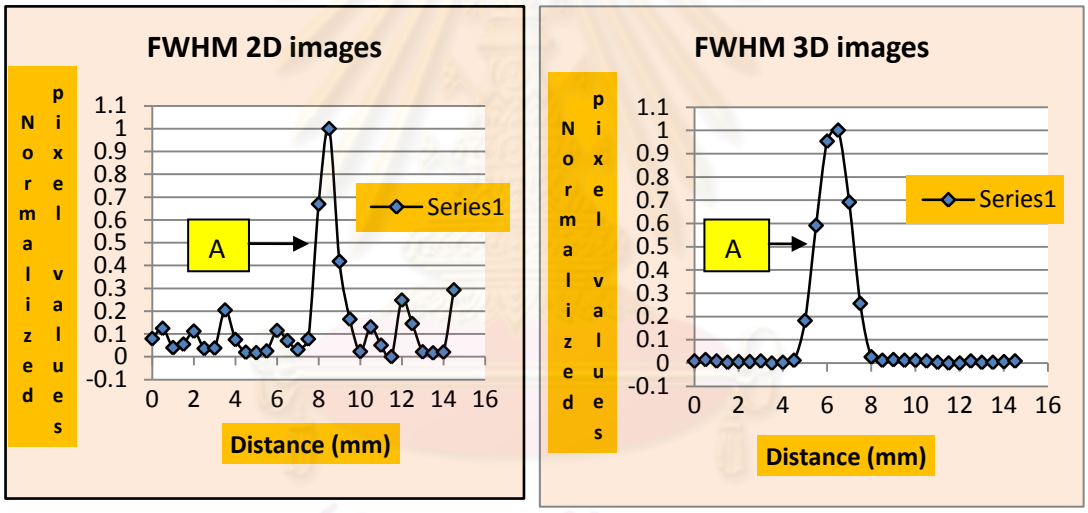

Figure 5.2 The normalized FWHM of 2D and 3D images for 0.4 T

Figure 5.2 shows the corresponding FWHM determined at a half of normalized values (0.5) at point A.

As the duct in phantom contained only saline, T2 weighted pulse sequence showed hyper signal intensity (brightness in T2) on the 2D and 3D images. The 2D MRCP protocol resulted in the signal which could express only the effect T2 weighted while 3D MRCP provides for both T2 weighted and including intrinsically contiguous sections to reconstruct images in MIP (Maximum intensity projection). Volumetric acquisition itself boosts the signal-to-noise ratio. As each excitation covers the entire volume, every phase-encoding step essentially adds average signal, which results in an increase signal- to-noise ratio by the square root of the number of sections. Thus, the 3D image has shown higher signal than at 2D image.

B. Signal to noise ratio (SNR), contrast to noise ratio (CNR) and image noise for MRCP imaging.

Variation of the slice thickness

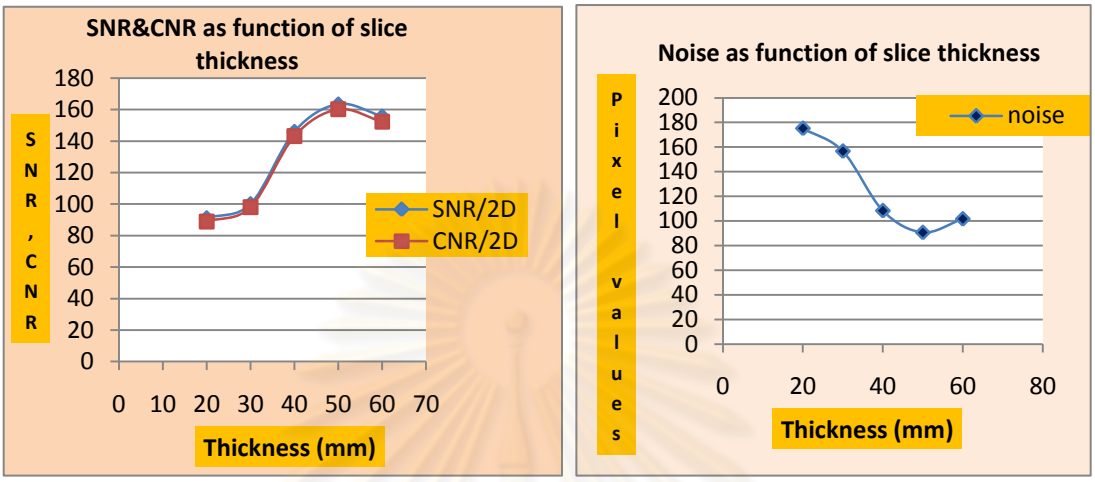

(A) (B)

Figure 5.3 The SNR & CNR (A) and noise (B) as function of slice thickness on 2D coronal plane MRCP imaging at MRI 0.4 T

As the slice thickness increased, the signal intensity increased, the noise decreased and the SNR improved, but the impact of partial volume effect also increased. At the small slice thickness, the spatial resolution is improved. Figure 5.3(A) shows the increasing slice thickness from 20-60 mm with increasing SNR and CNR from 90 to 160 and noise (B) decreased from 175 to 100.

Variation of field of view (FOV)

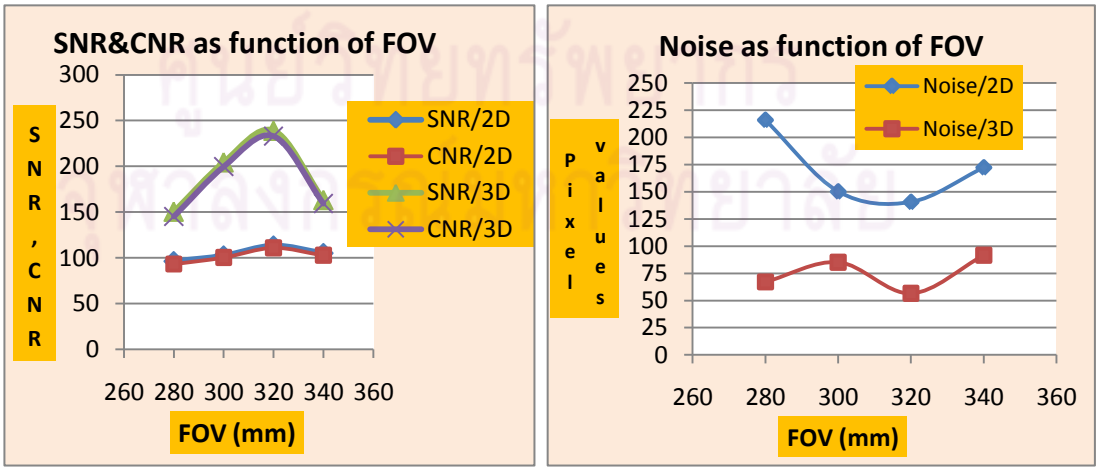

(A) (B)

Figure 5.4 The SNR & CNR (A) and noise (B) as function of FOV on 2D and 3D coronal plane MRCP imaging at MRI 0.4 T

Increasing the FOV without changing the matrix size resulted in the in-plane pixels bigger, more signal strength. Spatial resolution is poorer and the image appeared smaller, surrounded by larger area of background [16]. Figure 5.4 (A) shows the increasing SNR and CNR with increasing FOV up to 340 mm. As the FOV is 360 mm the noise increased resulted in decreasing SNR and CNR.

Variation of number of phase encoding (matrix)

The statistical variation in the pixel value of signal and background at different phases resulting in the fluctuation of SNR, CNR and noise at phase 288 and 320 for MRI 0.4 T. Equation (2) and (3) in chapter II shows SNR depend on the square root of NSA, number of phase encoding over bandwidth and other parameters by NSA or phase encode doubles, signal double and noise increases (randomly) by √2 [17].

FOV is kept constant with increasing number of phase encoding, the noise, SNR and CNR show statistical fluctuation. Table 5.2 shows SNR and CNR decreased at phase 192 to 256 and increased at phase 288 and 320, due to the automatic reconstruction of the software 0.4 T. When number of phase encoding is higher than 256, matrix 512 will be used.

Table 5.2 The noise, SNR and CNR at various phase numbers for 2D image at 0.4 T

Phase	**syringe**		**Bkg**		**SNR**	**CNR**
	mean	**SD**	**mean**	**SD** (Noise)	**SI** (syr) / **SD** (bkg)	**SI** (syr)-**SI** (bkg) / **SD** (bkg)
192	**16023.1**	**1094.7**	**380.1**	**177.5**	**90.27**	**88.13**
256	**14539.1**	**1064.5**	**403.1**	**169.1**	**85.99**	**83.61**
288	**14719.1**	**440.1**	**298.8**	**137.3**	**107.20**	**105.02**
320	**14704.1**	**759.8**	**390.4**	**150.9**	**97.44**	**94.85**

When matrix size is increasing to 512, phase number increasing, SNR signal increased.

5.1.2 Evaluation of the SNR, CNR for MRI 0.4 T and 3.0 T (Quantitative assessment)

Table 5.3 SNR, CNR using optimal 2D protocol for 0.4 T compared to 3.0 T in phantom

Parameters	**2D**					
	SNR			**CNR**		
	0.4 T	**3.0 T**	**3.0/0.4T**	**0.4 T**	**3.0 T**	**3.0/0.4T**
Slice thickness (40 mm)	146.03	169.62	1.16	143.17	167.41	1.16
FOV	102.53	169.62	1.65	100.48	167.41	1.66
phase	107.20	169.62	1.58	105.02	167.41	1.59
TR	105.15	169.62	1.61	102.7	167.41	1.63
NSA	89.95	169.62	1.88	87.68	167.41	1.91

Table 5.4 SNR and CNR using optimal 3D protocol for 0.4T compared to 3.0T in phantom

Parameters	**3D**					
	SNR			**CNR**		
	0.4 T	**3.0 T**	**3.0/0.4T**	**0.4 T**	**3.0 T**	**3.0/0.4T**
Slice thickness (2mm)	258.05	542.42	2.10	250.51	540.53	2.15
FOV	204.47	542.42	2.65	199.76	540.53	2.70
phase	324.29	542.42	1.67	312.56	540.53	1.72
TR	372.9	542.42	1.45	365.19	540.53	1.48
NSA	258.05	542.42	2.10	250.51	540.53	2.15

Table 5.3 and 5.4 show the ratio of SNR and CNR between 3.0 T and 0.4 T in phantom study. All parameters at 3.0 T shows ratio of SNR and CNR greater than 1 at 0.4 T.

Table 5.5 Comparison of 2D MRCP imaging for SNR, CNR at 0.4T with 3.0 T in volunteers

Case No.	2D					
	SNR			CNR		
	0.4 T	3.0 T	3.0/0.4T	0.4 T	3.0 T	3.0/0.4T
1	21.21	114.45	5.39	15.92	112.68	7.07
2	27.08	105.76	3.90	20.90	103.84	4.96
3	33.59	157.10	4.67	27.87	154.12	5.52
4	54.98	136.70	2.48	49.87	134.73	2.70
5	21.66	134.16	6.19	16.95	131.89	7.78
6	15.28	100.05	6.54	9.43	98.54	10.4
7	25.35	199.71	7.87	22.76	198.45	8.71
8	13.18	74.36	5.64	10.11	71.53	7.07
9	33.05	73.26	2.21	27.53	71.50	2.59
10	17.17	86.93	5.06	12.87	87.06	8.76

Table 5.6 Comparison of 3D MRCP imaging for SNR, CNR at 0.4T with 3.0 T in volunteers

Case No.	3D					
	SNR			CNR		
	0.4 T	3.0 T	3.0/0.4 T	0.4 T	3.0 T	3.0/0.4 T
1	157.17	279.16	1.77	147.21	272.02	1.84
2	135.01	251.97	1.86	123.25	244.06	1.98
3	143.96	243.04	1.68	136.55	234.46	1.71
4	202.6	270.82	1.33	190.90	262.95	1.37
5	115.92	240.25	2.07	103.45	231.16	2.23
6	153.86	294.11	1.91	143.13	285.56	1.99
7	268.21	219.95	0.82	249.67	209.39	0.83
8	251.63	106.43	0.42	236.93	100.46	0.42
9	206.56	309.33	1.49	193.46	299.64	1.54
10	128.11	235.5	1.83	120.46	218.81	1.81

Table 5.5 and 5.6show the ratio between SNR and CNR of MRI 3.0 T and 0.4 T in volunteers. The data shows higher ratio of SNR and CNR in 2D of 3.0 T than at 0.4 T where 3D protocol at case No. 7 and No. 8, the ratio of SNR and CNR are less than 1 in 3.0/0.4 T. The 2D MRCP imaging in case No.7 at 3.0 T shows higher ratio than at 0.4 T of 8 times for SNR and 10 times in case No. 6 for CNR.

Table 5.7 The average SNR and CNR of 2D and 3D MRCP imaging in 10 healthy volunteers

protocols	**SNR**		**CNR**	
	0.4 T	3.0 T	0.4 T	3.0 T
2D	26.25	118.25	22.33	116.46
3D	176.31	245.06	164.50	235.85

Table 5.7 shows the higher SNR and CNR of 3D imaging than 2D imaging. From equation (2) and (3) in chapter II.

2D SNR α Sequence×voxel$_{x,y,z}$ ×$\frac{\sqrt{NSA \times Number\ \ of\ phase\ (y)}}{\sqrt{Bandwidt\ h}}$ ×coil type× magnetic field× reconstruction algorithms ; where y is phase encoding in the y direction .

3D SNR α Sequence×voxel$_{x,y,z}$ ×$\frac{\sqrt{NSA \times Number\ \ of\ phase\ (y,z)}}{\sqrt{Bandwidt\ h}}$ ×coil type× magnetic field× reconstruction algorithms ; where y and z are phase encoding in y and z direction.

In 3D imaging, the factors contributing to SNR are the same as in 2D imaging including phase encoding in the z direction which resulting the higher SNR in 3D imaging than 2D imaging.

5.1.3 Image quality assessment by radiologist for 10 normal volunteers of MRCP imaging (Qualitative assessment)

Table 5.8 The overall image quality average scores of MRCP 3D for both field strengths

	Overall image score (1)		**P-value**	**Overall image score (2)**		**P-value**
Average score	3D 0.4 T	3D 3.0 T		3D 0.4 T	3D 3.0 T	
	2.67±0.52	2.93±0.64	0.15	2.89±0.58	3.39±0.61	0.12

Table 5.8 shows the average score for 10 volunteers by radiologist with 2 readings, the p-value >0.05. There is no significantly different in scoring image quality between 0.4 and 3.0T. Factors concerned the image quality are the different acquisition time for volunteers, the distance between two sites and different signal intensity in biliary system as shown in figure 5.5 and 5.6.

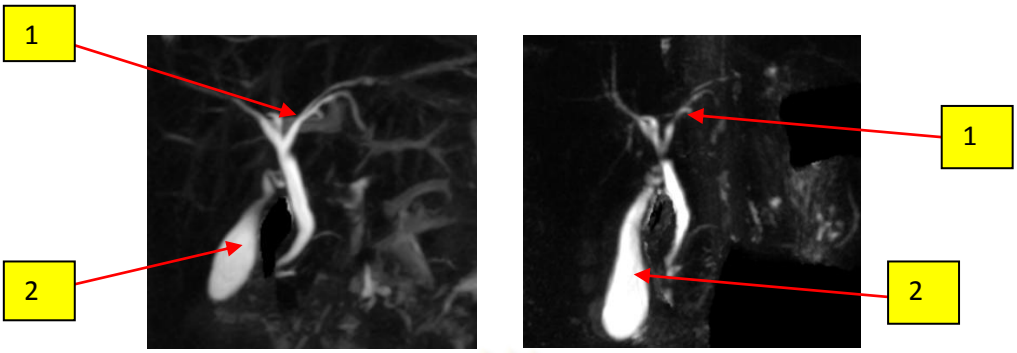

(a) (b)

Figure 5.5 The 3D MRCP imaging of case No.5, (a) at 0.4 T and (b) at 3.0 T

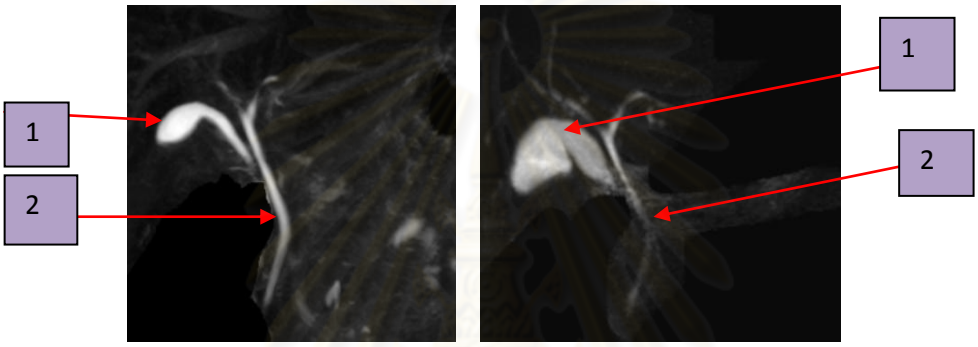

(a) (b)

Figure 5.6 The 3D MRCP imaging of case No.8, (a) at 0.4 T and (b) at 3.0 T

From figure 5.5 the point number 1 shows the different signal in left hepatic duct and number 2 shows the different size of gall bladder whereas figure 5.6 shows the different size of gall bladder (number 1) and different signal in common bile duct (number 2)

The intra-class correlation coefficients (ICC) for the 7 ducts structure

Table 5.9 The ICCs of 2D image quality score of 2 readings by one radiologist

ICCs		
Structure of ducts	**2D 0.4 T**	**2D 3.0 T**
RHD	0.61	0.77
LHD	0.61	0.78
GB	0.75	0.92

As in table 5.9 the intra-observer of image quality score shows moderate agreement values (0.61) at RHD and LHD for 2D 0.4 T. The highest ICCs at GB for 2D 3.0 T also (0.92).

Table 5.10 The ICCs of 3D image quality score of 2 readings by one radiologist

ICCs		
Structure of ducts	**3D 0.4 T**	**3D 3.0 T**
RHD	0.66	0.75
LHD	0.69	0.70
GB	0.64	1.00
CBD	0.87	0.68

Table 5.10 shows the intra-observer of image quality score of moderate agreement value (0.64) at GB for 3D 0.4 T. The same as on 3D image, the highest ICCs at GB for 3D 3.0 T also (1.0).

The intra-class correlation coefficient is the intra- observer agreement which values between 0 to1. The highest value is 1.0 expresses the consistency agreement of observer. This study showed the moderate ICCs values on some small ducts whereas the large part, for example at gall bladder showed a high ICCs value of an observer in this study.

5.1.4 Determination of optimal parameters for MRCP imaging protocols.

Three factors determined whether a particular detail or structure can be visualized in MRCP images. Clearly there needs to be **contrast** between the structure of ducts and its surroundings. Second, if the **resolution** is insufficient, information about the object will not be transferred into the image by the image formation process. Third, if SNR and CNR are too low, the details of the structure may be obscured by image **noise**.

In chapter IV, optimal protocols of MRCP imaging, are affected by the choice of slice thickness, FOV, matrix size, TR and NSA. If the slice is thicker, the SNR is better but the resolution is reduced. If the slice is thin, the SNR is too low to visualize the detail. As well as FOV, TR and NSA, if these factors increase the SNR and CNR increase follow whereas the scan time will increase also. For example of determination of the optimal protocols in this study as in Table 5.11 shows the optimal slice thickness.

Table 5.11 The resolution (FWHM), SNR and CNR for optimal slice thickness MRCP imaging MRI 0.4 T

Thickness (mm)		**FWHM** (mm)		**SNR**		**CNR**	
2D	3D	2D	3D	2D	3D	2D	3D
20	2	2.6	2.8	91.18	258.05	88.84	250.51
30	3	2.6	2.8	100.14	261.30	98.02	254.97
40	4	2.8	2.9	146.03	352.70	143.17	344.68

From table 5.11, 40 mm slice thickness was selected for 2D because of in MRCP imaging of 2D thick slab, the coverage anatomical region of every branch of ducts are considered in spite of the resolution decrease from 2.6 at 20 mm to 2.8 mm whereas for 3D image was selected at 2 mm with the reason of the thin slice was better resolution at small branches for MIP images reconstruction. According to thin slice expresses the better resolution but the reasonable SNR and CNR should be considered for large branches also. The different of diameter of ducts in biliary system for example small branch pancreatic duct and large branch common bile duct, the selecting optimal protocols in this study were selected at the optimal SNR, CNR, resolution including the appropriate scan time.

The same argument is true for in plane changes although the pixel dimensions are generally smaller. An important stage in image optimization therefore is to decide on the trade-off required between the voxel size required for an adequate SNR and the requirement for the voxel size to be small enough to permit the visualization of small anatomical or pathological details.

5.2 Conclusions

5.2.1 The optimal parameters setting for protocols of MRCP imaging at 0.4 T

From the primary research question: What are the optimal MRI protocols for MRCP imaging acquired by MRI 0.4 Tesla (Open) in comparison to MRI 3.0 Tesla? Therefore the optimal acquisition parameters of MRCP imaging were shown in Table 5.12.

Table 5.12 The acquisition parameters of 2D and 3D MRCP imaging for MRI 0.4 T (Open) compared to 3.0 T

Parameters	**2D**		**3D**	
	0.4 T	3.0 T	0.4 T	3.0 T
Plane	coronal	coronal	coronal	coronal
Pulse sequences	FSE breath-hold	SSh MRCP Rad TSE	Heavily T2W FSE	HR-SENSE T2W TSE
TR	5,000 ms	5,640 ms	6,000 ms	2,340 ms
*TE (fixed)	512 ms	740 ms	540 ms	740 ms
*FA (fixed)	90	90	90	90
Slice thickness	40 mm	40 mm	2 mm	2 mm
FOV	300 mm	300 mm	300 mm	300 mm
Gap (interval)	0	0	0	0
Number of Phase	288	256	288	256
Number of Frequency	256	256	256	255
NSA	2	1	4	1
Scan time	10 s	5 s	8.00 min	3.39 min
*Bandwidth (fixed)	30.5 kHz	375.6 Hz/pixel	47.8 kHz	223.4 Hz/pixel
Option	-	-	Respiratory gating	Respiratory gating

*TE, Bandwidth and Flip Angle cannot be changed.

5.2.2 Quantitative and qualitative assessments in MRCP imaging at 0.4 T and 3.0 T

A. Quantitative assessment

From the secondary research question: What are the image quality (spatial resolution and SNR) for MRI 0.4 Tesla (Open) and 3.0 Tesla in phantom study?

The image quality as described for quantitative assessment of spatial resolution, SNR and CNR are summarized using statistical variation to compare 0.4 T and 3.0T as shown in Table 5.13, 5.14 and 5.15.

Table 5.13 The spatial resolution (FWHM) of 2D and 3D MRCP imaging in duct phantom 2.0 mm diameter

FWHM (mm)		
Field strengths (T)	2D image	3D image
0.4	2.5	2.9
3.0	2.1	2.3

Table 5.13 shows MRI 3.0 T has better spatial resolution for both 2D and 3D imaging than MRI 0.4 T.

Table 5.14 Mean SNR and CNR of 2D and 3D imaging in phantom study

Proto-cols	**SNR**			**CNR**		
	0.4 T	**3.0 T**	**p-value**	**0.4 T**	**3.0 T**	**p-value**
previous 2D	**89.18± 12.5**	**169.62± 4.2**	**0.0026**	**87.05± 8.1**	**167.41± 4.1**	**0.0009**
Optimal 2D	**102.08± 5.92**		**0.0013**	**100.04± 6.71**		**0.0016**
previous 3D	**239.12± 33.9**	**542.42± 22.9**	**0.0033**	**232.36± 31.1**	**540.53± 23.1**	**0.0029**
Optimal 3D	**345.65± 34.37**		**0.0022**	**336.26± 26.70**		**0.0028**

Table 5.15 Mean SNR and CNR of 2D and 3D MRCP imaging in 10 healthy volunteers

Pro-tocols	**SNR**			**CNR**		
	0.4 T	**3.0 T**	**p-value**	**0.4 T**	**3.0 T**	**p-value**
2D	**26.25 ± 11.61**	**118.25 ± 37.65**	**0.00001**	**22.33 ± 11.93**	**116.46 ± 39.66**	**0.000009**
3D	**176.31 ± 53.04**	**245.06 ± 53.27**	**0.021**	**164.50 ± 50.78**	**235.85 ± 55.7**	**0.016**

Table 5.14 and 5.15 show MRI 3.0 T has significantly potential to provide better SNR and CNR for both 2D and 3D imaging than MRI 0.4 T (Open) (p-value <0.05).

B. Qualitative assessment

The qualitative assessment with 2 readings by one radiologist is summarized for all scores of ducts visibility including the overall image quality by overall image quality as shown in Table 5.16.

Table 5.16 The overall image quality score with 2 readings in volunteers by one radiologist

Pro-tocols	**Image quality scores (1)**		**p-value**	**Image quality scores (2)**		**p-value**
	0.4 T	3.0 T		0.4 T	3.0 T	
2D	1.3±0.55	2.64±0.71	0.000047	1.43±0.72	3.04±0.52	0.00002
3D	2.67±0.52	2.93±0.64	0.15	2.89±0.58	3.39±0.61	0.12

2D SSh MRCP Rad TSE at 3.0 T provided improvement diagnostic images of the all ducts while at 0.4 T 2D breath-hold FSE cannot be displayed the same information sufficiently (p-value<0.05) whereas at 0.4 T 3D heavily T2W FSE MRCP imaging with optimal protocols show reasonable image quality as well as 3D High resolution SENSE T2W TSE imaging which all ducts were not significant different in image quality by radiologist for 2 readings (p-value > 0.05) except at pancreatic duct (p-value < 0.05). For overall image quality, 2D MRCP imaging at 3.0 T was significant improvement than 0.4 T (p-value < 0.05) except 3D imaging (p-value >0.05) showing no significantly different between 0.4 and 3.0 T. Therefore, the MRCP imaging at 0.4 T could be beneficial in adding up the confidence at 3D images.

With these conclusions:

- MRI 3.0 T has better spatial resolution, SNR and CNR in phantom and SNR and CNR in volunteers than MRI 0.4 T.
- MRI 3.0 T shows the qualitative analysis significantly different for 2D breath-hold sequence than MRI 0.4 T.
- MRI 3.0 T provided different significant diagnostic 3D MRCP image and better visualization of pancreatic duct than optimal 3D MRCP protocol MRI 0.4 T.

Although the result is not statistical significantly analysis in 3D image of overall image quality but several processing studies show that MRI 3.0 T is superior to MRI 0.4 T. As the research hypothesis is that the image quality obtained from MRI 3.0 Tesla is better than MRI 0.4Tesla (Open) on both phantom and MRCP imaging is proved.

REFERENCES

[1] Toshio, K., et al. Open MRI for clinicians. Today's Open MRI :Tokyo; (2004): 18-19.

[2] Larkman, D.J., et al. A comparison of MR cholangiopancreatography at and 3.0 Tesla. British Journal of Radiology; 78(2005): 894–898.

[3] Hiroyoshi, I., et al. MRCP Imaging at 3.0 T vs 1.5 T: Preliminary Experience in Healthy Volunteers. Magnetic resonance Imaging; 25(2007): 1000-1006.

[4] Yasui, M., et al. MR cholangiopancreatography: Comparison of image Obtained with 1.0 and 1.5 Tesla units. Radiology; 20(2002): 77-82.

[5] Pavone, P., et al. MR cholangiopancreatography (MRCP) at 0.5 T: Technique optimization and prelinary results. European Padiology; 6 (1996): 147-152.

[6] Tamura, R., et al. Chronic Pancreatitis: MRCP versus ERCP for Quantitative Caliber Measurement and Qualitative Evaluation. Radiology; 23 (2006): 920-928.

[7] Michael, A., Tamer, S., Ronald, O., AAPM/RSNA Physics Tutorial for Residents. Radiographics; 7(2007):1213-1229.

[8] Richard, B., et al. MR Pulse Sequences: What Every Radiologist Wants to Know but Is Afraid to Ask. Radiographics; 26(2006): 513-537.

[9] Perry sprawls. Magnetic Resonance Imaging. Spatial Characteristics of the Magnetic Resonance Image : United States of America: (2000): 89-122.

[10] Irie, H., et al. Optimal MR Cholangiopancreatographic Sequence and Its Clinical Application. Radiology; 206(1998): 379-387.

[11] Hataipat, J., and Anchali, K., Optimization of Abdomen Multiplanar Reformation (MPR) with Isotropic Data Sets Aquired for 16-Detector CT Scanner. M.Sc.Thesis in medical imaging. Department of Radiology Faculty of Medicine Chulalongkorn University, 2008.

[12] American Association of Physicists in Medicine. Quality Assurance Methods and Phantoms for Magnetic Resonance Imaging (AAPM Report No. 28). Newyork, United State of America; 1990.

[13] American Association of Physicists in Medicine**.** Acceptance Testing of Magnetic Resonance Imaging Systems (AAPM Report No. 34). Newyork, United State of America; 1990.

[14] MRI Acceptance Testing. Magphan Manual. The phantom Laboratory Newyork; (2001): 1-23.

[15] Laila, A., et al. Clinical Magnetic Resonance Imaging. MR Cholangiopancreatography. Philadephia; Volume 3 (2006): 2480-2487.

[16] Donald, W., Elizabeth, A., Martin, J., Martin, R., MRI from picture to Proton. Ghosts in the machine: quality control.Cambridge university. United Kingdom; (2004): 201-216.

[17] Catherine, W., Carolyn, K., MRI in Practice. Parameters and Trade-offs. Oxford MRI Center; (1993): 95-96.

[18] SPSS 19.0 Command Syntax (2010). SPSS Inc., Chicago III: from http://en.wikipedia.org/wiki/SPSS [15 April 2011].

[19] Koch, Gary G., Intra-class correlation coefficient. Encyclopedia of statistical Sciences. New York; (1982): 213–217.

[20] Ray H., William G., MRI the Basis. Scan parameters and image optimization. California; (1997): 167-174.

APPENDICES

Appendix A: Data Sheet quantitative Image quality

The data sheet for quantitative assessment of MRCP imaging
Protocol……..

Magnetic field / Case No.	0.4 Tesla(Hitachi : Aperto)					
	Pixel value (ROI)				SNR	CNR
	SI (CBD)		SI (Liver)		SI (CBD) / SD (Liver)	SI (CBD)-SI (Liver) / SD (Liver)
	Mean	SD	Mean	SD		
1						
2						
3						
4						
5						
6						
7						
8						
9						
10						

Comments.....
.....

The data sheet for quantitative assessment of MRCP imaging

Protocol……..

Magnetic field / Case No.	3.0 Tesla (Philips: Achieva TX)					
	Pixel value (ROI)				SNR	CNR
	SI (CBD)		SI (Liver)		$\frac{\text{SI (CBD)}}{\text{SD (Liver)}}$	$\frac{\text{SI (CBD)-SI(Liver)}}{\text{SD (Liver)}}$
	Mean	SD	Mean	SD		
1						
2						
3						
4						
5						
6						
7						
8						
9						
10						

Comments.....

.....

The data sheet for qualitative assessment of MRCP imaging for … D at …. T

Protocols……..

Case No…….

Structures of ducts	Preference score					Remark
	4	3	2	1	0	
1.Right hepatic duct						
2.Left hepatic duct						
3.Common hepatic duct						
4.Gall bladder						
5.Cystic duct						
6.Common bile duct						
7.Pancreatic duct						

Scales

4= very good (diagnostic image quality, visualize structures with homogenous of ducts)
3= good (still diagnostic, visualize structures with inhomogeneous of ducts)
2= moderate (partly diagnostic)
1= poor (barely diagnostic)
0= non diagnostic (lacking enhancement of the ducts)

Comments

……
……
……
……

Appendix B:The performance test of MRI Scanners

Report of MRI system performance study

Location: MRI center, Sirinthorn building floor 1, Rajavithi Hospital
Date: 28 July 2010
Manufacturer: MRI 0.4 Tesla (Open), Hitachi: Aperto

Location: MRI center, Apuntree-Pacha building Floor 1, King Chulalongkorn Memorial Hospital
Date: 7 August 2010
Manufacturer: MRI 3.0 Tesla, Philips: Achieva TX

Quality control of MRI scanners were performed according to AAPM protocol report No. 28, 34, and Magphan manual as follows:

- ☐ Image uniformity
- ☐ Sensitometry (MRI number)
- ☐ High contrast resolution
- ☐ Low contrast sensitivity
- ☐ Slice geometry (slice width)
- ☐ Geometric distortion (spatial linearity)
- ☐ Slice position/Separation

Materials

1. Magphan phantom

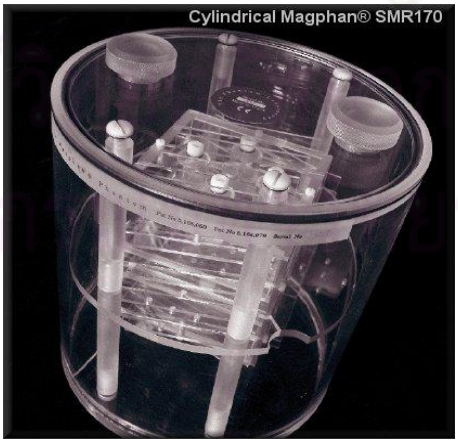

Figure I. Magphan phantom

Image uniformity

Purpose To test the ability of the MR imaging system to produce a constant signal response throughout the scanned volume when the object is being imaged with homogeneous MR characteristics.

Method A Magphan homogeneous phantom is used. Two liquid bath options are available, test cube plane 2 and the Magphan housing without the test cube and support disk (Figure II). Employ a pulse sequence with the following parameters: TR = 1000 ms, TE = 30 ms, single echo, slice thickness = 10 mm or less.

Place an ROI at the center of the image of the signal producing volume, enclosing at least 75% of the image, excluding regions near the edge. Determine the maximum (S_{max}) and minimum (S_{min}) pixel values within the ROI. Calculate the percent integral uniformity (PIU) as following equation:

$$PIU = [1 - (S_{max} - S_{min}) / (S_{max} + S_{min})] \times 100\ \%$$

S_{max} is maximum pixel values within the ROI, S_{min} is minimum pixel values within the ROI. The integral uniformity should be typically 80 % or better.

Results

Magnetic field strengths	PIU (%)	Acceptance decision
0.4 Tesla	93.33	Pass
3.0 Tesla	96.30	Pass

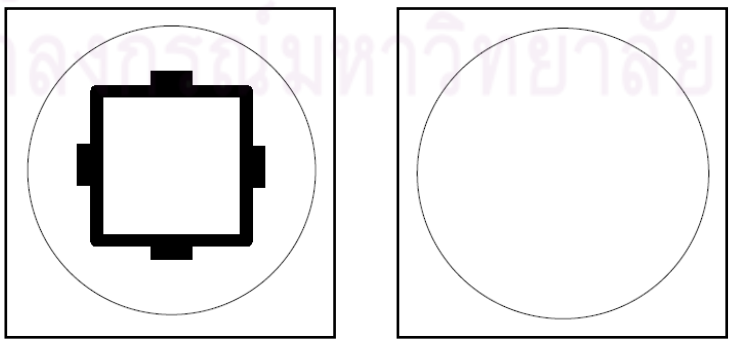

(A) (B)

Figure II. (A) Test cube plane 2 and (B) Magphan phantom housing.

Sensitometry (MRI number)

Purpose To measure the mean pixel value (ROI) in four sensitometric vials.

Method Since, the same parameters from image uniformity test. Four sensitometric targets vials are found in the top scan plane of the Magphan test cube. Four solutions with known systematical varied concentrations can be used. The results are only recording each vial daily a log of MRI number reproducibility can be established.

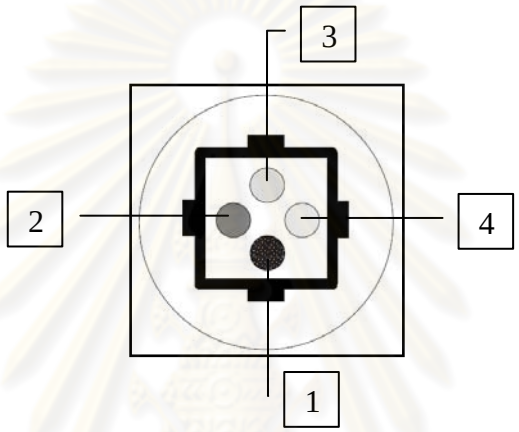

Figure III. Four sensitometric target vials in the top scan plane of the Magphan test cube.

Results

Magnetic field strengths	Vials	Mean Day 1	Mean Day 2	Mean Day 3	Mean Day 4	Mean Day 5
0.4 Tesla	1	17261.2	17342.8	17218.4	17200.2	16890.7
	2	17525	17492.3	17518.2	17470.6	16990.4
	3	17555.8	17680.5	17947.8	17749.2	18714.9
	4	19732.4	19821.4	18990.5	19645.5	19120.6
3.0 Tesla	1	913.1	897.6	945.2	1012.4	927.6
	2	1645.2	1721.2	1657.8	1598.7	1628.9
	3	1851.4	1878.6	1853.9	1792.8	1901.6
	4	1917.1	1932.9	1934.8	2003.3	2126.5

High contrast resolution

Purpose To measure the capacity of an imaging system to show separation of objects when there is no significant noise contribution.

Method Index the scanner to the resolution section. This section has a 1 to 11 line pair/cm, high resolution test pattern. The targets are 1, 2, 3, 4, 5, 6, 7, 8, 9, 10, and 11 line pair/cm. The high-contrast resolution should be equal to the pixel size. For example for a 25.6 cm field-of-view with a 256x256 acquisitions matrix, the resolution should be 1 mm.

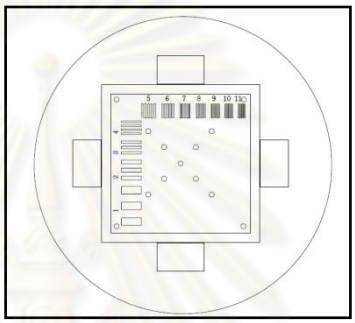

Figure IV. High resolution pattern

Results

Magnetic field strengths	**Smallest resolvable array element** (lp/cm)	**Accepted** (~ 1.1 mm)
0.4 Tesla	4.5 line pair/cm	pass
3.0 Tesla	5 line pair/cm	pass

Low contrast sensitivity

Purpose To measure the ability to distinguish differences in intensity in an image.

Method Determine the actual contrast levels of phantom, calculate the average of the measurements from several scans of low contrast section. Plotting the diameter of the hole VS. the depth of the hole visualized to estimate contrast detail curve.

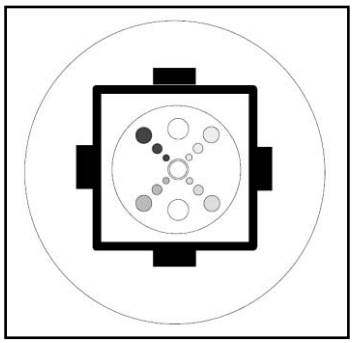

Figure V. Low contrast pattern

Results

Magnetic field strengths	**Depths** (mm)	**Mean value of pixel intensity**		
		Diameters (mm)		
		4.0	**6.0**	**10.0**
0.4 Tesla	0.5	11673.8	10862	10500
	0.75	12476	12452	12926
	1.0	13582	14603	15478
	2.0	14912.6	16440	16882.5
3.0 Tesla	0.5	1050.6	1040.9	1027.2
	0.75	1075.1	1079.4	1089.9
	1.0	1176.7	1203.0	1124.5
	2.0	1612.8	1560.3	1543.6

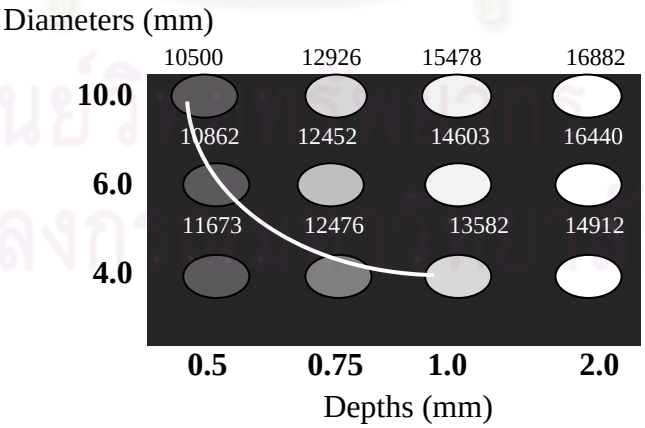

Figure VI. Contrast detail curve MRI 0.4 T

Slice geometry (slice width)

Purpose To estimate the full width at half maximum (FWHM) of the slice profile.

Method Slice thickness should generally agree with the indicated slice thickness within ± 1 mm for slice thicknesses > 5 mm.

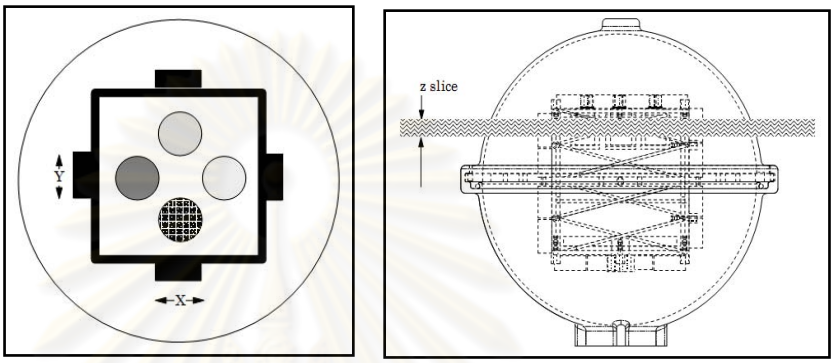

Figure VI. Slice geometry pattern

Results

Magnetic field strengths	**Slice thickness** (mm)	**Acceptance decision**
0.4 Tesla	(X), Z = 5.125 (Y), Z = 5.125	Pass Pass
3.0 Tesla	(X), Z = 5.025 (Y), Z = 5.025	Pass Pass

Geometric distortion

Purpose To measure the displacement of displayed points within an image relative to their known location, or improper scaling of the distance between points anywhere within the image.

Method Percent distortions in the spatial linearity (when measured over a 25 cm or greater FOV) are generally considered acceptable if they are < 5%.

Percent distortion is defined as following:

$$\frac{\text{True dimension} - \text{observed dimension}}{\text{True dimension}} \times 100\ \%$$

A

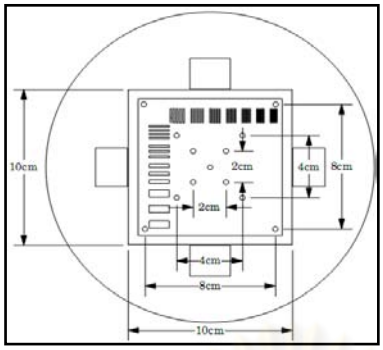

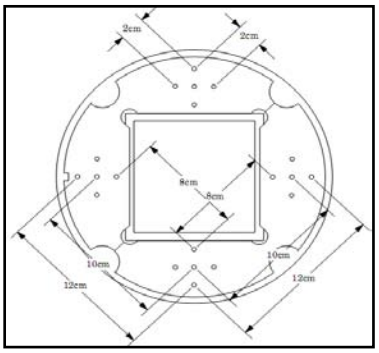

B

Figure VII. Geometric distortion (spatial linearity) pattern

Results

A

Distance	2 cm	4 cm	8 cm	10 cm
Measured distance (x) 0.4 T/3.0 T	2.0/1.99	4.04/4.01	7.92/8.06	10.0/10.07
Measured distance (y) 0.4 T/3.0 T	1.94/2.01	4.01/3.98	8.02/7.99	10.0/10.01

B

Distance	2 cm	8 cm	10 cm	12 cm
Measured distance (R) 0.4 T/3.0 T	2.0/2.02	7.98/7.99	9.99/9.99	11.9/12.0
Measured distance (L) 0.4 T/3.0 T	2.05/1.99	7.99/8.03	9.99/10.07	11.9/12.03

Magnetic field strengths	**Distortion** (%)	**Acceptance decision**
0.4 Tesla	<5	Pass
3.0 Tesla	<5	Pass

Slice position/Separation

Purpose To test for proper scanner selection among and between slices, and for table movement on MRI systems.

Method Slice position (offset) is the absolute location of the midpoint of the FWHM of the slice profile. Slice separation is the distance between any two slice positions. Slice locations are indicated by external positioning devices or by the selected inter-slice spacing.

Measure from the center of the first ramp to the center of the second ramp and multiply it by .25 (the 14° scaling factor) to determine the scan index between scans.

Comparison of external position marker should generally agree with the actual slice position within ± 2 mm. Slice separation disagreement should typically be < 20% of the total slice separation or ± 1 mm, whichever is greater.

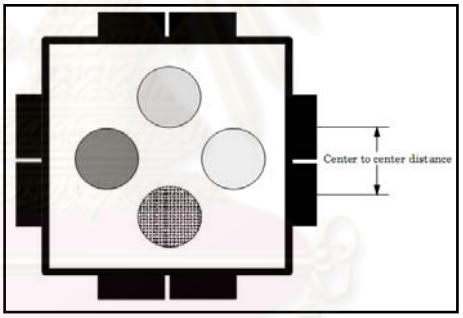

Figure VIII. Schematic illustration of 2 superimposed used to test the indexing accuracy between slices.

Results For 3.0 T the center of the first ramp to the center of the second ramp = 20.1

Therefore; $20.1 \times 0.25 = 5.025$ mm

For 0.4 T the center of the first ramp to the center of the second ramp = 21.5

Therefore; $21.5 \times 0.25 = 5.375$ mm

Magnetic field strengths	Actual slice position	Acceptance decision
0.4 Tesla	0.025	Pass
3.0 Tesla	0.375	Pass

Table I. Overview of parameters for QC testing

Parameters	**0.4 Tesla**		**3.0 Tesla**	
Brain protocol	T1	T2	T1	T2
FOV	250	250	250	250
TR (ms)	400	4500	400	4500
TE (ms)	15	100	15	100
FA	90	90	90	90
Number of slices	20	20	20	20
Thickness (mm)	5	5	5	5
Interval (mm)	0	0	0	0
Frequency	256	256	256	256
Phase	224	224	223	224
NSA	2	2	2	2
Bandwidth (kHz)	9	16	-	-
Scan time (min)	5.42	2.59	6.00	2.19

FOV-Field of view, TR-Repetition time, TE-Echo time, FA-Flip angle, kHz-kilo-Hertz

VITAE

NAME	Mr. Krisadang Thasenhod
NATIONALITY	Thai
DATE OF BIRTH	20 December, 1973
INSTITUTIONS ATTENDED	Bachelor degree of Science (Radiological Technology), Mahidol University, 1996
POSITION HELD&OFFICE	1996-present: Radiological Technologist,Department of Radiology , Rajavithi Hospital, Bangkok, Thailand
ADDRESS	24/321 Moo 2, T.Klongha, Klongluang district, Patumthani province, Thailand, 12120
E-MAIL ADDRESS	Krisadangthd@hotmail.com